NUMERICAL SIMULATIONS OF STRUCTURAL AND FLUID DYNAMICS FOR AERODYNAMIC PERFORMANCE IMPROVEMENT

by

Haoliang Yu

APPROVED BY SUPERVISORY COMMITTEE:

Arif Malik, Chair

Stefano Leonardi, Co-Chair

William Anderson

Giacomo Valerio Iungo

Dong Qian

Jie Zhang

NUMERICAL SIMULATIONS OF STRUCTURAL AND FLUID DYNAMICS FOR AERODYNAMIC PERFORMANCE IMPROVEMENT

by

HAOLIANG YU, BS, MS

DISSERTATION

Presented to the Faculty of

The University of Texas at Dallas

in Partial Fulfillment

of the Requirements

for the Degree of

DOCTOR OF PHILOSOPHY IN

MECHANICAL ENGINEERING

THE UNIVERSITY OF TEXAS AT DALLAS

May 2021

ACKNOWLEDGMENTS

I want to start with expressing my appreciation to my advisor, Dr. Arif Malik, for the faith he put in me who didn't indicate any talent and showed no strong background knowledge in this field by the time I joined his research group. I also want to thank both of my advisors, Dr. Arif Malik and Dr. Stefano Leonardi, for their mentorship, patience and support over these years. I would like to express my gratitude to my committee members, Dr. William Anderson, Dr. Giacomo Valerio Iungo, Dr. Dong Qian and Dr. Jie Zhang, for their valuable time, suggestions and comments in my research. I want to thank all my friends from ECSN, ECSW and WSTC for their time, support, and help during this wonderful journey.

I want to heartily thank my parents and girlfriend for their understanding and support all along. Without it, I wouldn't be able to go through all the difficult times and achieve my goals.

The work in this dissertation was supported in part by the the National Science Foundation and the teaching research assistantship provided by the department of mechanical engineering at The University of Texas at Dallas. The University of Texas at Dallas' Cyberinfrastructure & Research Services Department and The Texas Advanced Computing Center (TACC) are acknowledged for providing computational resources.

March 2021

NUMERICAL SIMULATIONS OF STRUCTURAL AND FLUID DYNAMICS FOR AERODYNAMIC PERFORMANCE IMPROVEMENT

Haoliang Yu, PhD
The University of Texas at Dallas, 2021

Supervising Professors: Arif Malik, Chair
Stefano Leonardi, Co-Chair

The present research aims to understand and improve the aerodynamic performance of airfoils in unmanned aerial vehicle (UAV) and wind energy applications using numerical approaches. Specifically, the research applications include: 1) the flexibility tailoring of passively induced airfoil shapes for thin UAV wings, and 2) the aerodynamic performance evaluation of wind turbine blade airfoils that include idealized leading edge (LE) damage patterns aimed at emulating erosion. In both applications, fundamental insights that motivate subsequent optimum design configurations are sought through the use of computational tools of varying efficiency and fidelity.

In regard to the first airfoil type studied, UAVs have attracted special attention in recent decades due to their unique and adaptable functionality for both military and civilian applications. Among fixed-wing UAVs, those with flexible passively-deforming wings have been shown to achieve extended aerodynamic endurance, reduced power consumption, and beneficial stability characteristics. Since neither excessively flexible nor excessively rigid wings maximize aerodynamic performance, flexibility tailoring for such membrane wings is still of significant interest. However, the numerical and experimental studies to date have been mostly limited to 2D studies, specifically to chordwise flexibility. To gain insights into fur-

ther design improvements, such as enabling extended aerodynamic endurance, more complex 3D geometric flexibilities, as are investigated and described in this work. Emulating a bio-inspired flexible UAV wing design, a novel topology optimization using a genetic algorithm with an efficient fluid structure interaction (FSI) model produces a wing frame configuration with optimal flexibility distribution. The decoupled effects of the induced camber and span-wise bending deformation are analyzed to understand their contributions to performance improvements.

Regarding the second airfoil type studied, designing wind turbine blades to achieve both extended service life and high operating efficiency is of great interest. Leading edge erosion, which poses significant problems to efficiency, necessitates research into the understanding of the underlying fluid dynamics. However, strong three-dimensionality of flow and relatively small scale of erosion poses great challenges to understanding and predicting the flow behavior numerically in terms of fidelity and computational time. Presented is a reduced order model (ROM) proposed for efficient drag prediction on a streamlined body with surface imperfections that emulate leading-edge roughness or erosion-induced damage. It requires as input only the geometric description of damage. Satisfactory performance is demonstrated via comparison with direct numerical simulations. Insights into the flow physics influencing both form and friction contributions to total drag are presented, a preferable damage mode from an engineering design aspect is revealed.

In summary, the described work addresses the research gaps through applying a set of numerical tools with varying fidelity and efficiency to conduct investigations from the aspects of aerodynamic performance, geometric design, and optimization. The results of the research provide new understanding in how to improve aerodynamic performance in both airfoil application types.

TABLE OF CONTENTS

LIST OF FIGURES

LIST OF TABLES

CHAPTER 1

INTRODUCTION

1.1 Bio-inspired unmanned aerial vehicle (UAV) wing

Unmanned aerial vehicles (UAVs) have been widely adapted for aerial photography, movie cinematography, disaster/military/agricultural surveillance, package delivery, etc. Accordingly, researchers and engineers have focused on improving UAV performance through extended-capacity lightweight batteries, simpler system controllability, and improved aerodynamic performance for carrying greater payloads, attaining longer flight duration, and increasing flight maneuverability in diverse flight conditions. Research to date has recognized that aerodynamic benefits can be gained by the adoption of flexible frame-membrane wings on UAVs. Passive deformation of flexible wings under aerodynamic load was found able to increase lift [101], decrease drag [2, 14], delay stall [42] and mitigate against strong gust encounters [48]. To maximize the aerodynamic performance, the flexibility tailoring of such flexible UAV wings draws great interest.

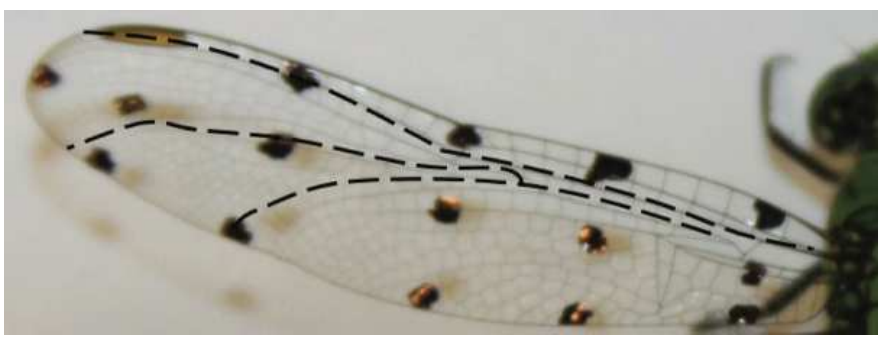

Figure 1.1. Sketch of the main wing veins (dashed lines) on the left forewing [33].

Initially inspired by insect wings, some flexibility studies of flapping wings were reported. In a review paper by Gursul et al. [49], tailoring of both spanwise and chordwise flexibility was identified by researchers as a potential means to improve thrust for flapping wings. Local deformation and stiffness distribution of fly wings were studied by Wehmann et al. [97]. They suggested that the local deformation greatly depends on the inertial and aerodynamic forces, which are closely related to the wing stiffness distribution and geometry shape. A picture of the forewing of the dragonfly is shown in Fig. 1.1 as another example [33]. At the perimeter of the wing, thicker vein structures are observed, which are expected to provide the overall structural rigidity. In the inner region, only a few main veins are found extending from the root to the tip (dashed lines), but other areas are filled with thin vein "free mesh" wing venation. These regions between the perimeter and the dashed lines have higher flexibility, which are able to form variable camber and improve flight performance. Similar ideas have been inspired from the observation of bats. The muscles in a bat's wings behave as a 'tuning' mechanism, enabling local flexibility changes that reduce or increase passively deformed camber of the bat's membrane-like wings [23].

Though most of the studies above deal with flapping wings and at different Reynolds numbers, the principle of flexibility tailoring should be applicable to fixed membrane and frame wings too. However, the numerical and experimental studies investigating the fixed membrane and frame wing flexibility distribution to date have been mostly limited to 2D studies or only involving chordwise flexibility. For example, Sun and Zhang [93] studied the effect of flexibility distribution on aerodynamic performance for a 2D membrane wing at Reynolds number 2,500 using a fluid structure interaction (FSI) method based on a high-fidelity fluid model with simplified finite element (FE) model. They noted that the flexible membrane introduces a passive camber beneficial for increasing lift, especially at higher angles of attack (AoA). The results also indicate that, even if 20% of the chord length of the wing is rigid at the leading-edge portion, the time-averaged lift is not significantly affected. However, inclusion of the same length rigid section on the trailing edge dramatically deteriorates performance. Fujita et al [41] conducted experimental studies into how the number of ribs and trailing edge would affect aerodynamic and deformation characteristics for rigid spar-and-rib frame and membrane wings. They found that the lift-to-drag ratio decreases as the number of ribs increase, and the flexibility of the trailing edge affected pitching moment characteristics. Understandably, with more ribs, the deformable regions of the membrane are reduced, the general flexibility of the membrane decreases, and then less lift is generated.

To extend the understanding and optimize the flexibility distribution of a 3D complex wing frame structure for thin fixed-wings, an efficient FSI model developed by Combes et al [29] is adopted in this research. It couples an advanced potential flow aerodynamic model with a corotational, large-deformation, frame-and-shell finite element structural model. However, this highly efficient FSI model was developed principally as a wing conceptual design tool since, by definition, potential flow methods do not consider viscous effects and thus cannot predict boundary layers, flow separation, or leading-edge vortex shedding [18]. As such, it is hypothesized that by performing the topology optimization using the adopted FSI model for the wing frame design, an optimal flexibility distribution can be achieved implicitly, which would ultimately lead to improved aerodynamic performance. To test this hypothesis, a higher-fidelity simulation is also required (large-eddy simulations (LES) in this proposed work) to confirm the outcome results as well as give a more fundamental understanding of the flow physics governing the aerodynamic performance of the UAV wings.

1.2 Streamlined body with leading edge (LE) damage

Surface roughness is found in a wide range of engineering applications as well as natural environments, and it plays a critical role in drag generation and momentum transfer (mass or heat). The broad engineering impacts of surface roughness, based on its associated flow phenomena, render it of great interest to the fluid mechanics community. Roughness idealised by very simple, regular shapes has been extensively studied, including square bars[79, 60], riblets with triangular cross sections [10, 22], cubes [27, 59, 108], wavy surfaces [21, 11, 66], and so on. Prior studies have demonstrated that the form drag is the dominant component,

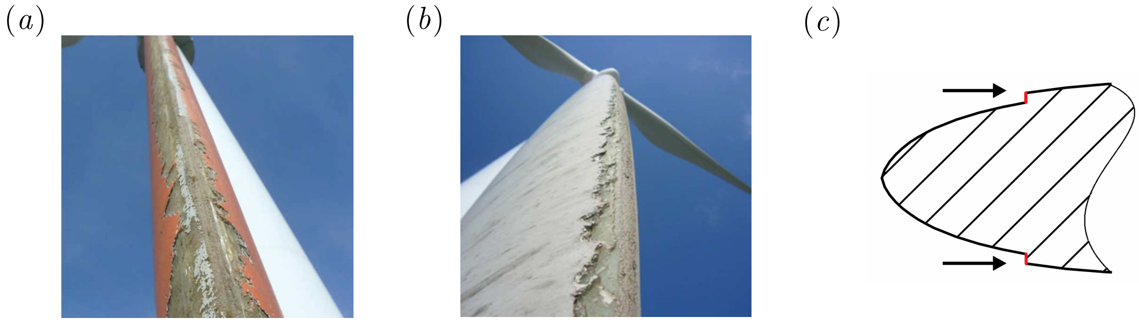

Figure 1.2. Wind turbine blade with LE erosion. (a) Field picture by Armour Edge [7]. (b) Field picture by Blade Partners [12]. (c) Schematic cross section view of wind turbine LE with erosion.

with friction only contributing a small portion to the total drag force [59, 66]. Moreover, it has been shown that geometric characteristics of roughness elements reveal significant impacts on the drag. For example, greater drag is observed when roughness elements are relatively isolated [60]. Accordingly, drag reduction is feasible by manipulating the shape and distribution of roughness elements in specific ways to reduce interactions between the overlying turbulence and the solid surface [10, 32, 43, 6]. In reality, the shape and distribution of roughness can be fairly complicated, and thus researchers have managed to come up with statistical measures to quantify some influential geometric characteristics of roughness [37, 38].

Although existing studies have contributed some understanding as to correlations between drag and the geometric characteristics of roughness, little research exists for curved surfaces with non-equilibrium temporal and/or spatial variations of the bulk flow. Despite this, roughness on streamlined bodies, ranging from the bio-fouling of ship hulls to the erosion of airfoils, is known to significantly affect operational performance. Inspiration for the work here stems from the wind energy industry, and specifically wind turbine blade erosion. Atmospheric particles, raindrops, hail, or sand frequently impact the rotating blades, causing erosion on the leading edge (LE) regions in particular [8]. Since wind turbine blades are usually laminated composite structures, severe damage on the LEs often appears as layer fracture. Indeed, an entire layer of material can be delaminated locally, as shown in Fig. 1.2(a, b), with small steps subsequently formed on both the upper and lower surfaces of the airfoil (Fig. 1.2(c)). Such steps can disturb the attached turbulent boundary layers and trigger flow separations on the LE, which may further interact with any separations on the trailing edges (TE), depending on the operating conditions. Such resulting unsteady flows can complicate the loading conditions on turbine blades and reduce aerodynamic performance. In the wind energy sector, for instance, compromised surface integrity of turbine blades has been found to significantly decrease energy production; and both experimental [87, 45] and numerical studies [95, 50, 46, 58] have been performed to quantify the effects of erosion on the aerodynamic performance of turbine blades. The associated large increases in drag and substantial lift losses at high angle of attack cause significant degradation in airfoil performance, leading to consequential losses in annual energy production.

A complicating issue in understanding, predicting, and addressing the effects of turbine blade damage is that their causes imply non-uniformity in their spanwise distributions. Furthermore, chordwise penetrations of damage may also vary according to local levels of erosion and delamination. The resulting strong three-dimensionality of flow associated with these complex airfoil geometry defects poses great challenges to understanding and predicting the flow behavior, and in efficiently estimating the reduced performance of damaged wind turbine blades. From the perspective of performing numerical analyses, such simulations require fine resolution to capture the small turbulent structures near the body, and thus also require lengthy simulation time for statistical convergence. Both the fidelity and computational time issues become more significant at higher Reynolds number. In addition, the complex physics governing the geometry-introduced pressure gradients and flow separations make the development of satisfactory and useful turbulence models fairly difficult [63, 68, 66, 31]. From an application perspective, performing such computationally expensive numerical studies has little direct benefit. Considering the aforementioned barriers, as well as the need for practical analysis tools in wind energy and other important applications, a reduced order model

(ROM) of the comparative drag that offers rapid evaluation with favorable accuracy is of great value, especially if it requires as input only the geometric description of damage.

The goal of this part of research, therefore, is to make the first step toward development of a simple model to estimate the drag of an airfoil containing surface defects. A streamlined bump taken from the literature is adopted for the present study, and LE erosion is idealized as a series of simple forward-facing steps, of varying chordwise location and spanwise length, superposed onto the streamlined bump. It is hypothesized that this useful ROM of total drag can be derived based on superposition of the effects of the individual constituent steps that, collectively, idealize LE damage (erosion) on the streamlined body. It is further hypothesized that the ROM is bilinear mathematically, in accordance with individual linear dependencies on the chordwise location and spanwise length, respectively, of each constituent step in the aggregated LE damage representation.

1.3 Research summary

To summarize the research background, needs, and hypotheses, proposed are investigations into the aerodynamic behaviors of passive airfoils associated with thin, flexible, fixed-wing UAVs, and airfoils for wind turbine blades having LE erosion. The presented research aims to provide suggestions for improvement from the aspects of airfoil geometric design based on revelation of new insights into the underlying flow physics. Following this Introduction, Chapter 2 provides literature reviews relevant to both applications fields. Chapter 3 introduces both an efficient FSI model and a high-fidelity computational fluid model (LES) used for the thin, flexible, fixed-wing UAV study. The validation of the fundamental model predictions against experimental results is also provided. A novel wing-frame flexibility optimization process is then introduced, which takes advantage of the high-efficiency FSI model. Once the optimum wing frame design is found, simulations for the original (baseline) wing and the optimum wing are conducted using the higher-fidelity computational fluid dynamics model. A test plan is then described and conducted that reveals the newly-discovered decoupled effects of the induced camber and spanwise bending. A detailed discussion of observations and new insights into flexible frame and membrane wing designs concludes the chapter. In Chapter 4, discussed first are the geometric modeling and basic development of the ROM for drag prediction of a streamlined bump with superposed surface defects idealised by steps. Following this, an "in-house" DNS code—which is applied later in the chapter to assess drag predictions, explain detailed flow behaviors, and justify the form of the ROM—is itself first validated. Once validated, the DNS are conducted on increasingly complex step configurations applied to the streamlined bump. The resulting flow fields are examined, and intriguing insights into the flow physics are reviewed, justifying the proposed simple bilinear mathematical form of the ROM. Subsequently, the ROM is applied to more complicated series of stepped geometries applied to the streamlined bump, the aim of which is to more closely emulate field damage of airfoils. The corresponding drag predictions are again compared to those by DNS, and limitations of the ROM are analyzed. A discussion of the key findings, and implications for applying the proposed ROM in practical applications, conclude the chapter. Finally, in Chapter 5, main contributions of this dissertation are summarized.

CHAPTER 2

LITERATURE REVIEW

2.1 Flexibility tailoring of bio-inspired UAV wing

Research to date has recognized that aerodynamic benefits can be gained by the adaption of flexible membrane wings onto UAVs. Passive deformation of flexible wings under aerodynamic load was found able to increase lift[101], decrease drag [2, 14], delay stall [42] and mitigate against strong gust encounters [48].

Since neither excessively flexible nor excessively rigid wings maximize aerodynamic performance [52], flexibility tailoring for such membrane wings is still of significant interest. Initially inspired by insect wings, some flexibility studies of flapping wings were reported. In a review paper by Gursul et al. [49], tailoring of both spanwise and chordwise flexibility was identified by researchers as a potential means to improve thrust for flapping wings. Local deformation and stiffness distribution of fly wings were studied by Wehmann et al. [97]. They suggested that the local deformation greatly depends on the inertial and aerodynamic forces, which are closely related to the wing stiffness distribution and geometry shape. A picture of the forewing of the dragonfly is shown in Fig. 1.1 as another example [33]. At the perimeter of the wing, thicker vein structures are observed, which are expected to provide the overall structural rigidity. In the inner region, only a few main veins are found extending from the root to the tip (dashed lines), but other areas are filled with thin vein "free mesh" wing venation. These regions between the perimeter and the dashed lines have higher flexibility, which are able to form variable camber and benefit the flying. Similar ideas have been inspired from the observation of bats. The muscles in a bat's wings behave as a 'tuning' mechanism, enabling local flexibility changes that reduce or increase passively deformed camber of the bat's membrane-like wings [23]. For fixed, flexible wings, Zhang et al. [107] performed experimental studies on frame-membrane planforms of differing aspect ratio wherein the wings were partitioned into several equally-sized, rectangular, rubber cells using varying numbers of aluminum ribs. The uniform cell aspect ratio for each wing, and the overall membrane pretension, were parameters considered in studying the aerodynamic performance. The conclusions were that the optimal cells had unit AR, and that preferred aeroelastic pretension ranged between 0.5 and 2. More recently, Sun and Zhang [93] studied the effect of flexibility distribution on aerodynamic performance for a 2D membrane wing at Reynolds number 2,500 using a fluid structure interaction (FSI) method based on a high fidelity fluid model with simplified finite element (FE) model. They noted that the flexible membrane introduces a passive camber beneficial for increasing lift, especially at higher angles of attack (AoA). The results also indicate that, even if 20% of the chord length of the wing is rigid at the leading-edge portion, the time-averaged lift is not significantly affected. However, inclusion of the same length rigid section on the trailing edge dramatically deteriorates performance. Fujita et al [41] conducted experimental studies into how the number of ribs and trailing edge would affect aerodynamic and deformation characteristics for rigid spar-and-rib frame and membrane wings. They found that the lift-to-drag ratio decreases as the number of ribs increase, and the flexibility of the trailing edge affected pitching moment characteristics. Understandably, with more ribs, the deformable regions of the membrane are reduced, the general flexibility of the membrane decreases, and then less lift is generated.

2.2 The effect of induced camber and spanwise bending

Considering that the flexibility of thin wings affects their aerodynamics, flexibility optimization implies attaining a preferred (or tuned) final, deformed geometry for the flexible wings when they are loaded aerodynamically. Among the potentially advantageous deformations of flexible membrane wings, spanwise bending and induced camber have been found to be two of the most influential characteristics. Studying spanwise deformation, Sachs and Holzapfel [84] showed that extreme dihedral (45 degrees) on a cambered pigeon wing plays an important role on lift and drag, particularly at low speeds. Wang and Liu [94] performed experiments to study the effect of wing flexibility on lift characteristics for delta wings. Three types of wing were designed and tested, including an elastic aluminum wing of 0.8 mm thickness, a relatively rigid aluminum wing of 3 mm thickness, and a flexible wing consisting of a carbon fiber outer frame and an extensible-film wing cover. The authors concluded that the flexible delta wing generated much greater lift due to its spanwise deformation and accompanying vibration. Paranjape et al. [77] found that dihedral angles can regulate sideslip during rapid turns and therefore allow for a wider range of stable turn rates while maintaining flight speed. An articulated micro air vehicle (MAV) studied by Oduyela et al. [72] included rigid but divided spanwise wing frames wherein adjacent segments were connected by variable compliance joints to offer high controllability of bending stiffness values and bending locations. The MAV prototype was validated experimentally and showed capability in alleviating disturbances to wind gusts. A similar design can be seen in the work of Gatto et al. [44], whose experimental investigation was performed for a wing with articulated winglets. Their methodology demonstrated adequate roll control and lift distribution tailoring. The aerodynamics effects of bending deflection on a flapping-wing MAV in hovering flight was studied experimentally by Forouzi et al. [39]. They showed that thrust could be enhanced up to 63% by introducing bending deflection.

Regarding camber effects in general, Pelletier and Mueller [78] carried out an experimental investigation on the lift, drag, and pitching moment difference for a series of flat and cambered plates. Their wind tunnel studies indicated cambered plates provide better performance in terms of aerodynamic characteristics. Gordnier et al. [48] developed a high-order Navier-Stokes solver that was coupled with a finite element plate model to understand flexible membrane wing performance in low Reynolds number (24,300) flow. Simulations were carried out for a wing of aspect ratio 2 at various AoAs, then the authors made comparisons between their numerical study and the experiments of Rojratsirikul [83] et al. Gordnier et al.'s work indicated that flexibility of the membrane wings resulted in the development of a mean camber, which they considered the primary factor in improved aerodynamic performance. Similarly, a fully coupled direct numerical simulation (DNS) based FSI tool by Yang et al. [100] was adapted to examine and understand the instantaneous flow field of flexible membrane wings (with camber), and favorable agreement with experiments was achieved. Bleischwitz et al. [13] conducted similar experiments to Galvao [42] using latex sheet wrapped on rigid steel leading and trailing edges. The performance of different AR wings was investigated, and it was found that passive deformation of the compliant membrane and its attendant camber provided significant improvement in lift. Vibration modes of the membrane and frame wings were also studied, and membrane oscillation induced by leading edge vortex shedding was found. Wrist and Hubner [98] performed experiments on flexible membrane UAV wings having 3D-printed polymer-based frames. Wings with cambered and flat frames were tested, with the results indicating that the net frame camber increases aerodynamic efficiency. Camber has also been seen to play an important role in flight control; a study done by Keidel et al. [56] proposed a novel camber-morphing wing design, which was studied numerically and experimentally. They demonstrated the capability of the morphing camber to vary lift, roll and pitch control.

Considering the above studies on the aerodynamic effects of spanwise bending and camber, an important issue that is ignored is that these two types of deformation are always coupled for UAV wing designs based on flexible frames and membranes. The above studies primarily focused on the effects of one of the deformation characteristics, i.e. the effects of either spanwise frame flexibility or the induced camber. A study that does combine both, as reported by Abudaram [1], was limited to relatively simple configurations; in their experiments, flexible membrane wings were studied when containing both positive and negative wing-frame stiffness gradients, but only along the spanwise direction. Nonetheless, no substantial difference was found between the positive and negative stiffness gradients for their specific wing designs.

Note that spanwise bending is predominantly determined by flexibility of the wing frame, whereas the induced camber stems from both the size (area) and the inherent flexibility of a constrained section of membrane. Lacking some means for active stiffness control of the membrane, flexibility 'tuning' of UAV wings is achieved by manipulating frame structures, which affects the individual compliant membrane regions that are constrained by the wing frame portions. Hence, dense frame structures (e.g. many ribs and spars) not only make the wing more rigid, but also create reduced area within which to develop induced camber. In contrast, sparse frame structures allow for greater extent of membrane inflation, but with an attendant increase in the overall wing flexibility.

Based on this correlation between spanwise bending and induced camber for flexible frame and membrane wings, this paper includes a numerical investigation that reveals both the combined and individual (de-coupled) static effects of spanwise bending and induced camber for a moderate-AR, optimum flexibility membrane UAV wing at Reynolds number 80,000. While it is acknowledged that dynamic behaviors of membranes can affect the aerodynamic performance of such flexible membrane wings (e.g. previously cited references [14, 13, 49, 93, 83, 48]).

2.3 The effect of the wind turbine leading edge erosion

Experimental studies [87, 45] and numerical simulations [95, 50, 46, 58] were performed to quantify the erosion effects on the aerodynamic performance of wind turbine blade. A large increase in drag and substantial lift loss at high angle of attack (AoA) cause a significant degradation in airfoil performance, which leads to the consequent loss in annual energy production (AEP). Gaudern [45] performed wind tunnel tests to evaluate complex erosion effect at different levels on wind turbine blade. The experiments are carried out at Reynolds number 2.2 millions and erosion geometry is obtained by scaling photographs of damage from real-world wind turbines of different ages. The degradation of performance is found on all wind turbine blades with erosion. An interesting point is revealed that a better airfoil design exists, which can lead to higher lift to drag ratio under both clean and eroded condition. Sareen et al. [87] conducted experiments using the airfoils with varying levels of leading edge erosion at three Reynolds number between 1 million and 1.85 million. They estimated that a relatively small LE erosion can cause 80% drag increase and 5% loss in AEP. As for moderate-to-heavy erosion cases, drag can increase up to 400–500%. With the coupled loss in lift, such defects can lead to 25% loss in AEP. Wang et al. [95] investigated the effects of leading edge erosion through numerical simulations. Two-dimensional incompressible Reynolds-averaged Navier–Stokes (RANS) simulations are performed for an S809 airfoil with pitting erosion on the LE, which uses semicircle cavities to represent the erosion pits. They found the aerodynamic coefficients are sensitive to the erosion area located at the first 15% of the airfoil in chordwise. From the other aspect of LE erosion study, recently, Kyle et al. [58] carried out 2D RANS simulations for NACA 64-618 airfoil at Reynolds number up to 11 millions. Instead of investigating the impact on the performance introduced by the LE erosion, they studied how a shield would be helpful to protect the LE and compensate the performance degradation. The results show that such shield would slightly increase the drag coefficient by 7%, but overall it is considered as minor impact on the aerodynamic performance.

However, the experimental approach inherently lacks the capability to probe the flow in a relatively small scale (e.g. near the erosion). Therefore, it can only provide an overall aerodynamic evaluation, but less detailed flow examination. As for the numerical approach, most of studies are still limited in two-dimensional, which makes broad assumptions that the erosion is spanwise identical and the flow motion along that direction is negligible. Unfortunately, this is not the case in reality. Since wind turbine blades are usually laminated using composite material, the severe damages on the LE often appear as fracture. As shown in Fig. 1.2, the entire layer of material is delaminated locally. Viewed from the cross section of damaged turbine blades (see Fig. 2.1, only show a region near LE), two small forward

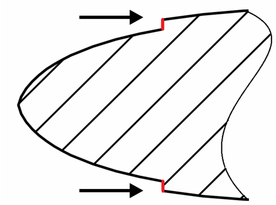

Figure 2.1. Schematic cross section view of wind turbine LE with erosion.

facing steps (FFS) are formed on the upper and lower side of the airfoil. Such steps are non-uniformly distributed along the span, and the location of the steps can also vary in chordwise depending on the erosion level. The complexity of the geometry qualifies the LE erosion as a three dimensional problem.

2.4 Adverse pressure gradient and forward-facing step

To understand the turbulent flow behavior around the 3D LE erosion is critical. The flow encounters a favorable pressure gradient (FPG) and local adverse pressure gradient (APG) at the same time on the pressure side of the airfoil. The FPG is due to the shape of the airfoil and the local APG is caused by the blockage of the FFS. Then the flow separates behind the step and reattaches after some distance. In the end, before it reaches the tailing edge (TE), the downstream flow undergoes another APG region introduced by the curved surfaces on the suctions side. In the field of wind energy, such knowledge can be adapted for providing better assessment of operating conditions and offering suggestions when the maintenance becomes necessary for the damaged turbine blades. Considering the geometry characteristic of erosion damage and its nonuniform distribution in spanwise, investigations of three-dimensional near-wall turbulent flow subjected to pressure gradients are demanded to examine the flow behaviors in detail. But performing numerical studies to investigate the coupled effects of pressure gradients and FFS for aerodynamic applications can be challenging. Such simulation requires fine mesh to capture the small turbulent structures near the body and also long simulation time for statistical convergence. Those requirements may become enormous hurdles, especially at a realistically high Reynolds number.

Alternatively, this problem could be addressed from the aspect of its basic components, FPG/APG and FFS. As seen in literature, one of the well established configurations to study the pressure gradient is with a bump placed on the wall [63]. By imposing FFS on the bump, the investigation of combined effects can be carried out. Though, either experimental or numerical studies are rather scarce on the flow encountering the combined effects in existing literature. However, individually, they have been extensively studied.

Separating and reattaching flow phenomena caused by FFS are investigated with various applications background. To study the wind flow in the vicinity of topological features such as coastal cliffs and escarpments, experiments on a polycarbonate and acrylic model are carried out in a water channel by Sherry et al. [88]. The dimension of the recirculation region formed downstream of FFS is characterised over a range of Reynolds numbers (1400–19,000). The turbulent mixing mechanisms which affects the reattachment distance are discussed. Hattori and Nagano [51] carried their investigations on the detailed turbulent structures of the boundary layer over a FFS. DNS are performed at three Reynolds number, and turbulent statistics as well as structures of boundary layers over the forward-facing step are present. Fang and Tachie [35] performed experiments for a forward-backward-facing step to study the turbulent separation characteristics. They stated that a higher approaching turbulence level tends to shift transition to turbulence from the rear part of the separation bubble to the leading edge.

As for most of atmospheric applications, including wind turbine blade of course, pressure gradient inherently come with the design. Delaying or suppressing the separation of turbulent boundary layer subjected to APG is of strong interest of these aerodynamic applications [63]. Webster et al.[96] conducted experiment and examined the turbulent boundary layer over a 2D bump. The boundary layer grew rapidly behind the bump apex, the mean velocity profile deviated from the law of the wall above the bump and the turbulent stresses were found to be increasing on the downstream side of the bump. Song and Eaton [92] presented experimental measurements for a turbulent boundary layer over a ramp with and without surface roughness. They found the separation region is larger in the rough wall case with earlier separation and later reattachment. And the normalized Reynolds stresses are less sensitive to the APG comparing with the smooth wall case.

CHAPTER 3

DECOUPLED EFFECTS OF SPANWISE BENDING AND INDUCED CAMBER[1]

Authors – Haoliang Yu, Umberto Ciri, Arif Malik and Stefano Leonardi

The Department of Mechanical Engineering, ECW31

The University of Texas at Dallas

800 West Campbell Road

Richardson, Texas 75080-3021

[1]Reprinted from *Yu, H., Ciri, U., Malik, A. S., & Leonardi, S. (2020). Decoupled effects of localized camber and spanwise bending for flexible thin wing. AIAA Journal, 58(5), 2293-2306.* https://doi.org/10.2514/1.J058669 with permission.

Investigated and revealed are new insights into the individual, decoupled effects of induced camber and spanwise bending on the lift, drag, and endurance for an optimum flexibility membrane-and-frame wing at Reynolds number 80,000. While previous studies into thin, flexible-wing designs for fixed-wing unmanned aerial vehicles have been shown to improve aerodynamic performance and delay the onset of stall, the individual contributions of localized induced camber and spanwise bending on the performance improvement have not been sufficiently examined. Furthermore, since the locally-induced camber and spanwise bending generally occur simultaneously, their decoupled effects are not well understood. This paper first introduces a wing frame optimization approach using a rapid fluid-structure interaction model to identify a wing flexibility design that maximizes aerodynamic endurance. A higher-fidelity, large-eddy simulation is then used for validation of the optimized wing flexibility, and to help explain both the coupled and uncoupled effects of the induced camber and spanwise bending that contribute to maximum performance. The formation of several locally-induced cambers at specific planform regions is found to create greater endurance (minimum power required) through favorable lift generation, in addition to reduced drag at relatively high angles of attack. Spanwise bending, however, is observed to be a noncontributing byproduct of the increased thin-wing flexibility. Detailed pressure distributions and instantaneous flow structure visualizations from large-eddy simulation provide new insights into the individual contributions of induced camber and spanwise bending while also justifying the optimum wing design.

The work here addresses a gap in the literature as to the understanding of the coupled and uncoupled contributions of bending and camber on the static-membrane aerodynamic effects. After introducing both an efficient FSI model and a high-fidelity computational fluid model used for the studies, validation of these models against experimental results is provided. A novel wing-frame flexibility optimization process is then introduced, which takes advantage of the high-efficiency FSI model. Once the optimum wing frame design is found, simulations for the original (baseline) wing and the optimum wing are conducted using the higher-fidelity computational fluid dynamics model. A test plan is then described and conducted that reveals the de-coupled effects of the induced camber and spanwise bending. A detailed discussion of observations and new insights into flexible frame and membrane wing design concludes the chapter.

3.1 Numerical Modeling

In the numerical study, two different fluid modeling techniques are adapted to balance the computational cost and capability in understanding separated bending and camber effects, the resulting fluid fields, and their influence on aerodynamic performance.

An efficient FSI model is used, as previously developed by Combes et al [29], which couples an advanced potential flow aerodynamic model with a corotational, large-deformation, frame-and-shell finite element structural model. Since for most high-fidelity computational fluid dynamics (CFD) models, resolving flow fields with high resolution in large domains presents excessive computational cost, potential flow models are advantageous to approximate performance for a large number of configurations and flight conditions. Moreover, they simply require definition of wing geometry and freestream/boundary conditions, allowing for highly efficient FSI modeling.

By definition, however, potential flow methods do not consider viscous effects and thus cannot predict boundary layers, flow separation, or leading-edge vortex shedding [18]. As such, the highly efficient FSI model was developed principally as a wing conceptual design tool. Considering this model lacks ability for detailed insight into the flow field, higher-fidelity large-eddy simulations (LES) have been performed to confirm preliminary results as well as give a more fundamental understanding of the flow physics governing the aerodynamic performance of the UAV wings. Discussion and qualification among high fidelity turbulence models have been presented by Celik [20]. Aside from DNS, which is widely agreed to be the most accurate numerical modeling technique, the LES are expected to provide the closest results to DNS but at dramatically lower computational cost. While Reynolds-averaged Navier-Stokes (RANS) is attractive because of its low computational cost, it lacks the capability to provide the instantaneous information on the flow structure [40].

3.1.1 Fluid-structure Interaction Model

The specific advanced potential flow method used in this work is based on that of Bramesfeld and Maughmer [18], wherein the wing and wake are modeled as continuous circulation and vorticity distributions using distributed vorticity elements (DVEs). So long as the flow remains attached, the method attains similar aerodynamic load resolution and accuracy as CFD but with significantly fewer elements; hence, the computational cost is drastically reduced. Good agreement on lift and drag predictions compared to experiments and other theoretical models has also been demonstrated [18, 16, 17].

The finite element structural model used in this work is formulated with frame and shell elements. Specifically, wing frame members are modeled using two-node, shear-deformable 3D frame elements having 6 degrees of freedom per node to capture bending, torsion, axial displacement, and transverse shear [30]. The flexible wing surface is modeled using shell elements that combine Felippa's OPT membrane element [36, 57] with the plate bending element by Batoz [9]. Since most thin UAV wing structures are designed to be planar with supports on the interior and perimeter, the frame and shell elements provide simpler structural formulation with reduced computational complexity and runtime than conventional isoparametric solid (continuum) elements. Moreover, they offer more flexibility in modeling thin UAV wings compared to membrane-only or combined membrane/Euler-Bernoulli (non-shear-deformable) plate bending formulations [29]. Large wing deformations resulting from high flexibility brings added challenges in structural modeling. Thus, a corotational algorithm is adopted to accommodate any nonlinear structural response [81, 82]. Validation with published works [57, 81] has been provided, with details found in [28].

3.1.2 High-fidelity Fluid Model

The adapted in-house LES model solves the filtered incompressible Navier Stokes and continuity equation. The numerical discretization is discussed in detail by Orlandi [73]. It employs the second-order centered finite-difference scheme for the spatial derivatives on an orthogonal staggered grid. The equations are advanced in time with a hybrid third-order, low-storage Runge-Kutta scheme, with linear terms treated implicitly and non-linear terms explicitly. The large sparse matrix resulting from the linear terms is inverted with an approximate factorization technique. Equations are advanced with the pressure at the previous step, which results in a non-solenoidal velocity field. A scalar quantity is used to project the velocity onto a solenoidal velocity and update the pressure in time. The presence of a body (e.g. the wing) is treated with the efficient immersed boundary method described in Orlandi and Leonardi [75]. This approach allows the solution of flows over complex geometries without the need for computationally intensive body-fitted grids. It consists of imposing a velocity equal to zero on the body surface, which does not necessarily coincide with the grid. Another condition is required to avoid describing the geometry in a stepwise way. This is done by discretizing the viscous terms taking into account the real distance between the grid point and the boundary of the body and not the grid spacing. The method has been extensively validated for flows over rough walls [75, 19, 103].

3.1.3 High-fidelity Fluid Model Validation for UAV Wing and Comparison with Experiment

This LES model described was successfully adopted for large-scale wind turbine studies [25, 86]. However, it has not been applied to study thin UAV wings, which present computational challenges, especially in using immersed boundaries. Validation with experimental data collected by Anada et al. [4] is therefore provided below.

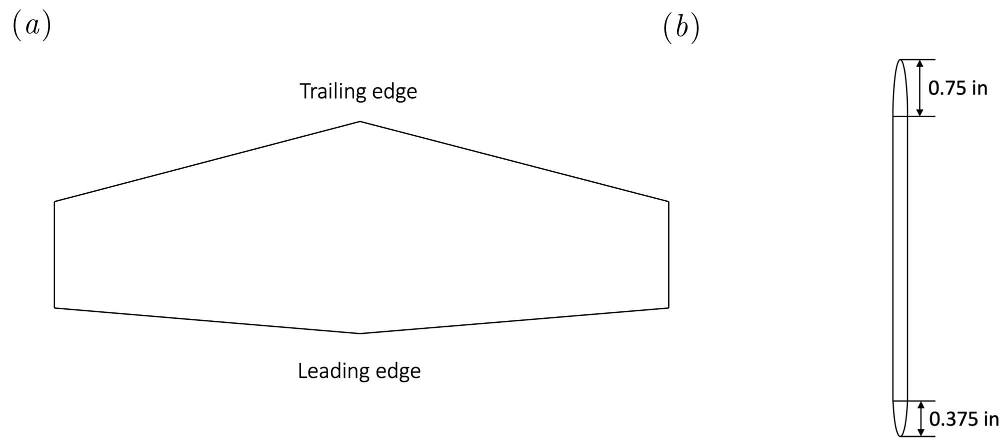

Figure 3.1. Reference wing geometry. (a) Top view. (b) Cross section view.

The experimental work done of Anada et al. [4] is one of the latest and most well documented studies found [78, 89, 69]. Wind tunnel data for ten flat-plate thin wings of multiple aspect ratios and taper ratios at Reynolds numbers ranging from 60,000 to 160,000 are provided in Anada's thesis [3]. Data collected for a specific wing tested at Reynolds 80,000 is chosen for comparison to validate the capability of the LES model. The wing has similar dimension and shape to that for the optimization study shown later in this work. The wing geometry is shown in Fig. 3.1, which is accurately defined in the LES using the ray triangle intersection technique [65].

Dimensions of the computational domain, normalized by 3.5-inch mean chord, are 12.288, 13.332 and 9.600 for X, Y and Z directions, respectively, as shown in the Fig. 3.2(a). The cross-section dimension is determined by the wind tunnel size then nondimensionalized by the 3.5-inch mean chord of the wing. Streamwise dimension is set large enough (more than 10 times mean chord) but less than the length of the wind tunnel test section to reduce computational cost. The grid resolution is $768 \times 256 \times 512$, which is determined from grid sensitivity studies; the adopted grid resolution has shown the ability to provide sufficiently accurate predictions at reasonable computational cost.

(a) (b)

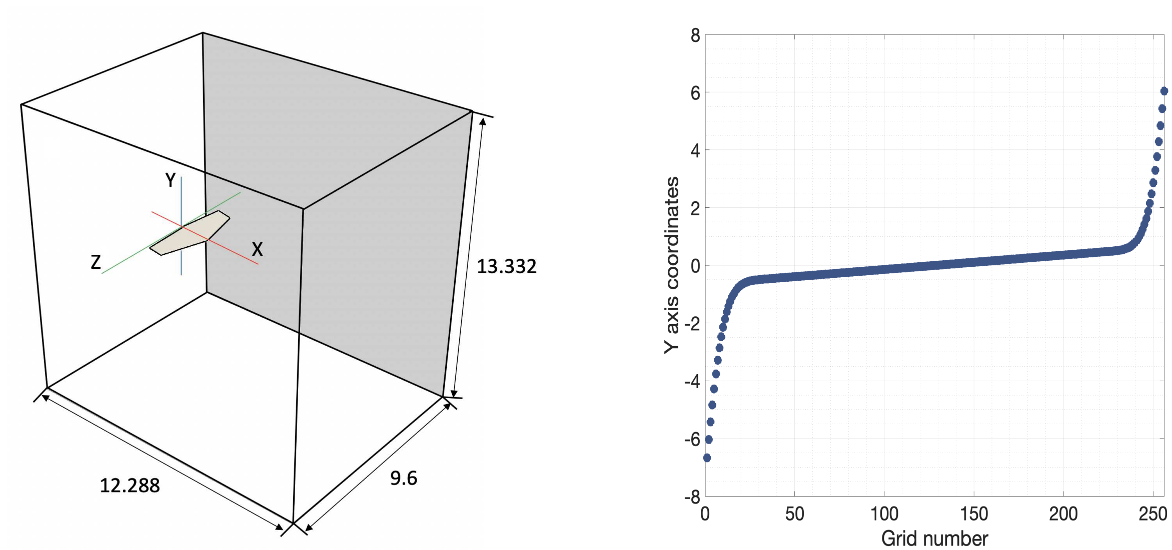

Figure 3.2. High-fidelity fluid simulation set up. (a) Simulation domain. (Dimensions are normalized by 3.5-in mean chord. (b) Y (vertical) direction grid resolution.

The streamwise and spanwise directions (X and Z, respectively) have uniform resolutions, whereas the Y direction resolution is finer in the center area where the wing is placed, and coarser elsewhere (see Fig. 3.2(b)). The wing is placed 3 chords from the inlet. No-slip conditions are imposed on the domain walls to mimic the wind tunnel. The inflow is uniform, and radiative boundary conditions are imposed at the outlet of the domain. A sub-grid model is used to represent the unresolved scales of motion. The classic Smagorinsky model [90] is used, with model constant set to $C_S = 0.09$. The van Driest damping function [34] is applied on the walls but not on the wing surface. The eddy viscosity for the points closing to the wing surface is computed using the actual distance from the wing rather than the mesh spacing.

Simulations for the validation were performed at AoA of -5, 0, 5, 8, 10, 12, and 15 degrees. The experimental data are concurrently plotted with simulation results in Fig. 3.3. Note that the LES shows good agreement with experiments, although the lift coefficient

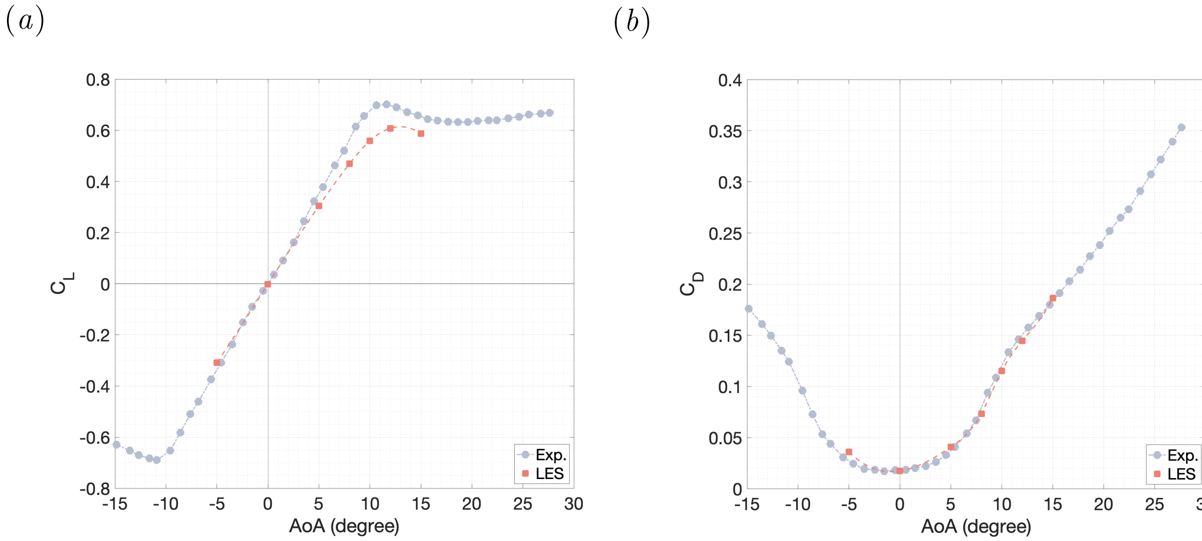

Figure 3.3. Reference wing geometry. (a) Coefficient of lift versus AoA. (b) Coefficient of drag versus AoA.

is under predicted at higher AoAs, and in general the results justify LES as a numerical approach.

Note that the final LES grid resolution is determined by gradually refining the grid until satisfactory agreement with experimental data is achieved. To illustrate this, a grid refinement study has been carried out by doubling the number of points in the Y direction (vertical direction in Fig. 3.2(b)) and maintaining the same resolution in X and Z at 10 degrees AoA (since the prediction at 10 degrees does not match the experiment as well, per Fig. 3.3(a)). Grid resolution in the Y direction is considered the most sensitive due to the numerical challenge in modeling the small wing thickness. As shown in Fig. 3.4 the results are only weakly dependent on the resolution. A modest improvement is observed from the coarsest grid (128 points) to the medium grid (256 points). Comparing the lift and drag coefficients of the meduim and fine grid (512 points), a very minor difference is observed. Thus a medium grid of $768 \times 256 \times 512$ is adopted as suitable resolution for LES predictions.

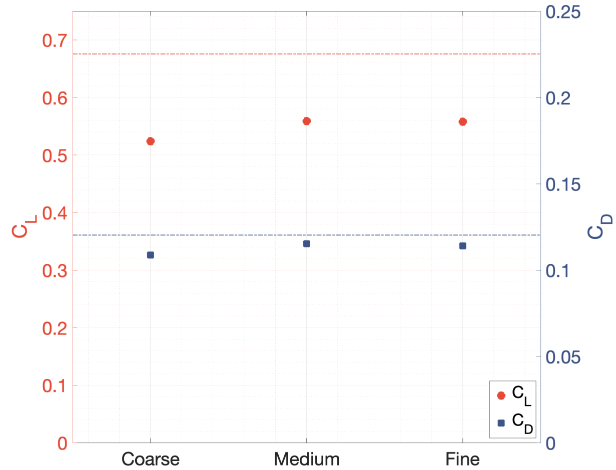

Figure 3.4. LES grid sensitivity study. Coarse: $768 \times 128 \times 512$, medium (adopted): $768 \times 256 \times 512$, fine: $768 \times 512 \times 512$. The dashed lines represent respective coefficients of lift and drag as interpolated from the experimental data for 10 degrees angle of attack.

3.2 Wing Frame Optimization

To achieve better aerodynamic performance, different optimization strategies were explored. For example, optimal hovering motion was pursued for flapping wings using adjoint-based algorithm [99]. And Local flexibility was tuned with an interesting morphing idea for fixed UAV wings [106]. In this present paper, the efficient FSI model serves as a conceptual design tool by providing the capability to rapidly explore a large number of wing configurations so as to help narrow the design domain. Exploiting this advantage, an optimization study was performed to minimize power required by maximizing the endurance parameter, defined in Eq. (3.1)

$$\eta = \frac{C_L^{\frac{3}{2}}}{C_D} \tag{3.1}$$

Where C_L and C_D are the total lift and drag coefficients, respectively. This definition of the endurance parameter assumes constant airspeed, altitude, and angle of attack. Increasing the lift and reducing the drag are pursued.

A related optimization work was done previously by Combes et al [29]. Using regularly spaced control points as design variables, they allowed continuous variation of the elastic moduli for both shell and beam elements to identify an ideal mechanical property distribution that resulted in maximum aerodynamic performance. Their approach provides general insights into the preferred wing flexibility distribution, but in practice it would present major manufacturing challenges. Therefore, in this work, a discrete frame segment optimization problem is selected as a more practical alternative. Introduced is a novel wing frame topology optimization approach that couples a genetic algorithm (GA) [47] with the efficient FSI model to identify the best 'skeletal' flexible frame configuration [105].

3.2.1 Panel Mesh Sensitivity

Prior to the FSI optimization process a mesh sensitivity study is conducted to determine appropriate resolution of the distributed vorticity aerodynamic panels since it is understood that lift and drag predictions are correspondingly affected. The same wing geometry as that studied experimentally in the literature [3] (see Fig. 3.1) is therefore simulated with varying numbers of panels at 5 and 10 degrees AoA and with Reynolds number 80,000. Sample aerodynamic meshes for 32, 128 and 512 panels (half wing) are shown in Fig. 3.5.

The aerodynamic panel mesh sensitivity results are shown in Fig. 3.6. Note that the potential flow approach underpredicts both the lift and drag when compared to the respective experimental values. Interestingly, with regard to lift prediction at both 5 and 10 degrees AoA, the potential flow approach achieves better agreement with the experimentally determined lift when fewer panels are used. In fact, the potential flow lift coefficient using 32 and 128 panels at 5 degrees, and 32, 128 and 512 at 10 degrees is closer to the experimental lift coefficient than that predicted by LES. However, as the number of panels is increased, the potential flow lift coefficient continually decreases then converges below the LES predicted lift coefficient, resulting in greater difference relative to the experiment than LES.

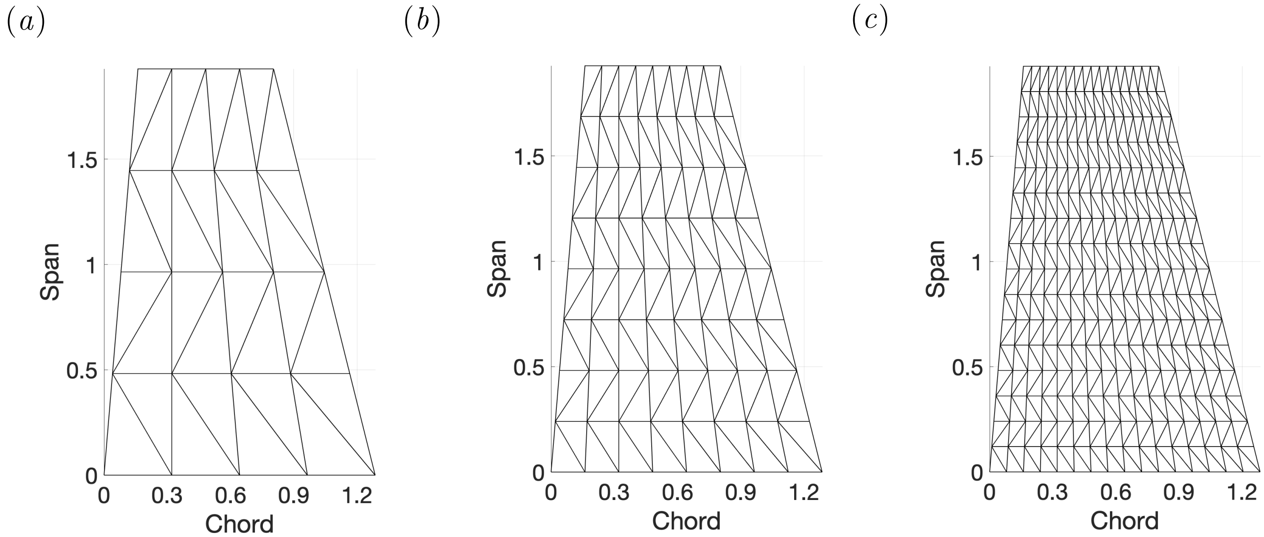

Figure 3.5. Aerodynamic mesh of reference wing geometry. (a) 32 panels. (b) 128 panels. (c) 512 panels.

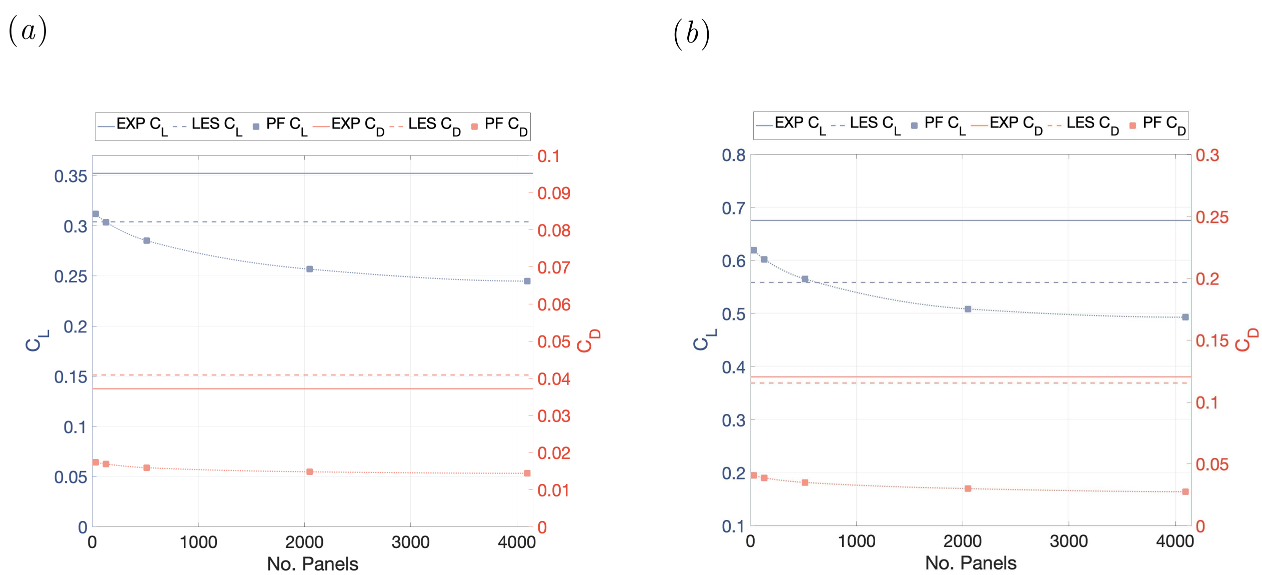

Figure 3.6. Aerodynamic panel mesh sensitivity study. (a) At 5 degrees AoA. (b) At 10 degrees AoA.

Regarding the drag prediction, upon initial inspection it appears detrimental for optimization that the potential flow method generates about a factor of 2 underprediction at 5 degrees AoA and factor of 3 underprediction at 10 degrees. Note, however, that the potential flow model assumes zero wing thickness. The same advanced potential flow model was shown to match lift and drag reasonably well compared to high-fidelity RANS at low AoAs (< 8 degrees) at Reynolds number 75,000 for a wing with similar geometry but a normalized thickness of 4.23×10^{-4} (actual thickness $0.0254mm$) [29]. As mentioned previously, in the current comparison the normalized thickness of the experimental reference wing is much larger at 3.37×10^{-2} normalized thickness ($3.81mm$). With much larger thickness, the 'thin-wing' drag prediction is not expected to match the experiment. Moreover, greater flow separation can be expected at the higher AoAs (i.e. 10 degrees), and even though this contributes to the drag, it is not captured by the potential flow model, suggesting the reason its drag prediction is worse at 10 degrees AoA.

Despite the underprediction of drag by the potential flow method, note that it actually will not detrimentally affect the optimization process when identifying wing configurations with preferable endurance parameter. This is because all wing flexibility configurations are simulated under the same thin-wing assumption with lift and drag consistently underpredicted. In other words, the maximum predicted endurance parameter still represents the maximum for each flight condition, but it is simply a scaled value relative to the true value. Nonetheless, to better understand the thickness-to-drag sensitivity of the potential flow model, additional LES simulations are performed for varying wing thickness, as shown later in this paper.

The time consumed for each single potential flow simulation at 5 degrees AoA is tabulated in Table 3.1 (single work station, XEON CPU, 16G RAM). The computational cost remains relatively constant at different AoAs. As the number of panels used is increased, computational cost grows significantly. This cost is further amplified when the potential flow

Table 3.1. The computational cost for potential flow method with different numbers of panels.

No. Panels	32	128	512	2048	4096
Time(s)	3.5	23.6	330.2	5867.4	27099.9

based FSI is coupled to an optimization process. For this reason, the 32-panel mesh is used for the FSI optimization, and while it does not represent a converged prediction, it does achieve the closest agreement to the published experimental results. In addition, it serves the main purpose of the optimization algorithm, which is to rapidly explore a large number of wing configurations so as to narrow the very large design domain.

3.2.2 GA Topology Optimization

The basic initial wing configuration to be optimized is shown in Fig. 3.7(a). Span of the half wing is 8 inches, it has a 4-inch root, and 2-inch tip. The half wing frame has three inner ribs, which form connections between three opposing intersection points on the leading and trailing edges. Two inner spars connect opposing intersection points on the wing root and tip. Frame segments between any two intersecting points that do not both lie on the wing perimeter are defined as ‘parts’. The intent during optimization is to remove or maintain frame part(s) to influence the local flexibility of both the frame and the constrained membrane. For the specific wing frame in Fig. 3.7(a), there are 17 parts that can be removed or kept, but with the constraint that at least one end of remaining continuous ‘strings’ of frame parts is connected to the perimeter so that no internal strings of frame parts ‘float’ inside the wing. A ‘breadth first search’ (BFS) algorithm is employed to ensure this requirement, details for which can be found in [105]. Note that even for such a simple initial frame configuration, a total of 131,071 unique design adaptations are possible.

Prior to optimization, the efficient FSI simulation was run for the wing shown in Fig. 3.7(a) at 5 degrees AoA and Reynolds number 80,600. The corresponding finite element mesh and

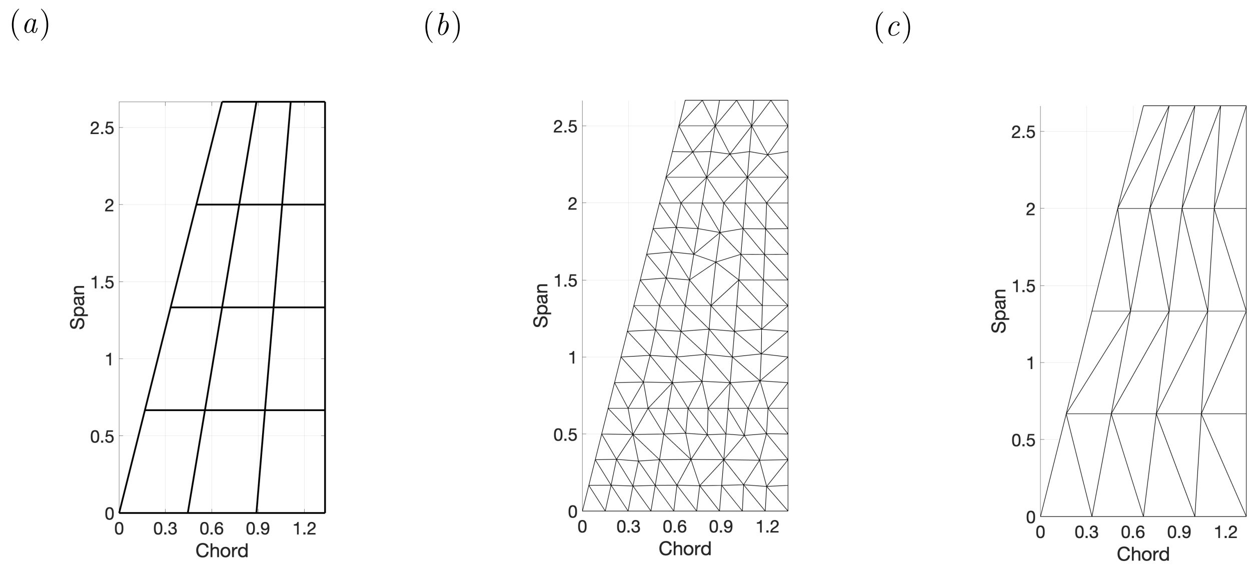

Figure 3.7. Original wing simulation set up in FSI. Wing dimensions are normalized by mean chord. (*a*) Original wing configuration. (*b*) Coarse FE mesh. (*c*) Aero. mesh w/ 32 panels.

aerodynamic grid of triangular DVE panels are shown in Fig. 3.7(*b*) and Fig. 3.7(*c*), respectively. Figure 3.8 shows the resulting deformed geometry when all frame parts are maintained. This configuration is considered as the 'original' (baseline) design; it is subsequently compared to an optimum-frame wing as well as derived wings constructed to examine the de-coupled contributions of induced camber and spanwise bending. For this original baseline wing, the advanced potential flow prediction of the FSI simulation gives $C_L = 0.3475$ and $C_D = 0.0166$, from which the endurance parameter η is computed as 12.3657.

The frame optimization process was executed under the same flow condition with GA population size of 51 and for 30 generations. Figure 3.9(*a*) shows the endurance parameter trend during optimization. The circular symbols in the plot represent the best endurance parameter achieved in a single generation whereas the triangular symbols represent mean values of all individuals within each generation. Note that the optimization terminated when there was no change in the best value after 5 generations (set by user). The mean endurance parameter value increased from about 13.6 to 14.7, with the best value achieved being 14.7707.

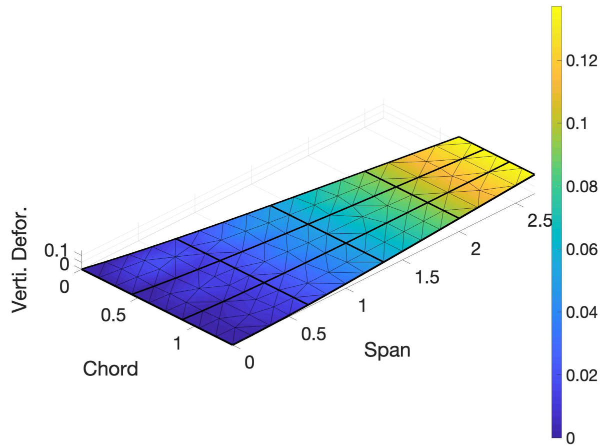

Figure 3.8. Original wing deformation contour predicted using the efficient FSI model. The color represents vertical deformation. All units are normalized by mean chord.

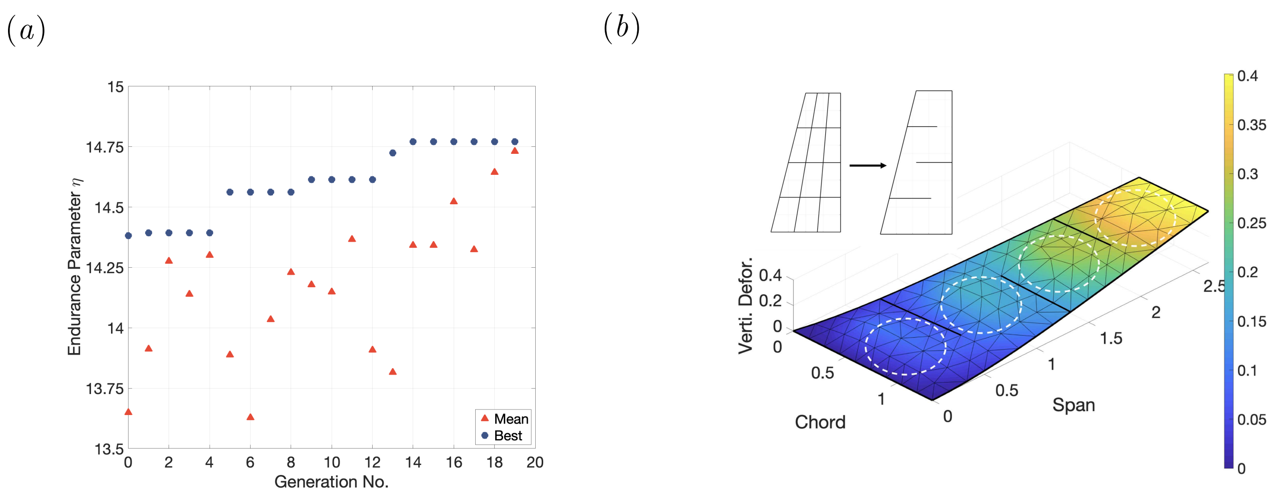

Figure 3.9. GA optimization process. (a) GA optimization history. (b) Optimum configuration with deformed shape. The color represents the vertical deformation. All units are normalized by mean chord. Noticeable 'bubble' deformations are encircled by dashed lines.

The resulting deformed wing geometry for the optimum configuration is shown in Fig. 3.9(b). Upon removal of specific frame parts during optimization, the overall flexibility of the wing is increased, which explains the larger wing tip deflection compared to the original design (Fig. 3.8). Four noticeable membrane deformation 'bubbles' (circled in the Fig. 3.9(b)) are observed on the wing due to reduced membrane constraints accompanying the frame part eliminations. The optimum endurance parameter, $\eta = 14.7707$, is based on the advanced potential flow prediction giving $C_L = 0.4905$ and $C_D = 0.0233$.

Note that both the lift and drag coefficients as well as the endurance parameter all increased for the optimum wing. In relative terms, the drag coefficient and lift coefficient increased about 40%, while the endurance parameter increased about 13%.

3.3 FSI Model Verification with LES, and Decoupling of Camber and Bending Effects

In order to verify the outcomes of the optimization using the efficient FSI model, simulations using deformed shapes of both the original and optimum wings are performed using high-fidelity LES. Since it is acknowledged that resolution of the aerodynamic panels in the potential flow model directly affects resolution of the resulting pressure distribution (and thus the loading condition for the FE structural model), both the FE mesh and aerodynamic mesh for the optimum wing are refined, as shown in Fig. 3.10, to provide the deformed wing shape for simulation and verification by LES. The LES simulation conditions with the optimum deformed wing shape are identical to those cited earlier with Fig. 3.2(a) for validation of the LES model against previously published experimental results.

Since the required wing thickness in LES is not physically defined in the FSI model (due to the thin wing assumption), two different thicknesses are examined in LES. One wing has 0.05 thickness (as normalized by mean chord), which is the same as that used earlier for the

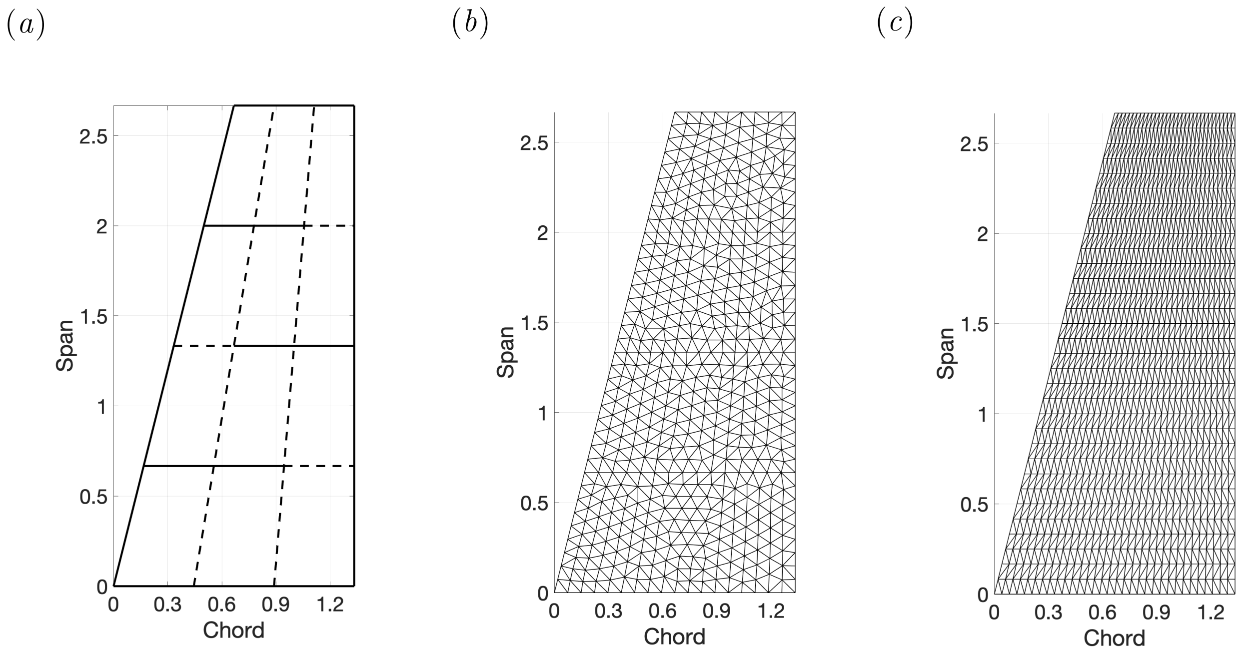

Figure 3.10. Optimum wing simulation set up in FSI. Wing dimensions are normalized by mean chord. (a) Optimized wing configuration. (b) Fine finite element mesh (995 triangular shell elements and 213 beam elements). (c) Aerodynamic mesh using 2048 panels.

LES validation. The other wing, having 0.03 normalized thickness, is used for comparison purposes to study the effect of thickness on the LES-predicted aerodynamic performance.

Figure 3.11 shows perspective and frontal views of the deformed optimum (OPT) wing and the deformed original (ORI) wing as predicted earlier by the efficient FSI model (with fine FE mesh and 2048 aerodynamic panels) which is simulated using LES.

Results of the LES, shown in Table 3.2, indicate that the OPT wing creates greater lift, greater drag, and yields a larger endurance parameter as compared to the ORI wing. This verifies the trends predicted by efficient FSI model. As expected, however, while an increase in endurance parameter for the optimum wing is also identified by LES, significant differences in the values of lift and drag coefficients predicted by LES and the FSI's potential flow method do exist. As discussed earlier, it has already been shown that the potential flow method with zero wing thickness consistently underestimates drag as well as lift to a lesser extent. From the LES results in Table 3.2, it is also observed that, as wing thickness is

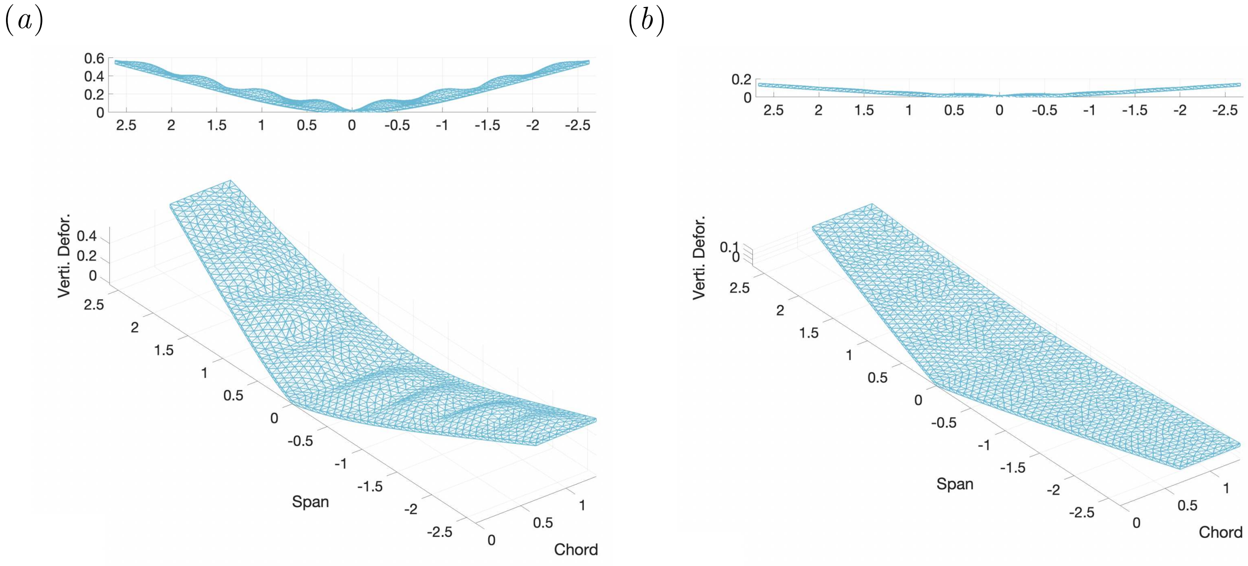

Figure 3.11. Perspective and frontal views of deformed wing geometries (0.03 normalized thickness) for use in LES. (a) Deformed optimum (OPT) wing. (b) Deformed original (ORI) wing.

reduced by 40% (from 0.05 to 0.03), the drag correspondingly decreases about 15%. This confirms the important role that wing thickness plays on drag, and also accounts for some of the difference between the experimental and potential flow results seen earlier in Fig. 3.6.

Table 3.2. Simulation results comparison between the FSI's potential flow method (PF) and LES. Note: '2048F' indicates 2048 distributed vorticity panels (Fig. 3.10(c)) with fine finite element mesh (Fig. 3.10(b))

Method	Resolution	Configuration	C_L	C_D	η
PF	2048F	OPT	0.4933	0.0231	14.9987
LES	0.05	OPT	0.6831	0.1005	5.6177
LES	0.03	OPT	0.6942	0.0847	6.8289
PF	2048F	ORI	0.2880	0.0141	10.9496
LES	0.05	ORI	0.4440	0.0903	3.2763
LES	0.03	ORI	0.4122	0.0649	4.0777

To better understand the differences in lift predictions between the efficient FSI and the LES, a comparison of net pressure distributions is provided in Fig. 3.12 (for OPT wing) and in Fig. 3.13 (for ORI wing). For both wings, the advanced potential flow model achieves

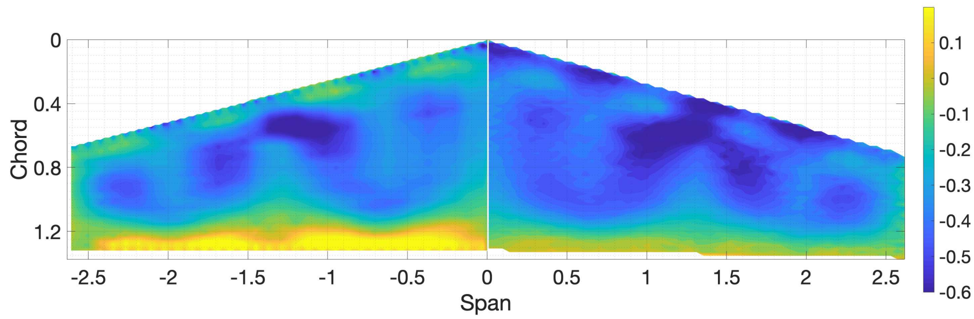

Figure 3.12. Nondimensionalized net pressure distribution on the optimum (OPT) wing predicted by potential flow model using 2048 panels (left), and LES (right). Wing dimensions are normalized by mean chord.

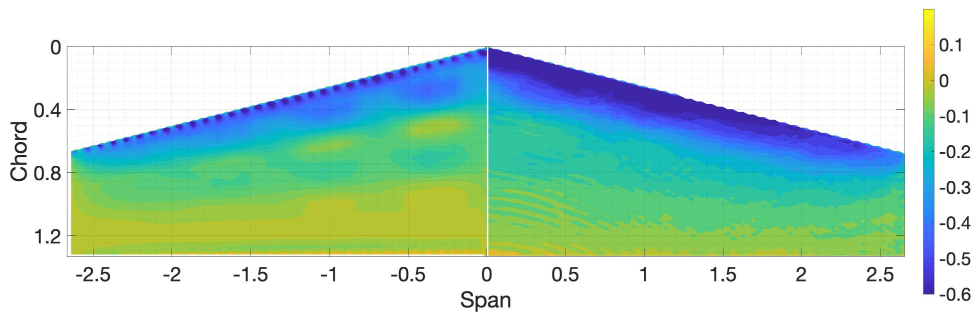

Figure 3.13. Nondimensionalized net pressure distribution on the original (ORI) wing predicted by potential flow model using 2048 panels (left), and LES (right). Wing dimensions are normalized by mean chord.

reasonably similar pressure pattern to that obtained by LES, despite the huge computational cost difference (each LES requires 4 days using 64-core parallel processing). However, differences in magnitude of the net pressure are still observed, which explains the under-prediction of lift using the potential flow method. Considering the OPT wing in Fig. 3.12, it is seen that the 'curled' distribution pattern of the larger pressure difference (darker blue region) matches with the optimized wing frame configuration, shown earlier in the Fig. 3.9(b) and Fig. 3.10(a) in which the locally induced camber produces larger magnitude net pressure.

Recall from the frontal views for the optimum wing (OPT) versus the original wing (ORI) in Fig. 3.11, two main geometrical differences were readily observed. The first being the larger tip deflection (spanwise bending) of the optimum wing, which arises due to the removal of frame parts so as to increase the overall wing flexibility. The second being the localized, convex, induced-camber deformations, i.e. ‘bubbles’. Compared to the original wing, the membrane of the optimum wing develops enlarged bubbles because the removal of its frame parts eliminates the localized (peripheral) membrane constraints. While the original deformed wing does exhibit such bubbles, they are much smaller in comparison.

As pointed out in the introduction, both spanwise bending and induced camber are known to be important aeroelastic effects in flexible frame and membrane type UAV wings. With such wings these two deformation characteristics always occur simultaneously. The challenge in studying these coupled behaviors is to understand how each contributes separately to the combined effect. To facilitate this understanding, a third wing geometry (INT) is created and is shown in Fig. 3.14(a). This wing does not represent the result of any wing design using the FSI model. Instead, it is created by ‘manually’ removing the bubble deformations from the deformed optimum wing shape. Geometrically, the new wing has the same spanwise bending profile and tip deflection as the optimum wing while having a very smooth and flat surface similar to the original wing. It is thus considered to have an ‘intermediate’ deformation characteristic that is in between the original and optimum deformed wing shapes. For further comparison, a rigid flat plate (FLT) wing (that also removes the spanwise bending) is also created and as shown in Fig. 3.14(b).

Thus, the four different deformed wing shapes introduced above are studied to help understand how the spanwise bending and induced camber bubbles contribute separately to the combined beneficial effect of improved aerodynamic endurance. Hereafter, the three-letter acronyms ORI, OPT, INT, and FLT are adopted to refer to the different deformed wing shapes. To clarify the nomenclature, note that the optimum wing (OPT) and the original (baseline) wing (ORI) are the final deformed shapes predicted by efficient FSI simulation. ORI and OPT differ as a result of their different frame structure configurations due to the

(a) (b)

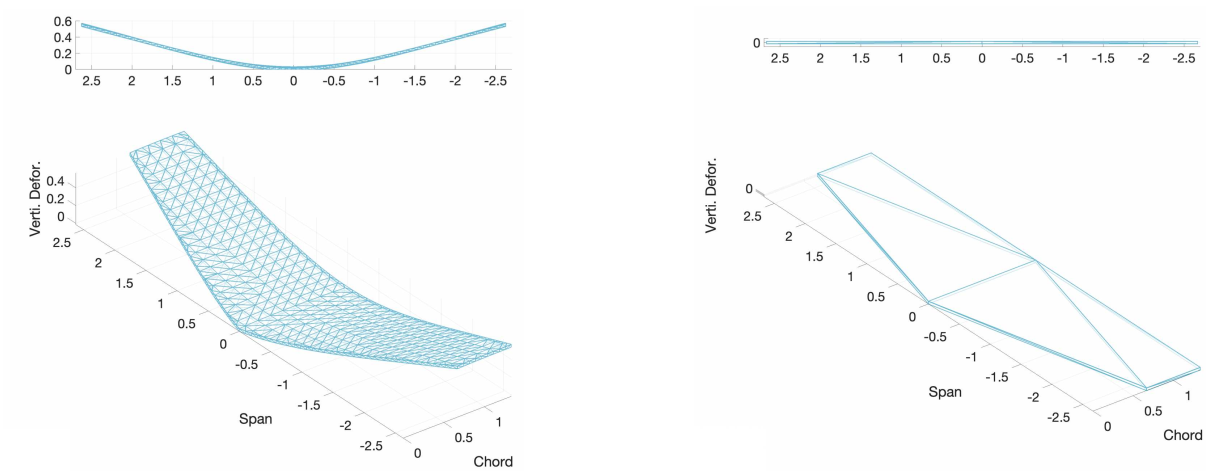

Figure 3.14. Perspective and frontal views of additional wing geometries (0.03 normalized thickness) for comparison in LES. (a) Intermediate (INT) wing. (a) Flat (FLT) wing.

GA optimization (see Fig. 3.7(a) and Fig. 3.10(a)). The intermediate wing (INT) is inherited from the OPT wing by manually removing induced camber bubbles, while the rigid flat plate wing (FLT) is similar only in terms of its planform and dimensions. Thus, INT and FLT actually have no associated inner frame structure, but they share the same 'ancestor' as the ORI and OPT wings. Note that when investigating the aerodynamics of the four wing shapes using LES in the studies below, each wing is considered rigid, including when the AoA is varied in those simulations which will be discussed later.

Simulations were performed at Reynolds number 80,000 and AoA 5 degrees. Coefficients of lift and drag are computed and plotted in Fig. 3.15. The OPT wing's superior lift-to-drag ratio (dashed lines in Fig. 15) is clearly seen no matter which wing thickness is used.

In general, the ORI, INT and FLT wings show similar performance for each wing thickness, with the thicker wing indicating small increases in lift but larger increases in drag. In comparing the OPT and INT wings, the presence of the locally induced camber bubbles is the only geometric difference; nonetheless, these local cambers lead to significant increase in lift coefficient at the expense of a relatively small increase in drag. Referring back to the

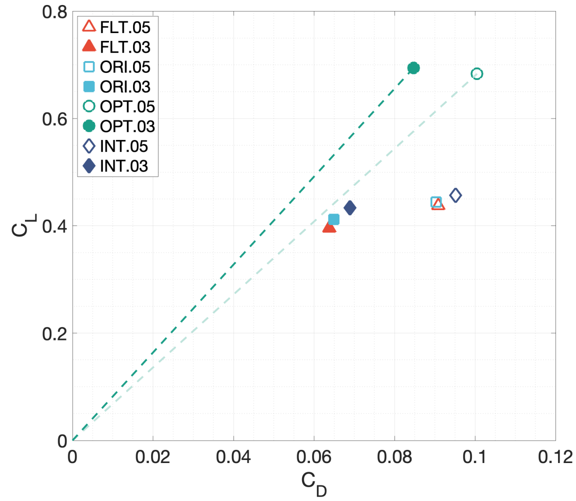

Figure 3.15. Coefficient of lift versus coefficient of drag for ORI, OPT, FLT, and INT wings for two different thicknesses as predicted by high-fidelity LES.

wing net pressure distribution in Fig. 3.12, a higher pressure difference is produced where the bubbles are formed, leading to greater lift generated in those regions. The localized camber bubbles therefore appear to be influential for efficient generation of lift. The accompanying drag increase for the OPT wing versus the INT wing (no bubbles) stems mainly from the greater lift and partially from increased skin friction due to the more convex airfoil shape.

The spanwise bending deformation is not found to significantly affect either drag or lift. From the dihedral angle point of view, a similar observation was discussed by Sachs and Holzapfel's [84]. They found a 22.5-degree dihedral did not create an obvious effect on either lift or drag, while a dihedral angle as large as 45 degrees decreased lift and significantly increased drag. The phenomenon is particularly evident at high AoA ($>$ 10 degrees). In the case here, the INT wing has just 12 degrees dihedral angle and is simulated at 5 degrees AoA.

To further understand the performance on the four thinner wings, additional LES were performed at various AoAs (based on pitch changes with same rigid geometries). The results are shown in Fig. 3.16. In general, INT, ORI and FLT wings exhibit similar performance,

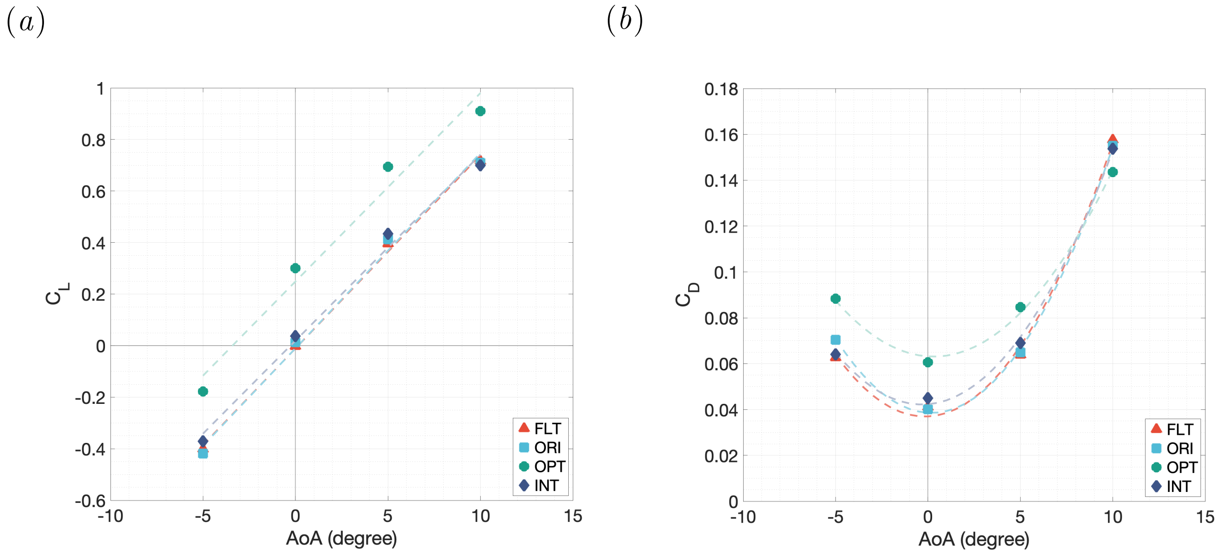

Figure 3.16. Coefficients of lift and drag versus AoA for ORI, OPT, FLT and INT wings as predicted by high-fidelity LES. (a) Coefficients of lift versus AoA. (b) Coefficients of drag versus AoA.

and the lift curve of the OPT wing is shifted upward. Also, the OPT wing always creates greater drag than the other wings at lower AoA, but interestingly this circumstance inverts at 10 degrees AoA. The reason for this is discussed below. Note that all four wings perform better at 5 degrees AoA, and comparing the lift trend lines shown it is clear that 5 degrees AoA is the angle at which the wing frame was optimized. A second order polynomial fit is given in Fig. 3.17, made according to Eq. (3.2) [5] based on the data for the AoA sweep and the corresponding drag polar for each wing.

$$C_D = C_{D,min} + \frac{(C_L - C_{L_{min\,drag}})^2}{\pi e AR} \tag{3.2}$$

In Fig. 3.17, increased slope for the tangent line indicates greater efficiency of the wing, and intersection of tangents to the corresponding parabolic curve represents the best theoretically achievable aerodynamic performance for the given wing. It is seen that all four wings at 5 degrees AoA operate near their respective best theoretical performance (a single tangent is shown for FLT, ORI and INT since they would nearly overlap.). The OPT wing,

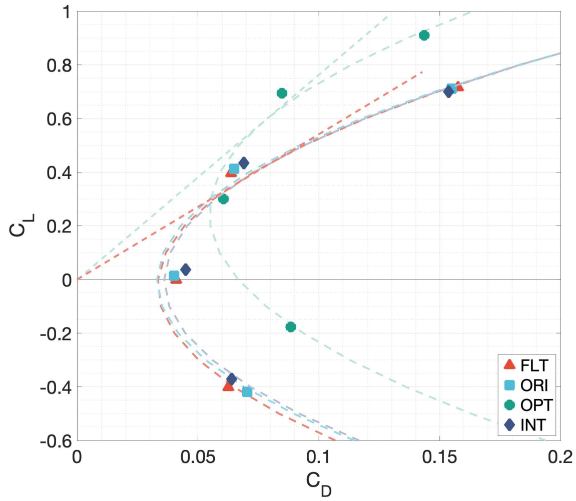

Figure 3.17. Drag polar for FLT, ORI, OPT, and INT wings based on LES prediction. Dashed lines are tangent to the respective parabolic curves from the origin.

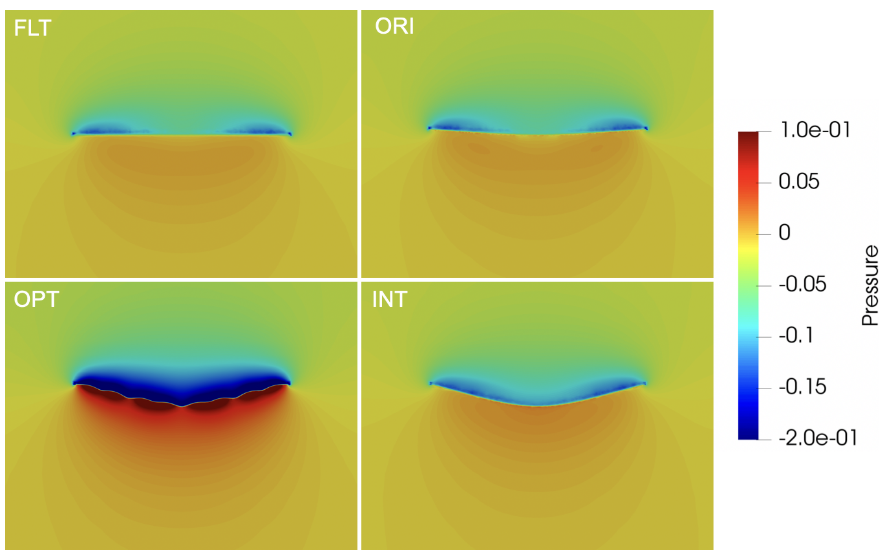

Figure 3.18. Pressure distribution visualization at near middle chord for ORI, OPT, INT, and FLT wings based on LES prediction.

however, is indeed confirmed as being optimized since at no AoA value does the ORI (FLT or INT) wing achieve a better efficiency than the OPT wing.

Figure 3.18 shows contours of the pressure distributions from LES at chordwise location X = 1 (near mid chord) for the ORI, OPT, INT, and FLT wings. From the figure, it is straightforward to infer why the OPT generates greater lift; a connected weak pressure region is seen above the wing, and strong pressure region exists beneath the wing. This large difference in pressure correspondingly creates larger upward force.

$$\mathbf{J} \equiv \nabla \vec{u} = \begin{bmatrix} \partial_x u_x & \partial_y u_x & \partial_z u_x \\ \partial_x u_y & \partial_y u_y & \partial_z u_y \\ \partial_x u_z & \partial_y u_z & \partial_z u_z \end{bmatrix} \tag{3.3}$$

$$\mathbf{S} = \frac{\mathbf{J} + \mathbf{J}^{\mathrm{T}}}{2} \tag{3.4}$$

$$\boldsymbol{\Omega} = \frac{\mathbf{J} - \mathbf{J}^{\mathrm{T}}}{2} \tag{3.5}$$

Returning now to the earlier observation from in Fig. 3.16(b) in which the OPT wing is found to create more drag than the other wings at 5 degrees AoA, but less drag at 10 degrees. To better understand and explain this, coherent structures (vortices) are visualized in Figs. 3.19 and 3.20 for the OPT and INT wings at 5 and 10 degrees AoA, respectively, using the λ_2 vortex criterion [55]. λ_2 is one of the eigenvalues of $\mathbf{S}^2 + \boldsymbol{\Omega}^2$ ordered such that $\lambda_1 \geq \lambda_2 \geq \lambda_3$, seen in Eqs. (3.3) to (3.5), $\mathbf{J}$ is the gradient velocity tensor, $\mathbf{S}$ and $\boldsymbol{\Omega}$ are symmetric and antisymmetric parts of $\mathbf{J}$. (since the INT, ORI and FLT have fairly similar performance, only INT is shown.)

At 5 degrees AoA (Fig. 3.19), flow remains attached, and no obvious coherent structures are observed above the wing. Stronger wing tip vortices are generated by the OPT wing compared to the INT wing due to the higher lift (net pressure) produced by OPT wing. Such strong tip vortices contribute to higher drag. However, the dominant vortex structures are different at 10 degrees AoA as shown in Fig. 3.20. The flow still remains attached, and strong tip vortices are observed for both OPT and INT wings, but note that the INT wing has stronger and greater number of vertical structures generated in the wake region than

(a) (b)

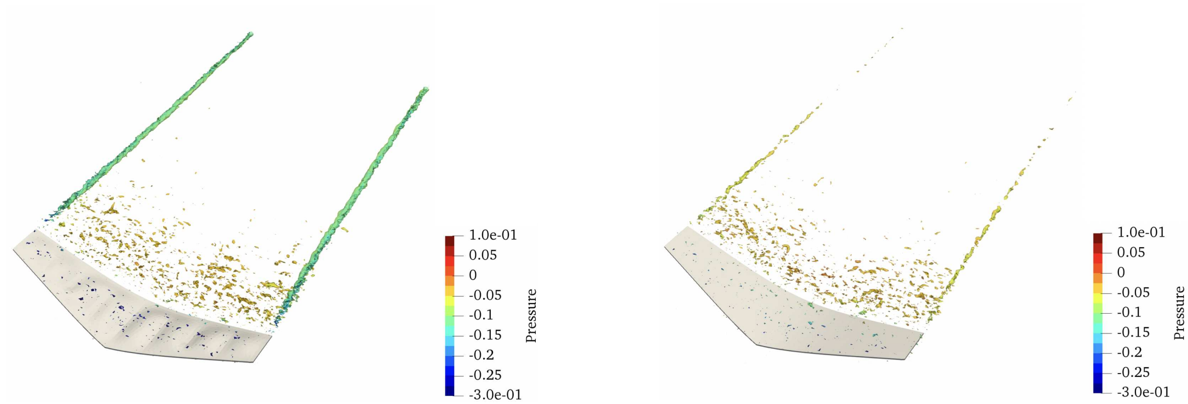

Figure 3.19. Vortices visualization at 5 degrees AoA using vortex λ_2 criterion. (a) OPT wing. (b) INT wing.

(a) (b)

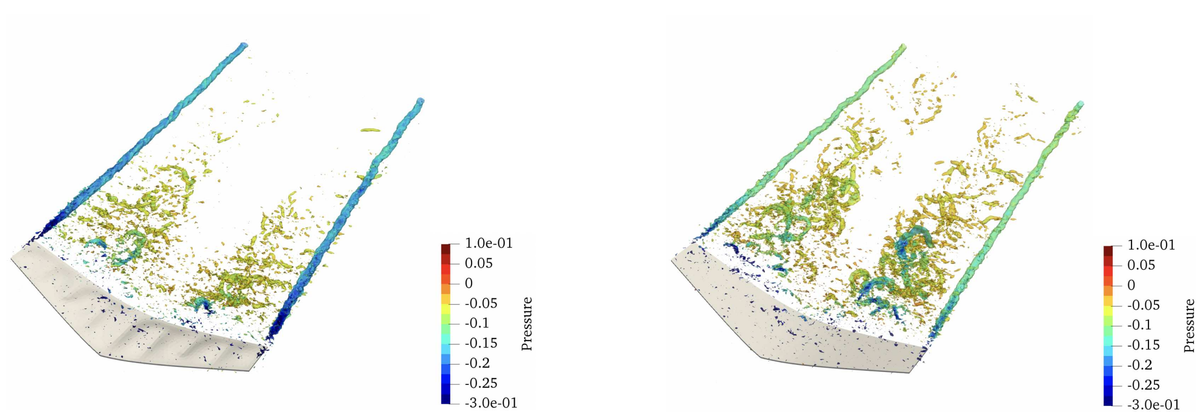

Figure 3.20. Vortices visualization at 10 degrees AoA using vortex λ_2 criterion. (a) OPT wing. (b) INT wing.

the OPT wing, thus contributing to higher drag. This explains and confirms the previous observation in Fig. 3.16(b) where locally induced cambers of the OPT wing are seen to generate fewer vortices in the wake region at high AoA, thereby reducing drag.

3.4 Chapter Discussion

Simple spanwise bending alone appears not important in generating lift or drag, but when occurring simultaneously with localized camber bubble type deformation, improved aerodynamic performance can clearly be seen, but this is due to the camber bubbles rather than the bending. Even though the optimization algorithm implemented in this work is in fact 'blind', the efficient FSI model applied retains sufficient fidelity for the process physics so as to identify an improved wing flexibility design that can indeed be readily justified via pressure and flow field examination using LES.

At first glance, the optimization procedure with the frame and membrane design may be viewed as removing unnecessary frame parts so as to increase local flexibility and achieve larger wing tip deflection, with the attendant passively induced camber that would be expected. On the contrary, it is now appreciated that constraining the membrane regions with frame parts in a very specific pattern so as to enable development of a suitable, targeted induced camber deformations is the motivation behind the optimization. The larger wing tip deflection is actually a byproduct of the membrane bubble deformations. Noticing that the GA optimization was allowed to remove any parts in any combination inside the wing perimeter as long as the perimeter attachment constraint was satisfied, it is evident that formation of several smaller bubbles is preferable to a single (or fewer) larger bubble(s). This means that localized bubble deformations are beneficial for increasing lift, but that they also need to be limited to some suitable size and number. Moreover, the actual locations of where such localized deformations should be generated, and to what magnitude, may be critical (for example, near the leading edge or near the trailing edge). As illustrated in the wing designs shown in this work and in previous studies, the greater trailing edge flexibility is generally preferred [29, 105], while the leading edge is required to be relatively stiffer. In other words, development of bubbles near the trailing edge may be more suitable than near the leading edge [93, 29, 105]. The authors surmise that a single bubble can be readily explained by well-studied induced camber theories [48, 83, 42, 94, 13, 52], but a group of several bubbles may interact with the flow quite differently [85]. Additional research is needed to investigate such detailed interactions.

By taking advantage of an efficient, coupled FSI solver, which allows for rapid exploration of thousands of wing frame configurations, a novel GA topology optimization procedure is used to improve the endurance parameter for a frame-and-membrane UAV wing. The final achieved optimum wing frame configuration results in several bubble-like deformations in addition to larger wing tip deflection normally associated with increased thin-wing flexibility. The findings reveal that frame configurations which allow for spanwise bending together with multiple bubble-like (locally) induced camber deformations offer significant improvement in the aerodynamic endurance, in addition to reduced drag at high AoA. The optimum design is verified and explained using a high-fidelity LES model. The coupled and uncoupled effects of spanwise bending and locally induced camber are studied through examination of the detailed pressure distributions and flow fields. The LES studies validate the efficient FSI solver's configuration preference, showing that although wing tip deflection alone has a minor effect on lift and drag, its occurrence is incidental to the modified frame stiffness that leads to the multiple locally-induced camber bubbles.

CHAPTER 4

A SIMPLIFIED MODEL FOR DRAG EVALUATION OF A STREAMLINED BODY WITH LEADING EDGE DAMAGE[1]

Authors – Haoliang Yu, Umberto Ciri, Arif Malik and Stefano Leonardi

The Department of Mechanical Engineering, ECW31

The University of Texas at Dallas

800 West Campbell Road

Richardson, Texas 75080-3021

[1]This paper has been submitted for review to *Journal of Turbulence*.

The goal of this chapter, therefore, is to make the first step toward development of a simple model to estimate the drag of an airfoil containing surface defects. A streamlined bump taken from the literature is adopted for the present study, and LE erosion is idealized as a series of simple forward-facing steps, of varying chordwise location and spanwise length, superposed onto the streamlined bump. It is hypothesized that a useful ROM of total drag can be derived based on superposition of the effects of the individual constituent steps that, collectively, idealize LE damage (erosion) on the streamlined body. It is further hypothesized that the ROM is bilinear mathematically, in accordance with individual linear dependencies on the chordwise location and spanwise length, respectively, of each constituent step in the aggregated LE damage representation. Discussed first in this work are the geometric modeling and basic development of the ROM for drag prediction. Following this, an "in-house" DNS code—which is applied later in the paper to assess drag predictions, explain detailed flow behaviors, and justify the form of the ROM—is itself first validated. The DNS validation is performed through comparisons with a previously published DNS study of the same streamlined bump in a turbulent channel flow. Once validated, the DNS are conducted on increasingly complex step configurations applied to the streamlined bump. The resulting flow fields are examined, and intriguing insights into the flow physics are reviewed, justifying the proposed simple bilinear mathematical form of the ROM. Subsequently, the ROM is applied to more complicated series of stepped geometries applied to the streamlined bump, the aim of which is to more closely emulate field damage of airfoils. The corresponding drag predictions are again compared to those by DNS, and limitations of the ROM are analyzed. A discussion of the key findings, and implications for applying the proposed ROM in practical applications, conclude the paper.

4.1 Geometrical modeling of leading edge erosion

Although LE erosion/damage on wind turbine blades often presents very irregular shapes, for simplification purposes, it is idealized here as a series of steps, each characterized by a chordwise location (d) and spanwise length (λ), on a streamlined bump. The height of the bump is 0.6666δ with length 6.8477δ. The apex location is at $x/\delta = 3.6835$ (Fig. 4.1, δ is the half channel height of the simulation domain seen later), further details are given in [54, 62]. Steps are modeled by shifting the original smooth bump profile downward by a constant amount ($0.0145c$, where c is the chord length of smooth bump), representative of delamination. In accordance with the chordwise location, the bump-with-step geometry adopts the shifted profile in front of the step and the original profile behind the step. A simple example with a single step at normalized location $d/c = 0.435$, and covering the entire span ($\lambda/s = 1$), is shown in Fig. 4.1(a), where s is the span length. Cases with spanwise limited steps are created by extruding the step profile for a certain length (λ) along spanwise direction, then combining this with a ($s - \lambda$) wide extrusion of the smooth profile. A specific case referred to hereinafter as 'half step' case is provided for illustration (Fig. 4.1(b)), in which the step only covers half of the span ($0 < z < 1.57$). The other half of the span ($-1.57 < z < 0$) maintains the original smooth profile. Since such geometry contains two distinct chord lengths (c and c'), a weighted average chord length ($\bar{c}$) is used in the drag coefficient calculations seen later, where $\bar{c} = c(1 - \lambda/s) + c'(\lambda/s)$.

4.2 Development of a reduced order model of drag

Considering first a single, full-span step, in developing a ROM that can estimate the drag of the bump with step, the total drag is first expressed as a sum of the drag of the baseline case (smooth bump, $C_{d,0}$) and the increment due to the single step ($\Delta C_{d,step}$):

$$C_{d,total} = C_{d,0} + \Delta C_{d,step} \tag{4.1}$$

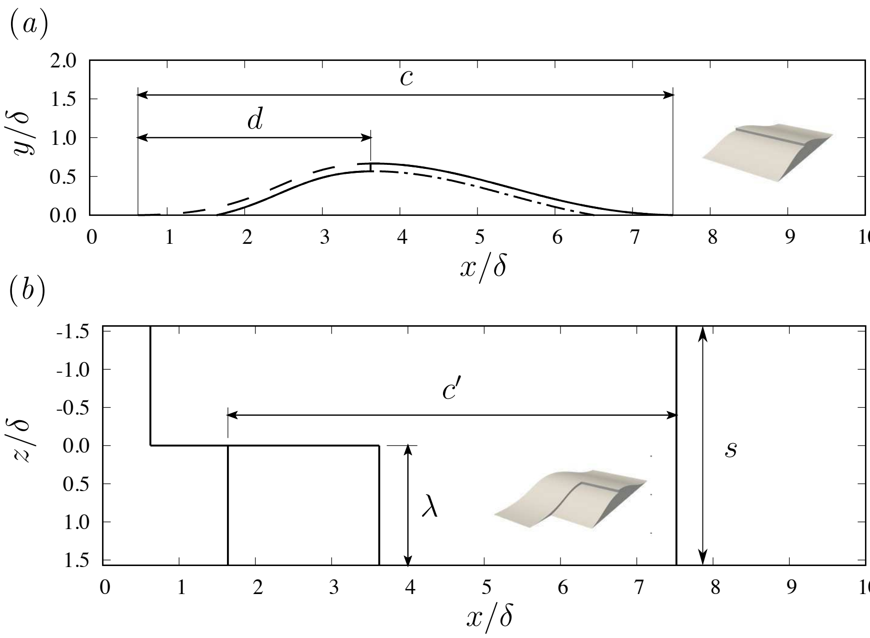

Figure 4.1. (a) Sketches of the bumps with a step at $d/c = 0.435$. Side view for the case with $\lambda/s = 1$ (——), smooth (----), and shifted (—·—). (b) Top view for the half step case ($\lambda/s = 0.5$).

This drag increment due to the step can be decomposed into the change of the dominating form drag and a small portion from the friction drag [59, 66], which is assumed negligible.

$$\Delta C_{d,step} = \Delta C_{d,form} + \Delta C_{d,viscous} \approx \Delta C_{d,form} \tag{4.2}$$

The form drag on the stepped bump from dimensional analysis is assumed to be directly proportional to the square of the local tangential velocity (U_t at the step's chordwise location), thus:

$$\Delta C_{d,step} = m_1 {U_t}^2 \tag{4.3}$$

where m_1 is a constant. Similarly, the increment of drag is also hypothesized to be proportional to the step's spanwise length (m_2 is a constant):

$$\Delta C_{d,step} = m_2(\lambda/s) \tag{4.4}$$

Combining Eq. (4.3) and Eq. (4.4), a bi-linear relation can be written as:

$$\Delta C_{d,step} = m{U_t}^2(\lambda/s) \tag{4.5}$$

where m is the combined constant. Substituting Eq. (4.5) into Eq. (4.1) gives:

$$C_{d,total} = C_{d,0} + m{U_t}^2(\lambda/s) \tag{4.6}$$

To be useful in practical applications, however, Eq. (4.6) must be expressed as a function of the geometric damage description only. Incorporating simple potential flow theory with a conformal mapping approach, the dependence of the local tangential velocity, ${U_t}^2$, on d/c is found.

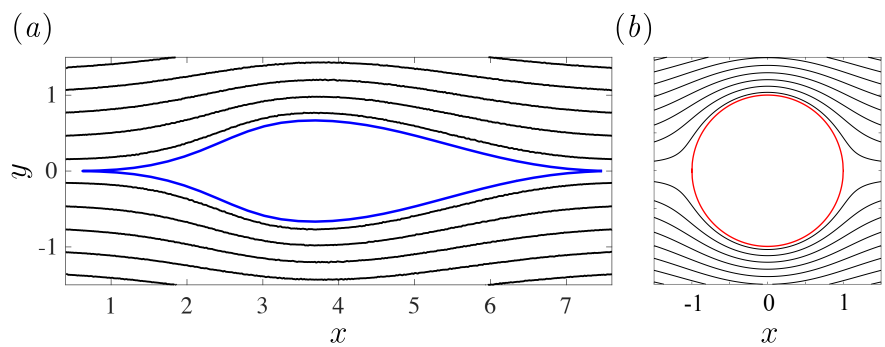

Figure 4.2. (a) Streamline visualization around the mirrored smooth bump geometry using conformal mapping. (b) Streamline visualization around the cylinder with unit radius obtained by the superposition of doublet and uniform elementary plane flow.

Consider that the smooth bump profile is mirrored (Fig. 4.2(a)) and conformably mapped onto a cylinder having unit radius (Fig. 4.2(b)) using Koebe's iterative method [70, 71]. The velocity potential (ϕ) is computed around the cylinder by the superposition of doublet and uniform elementary plane flows, and is then reversely mapped back to the domain containing the bump. Velocity components around the bump are determined by $u = -\partial\phi/\partial x$ and $v = -\partial\phi/\partial y$. The tangential velocity is $U_t = \vec{u} \cdot \hat{t} + \vec{v} \cdot \hat{t}$, in which $\hat{t}$ represents a unit vector tangent to the bump profile. As seen in Fig. 4.3, the distribution of the square of

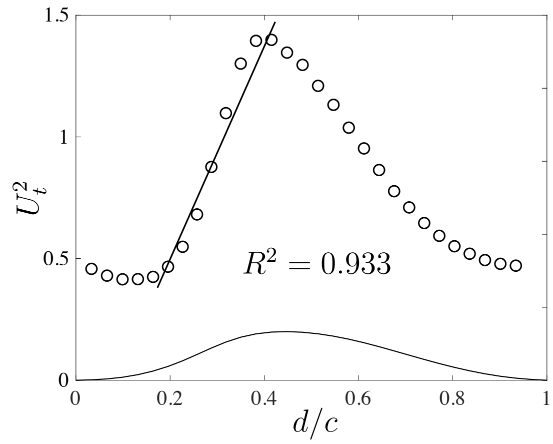

Figure 4.3. Squared tangential velocity distribution along the bump. Potential flow with conformal mapping (○) , Linear fit (——).

tangential velocity, U_t^2, on the windward side indicates a strong linear relation with respect to its chordwise location (d/c), hence Eq. (4.7), where a and b are constants:

$$U_t{}^2 = a(d/c) + b \tag{4.7}$$

Now, Eq. (4.6) can be re-written by substituting for $U_t{}^2$ from Eq. (4.7), where a' and b' are the new constants:

$$C_{d,total} = C_{d,0} + m\left[a(d/c) + b\right]\lambda/s = C_{d,0} + \left[a'(d/c) + b'\right]\lambda/s \tag{4.8}$$

4.3 Justification for the form of the reduced order model

In this section, DNS are performed using the in-house code to test the hypothesis of bilinearity in the form of the proposed ROM, in addition to identification of the coefficients in Eq. (4.8). A description of the numerical code is given in Appendix A.2. Validation of the DNS is presented first in Section 4.3.1 through comparisons with the literature. A parametric study is then carried out in Section 4.3.2 to illustrate the bilinear geometric dependence of the ROM, considering variations in the chordwise location and spanwise length of the single step. Each configuration is accompanied by the DNS, which are used to justify the underlying hypothesis of bilinearity in the ROM, as well as to examine details of the corresponding flow fields and reveal insights into the flow physics. Performance of the ROM on more complex configurations is investigated in Section 4.4.

4.3.1 Validation of numerical method used to test hypotheses in model development

The streamlined bump considered is replicated from a well-regarded study by Marquillie et al. [63]. Parameters of the DNS are reproduced, and simulations are performed for a fully developed channel flow with the smooth bump located on the lower wall. The simulation domain has size $12.56\delta \times 2.0\delta \times 3.14\delta$ (δ is the half channel height, see Fig. 4.4(a)) and grid resolution of $1537 \times 385 \times 385$. A uniform mesh is used along the streamwise (x) and spanwise (z) directions. The channel height mesh (y direction) includes a refining gradient near the lower half channel region (250 points in $0 < y/\delta < 1$ based on a constant $\Delta y = 0.004$), see Fig. 4.4(b)).

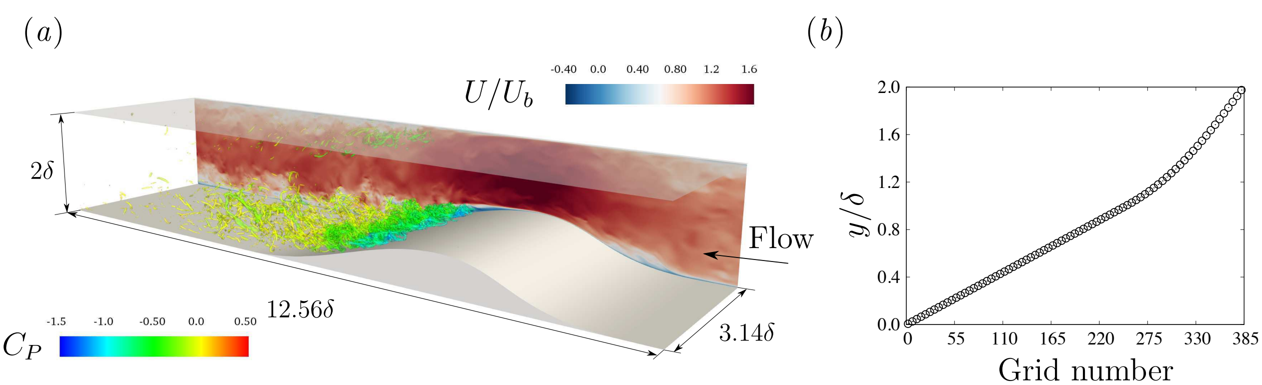

Figure 4.4. (a) Simulation setup plotted with instantaneous streamwise velocity (U) and coherent structure visualization using Q criterion [53] colored by the pressure coefficient (C_P). (b) Grid resolution along y direction. Every five grid points are plotted in symbols.

Periodic boundary conditions are imposed in spanwise directions, while the radiative boundary condition [76] is imposed at the outlet. The inlet fields are taken from a precursor simulation to generate fully developed turbulence and avoid an excessively long streamwise domain. No-slip boundary conditions are applied on both top and bottom walls.

The precursor simulation is a DNS turbulent channel flow with smooth walls, and is performed in a domain of size $6.28\delta \times 2\delta \times 3.14\delta$ with a uniformly distributed grid resolution of $513\times257\times385$. The turbulent Reynolds number is $Re_\tau = U_\tau\delta/\nu = 395$, where $U_\tau = \sqrt{\tau/\rho}$, and τ is the wall friction. Periodicity is imposed in the spanwise and streamwise directions. No slip conditions are imposed at both walls. The corresponding mean velocity profile in wall units $\overline{U}^+$ and root-mean-square (rms) velocity profiles of the precursor simulation agree well with the DNS of Moser et al. [67], as shown in Fig. 4.5 (overbars indicate averages over spanwise, streamwise, and time).

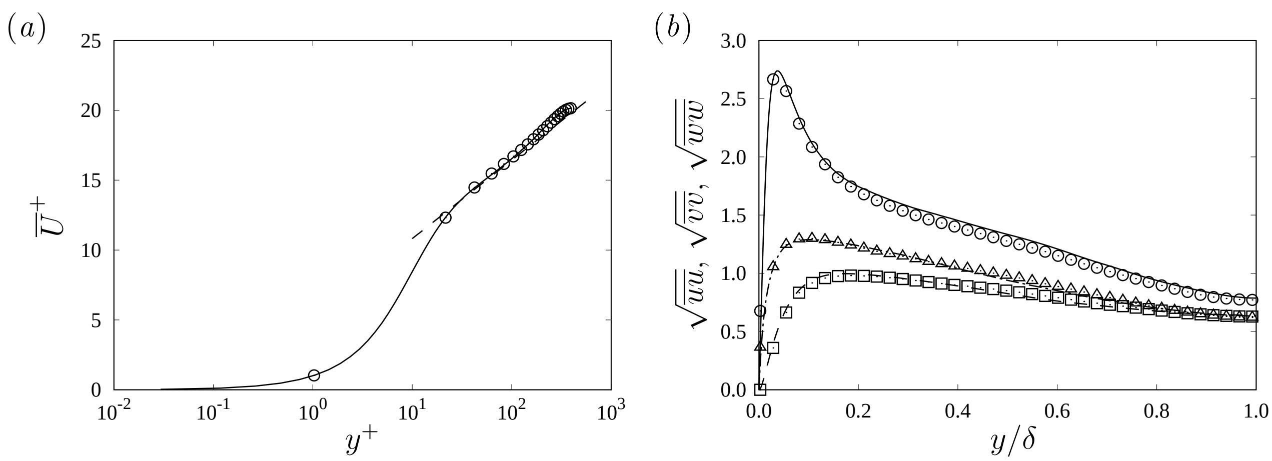

Figure 4.5. Precursor validation with Moser et al. [67] (a) The mean velocity profile in wall units, where $y^+ = U_\tau y/\nu$ and $\overline{U}^+ = \overline{U}/U_\tau$. The present data (○) are plotted using every ten grid points. Data by Moser et al. is shown as (——). The log law, $U^+ = \ln y^+/\kappa + B$, with $\kappa = 0.41$, $B = 5.2$ is plotted as (– – – –). (b) The rms velocity profiles in global coordinates. The present data are plotted in symbols using every five grid points, data by Moser et al. are plotted in lines. $\sqrt{\overline{uu}}$: (○, ——). $\sqrt{\overline{vv}}$: (□, – – – –). $\sqrt{\overline{ww}}$: (△, —·—). u, v, w represent the velocity fluctuations respect to the mean velocity.

As for the simulation with bump, the pressure coefficient is $C_P = (\overline{P} - P_0)/(\frac{1}{2}\rho U_{\max}^2)$, where P_0 is a reference pressure taken near the outlet $x/\delta = 12$ (averaged in y, z and time), and $U_{\max}$ is the maximum velocity at the inlet (averaged in z and time) on the upper flat wall as well as the lower bump surface. The bump geometry, being a streamlined body, has a pressure distribution around it that qualitatively resembles that over an airfoil. A favorable pressure gradient (FPG) region exists beginning at the LE to the apex of the bump, whereinafter an adverse pressure gradient (APG) region follows the apex to the TE (Fig. 4.6(a)). Observation of the friction coefficient, C_f $(= \tau/(\frac{1}{2}\rho U_{\max}^2)$, where τ is the shear stress at the wall), indicates that the flow separates from the lower wall (where $C_f < 0$) after the apex of bump and then reattaches at $x/\delta = 5.6$, as seen in Fig. 4.6(b). Separation is not observed on the upper wall, but C_f tends to become zero at $x/\delta \approx 6$, which indicates the flow is close to separating. In these numerical results, both C_P and C_f agree well with the DNS performed by Marquille et al.[63]. Although actual separation is only observed on the lower wall, the occurrence of coherent structures are seen near both walls in Fig. 4.4, as is also confirmed in the reference [63].

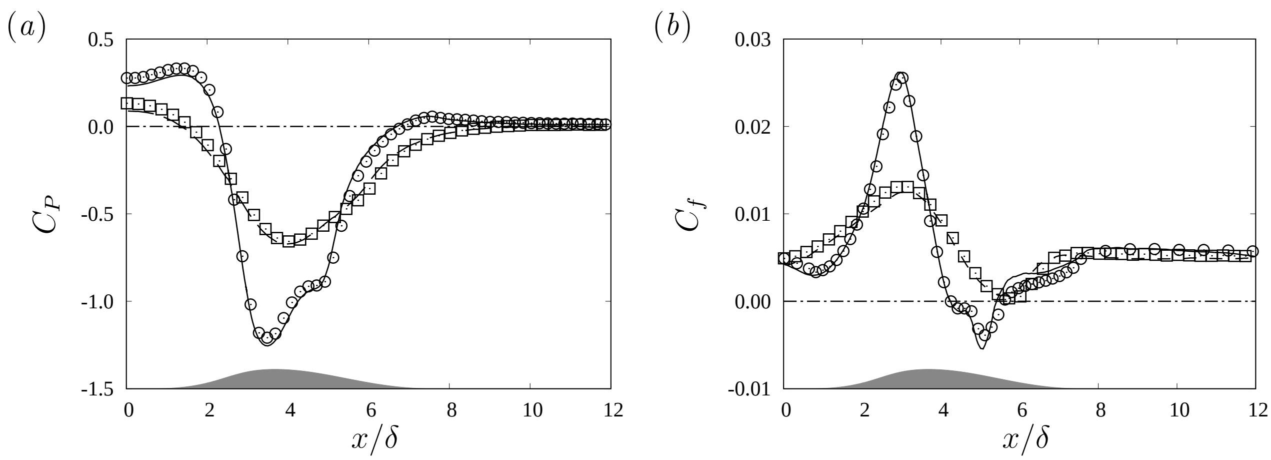

Figure 4.6. Pressure and friction coefficients comparison with Marquillie et al. (in lines) [63]. Present data are plotted in symbols using every twenty five grid points for the lower wall (○, ——) and thirty five grid points for the upper wall (□, ----). (a) Pressure coefficient computed at the two walls. (b) Skin friction coefficient computed at two walls.

The tangential velocity $\overline{U_t}$ is computed at various locations on both walls. Velocity profiles are plotted in Fig. 4.7 and compared with the DNS by Marquillie et al. [63]. A reverse flow ($\overline{U_t}/U_b^* < 0$) is observed at $x/\delta = 5.0$ on the lower wall consistent with the negative friction observed in Fig. 4.6(b). The velocity profiles from different locations on the upper wall confirm that no flow separation occurs (Fig. 4.7(b)).

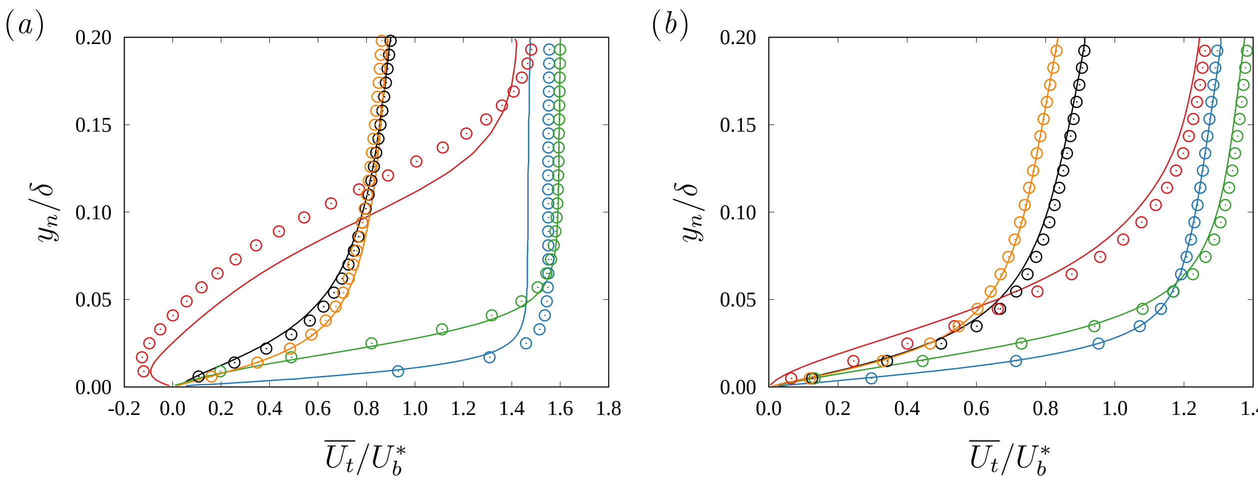

Figure 4.7. Mean tangential streamwise velocity profiles comparison with Marquillie et al. [63]. y_n is the normal distance to the wall. U_b^* is the projection of bulk velocity on the tangential direction. Symbols are the present data and lines are from Marquillie et al. $x/\delta = 0.5$: (——,○) $x/\delta = 3.0$: (——,○) $x/\delta = 11.0$: (——,○). (a) At the lower curved wall. $x/\delta = 4.0$: (——,○) $x/\delta = 5.0$: (——,○). (b) At the upper flat wall. $x/\delta = 4.5$: (——,○) $x/\delta = 5.5$: (——,○).

4.3.2 Variations in the chordwise location and spanwise length of a single step: parametric study and flow field examinations

To test the hypothesis regarding bilinear effects of chordwise location (d/c) and spanwise length (λ/s) which form the basis of the proposed ROM, a parametric DNS study is performed. Three chordwise locations of the step ($d/c = 0.232$, 0.348 and 0.435) are considered, and each is further tested with three different spanwise lengths (λ/s = 0.5, 0.7, and 1). Therefore, nine cases are simulated using the same setup described in Section 4.3.1.

The resulting drag coefficients for each configuration obtained by DNS, as well as their constituent viscous and pressure contributions, are shown in Table 4.1 (note that $C_d = 2F_\mathrm{d}/(\rho U_b^2 \overline{c} s)$, where F_d represents the corresponding drag force, and $\overline{c}$ is the spanwise averaged chord length). With respect to the smooth case, the total drag coefficient increases with

d/c as well as λ/s. The increment in drag is dominated by the contribution from form drag, which is consistent with the findings by Mollicone et al [66], and justifies the approximation in Eq. (4.2). In the smooth case, about 80% of total drag is contributed by the pressure force. For cases with a uniform step ($\lambda/s = 1$), the pressure force contribution to the total drag increases as the step approaches the mid chord, and is found to contribute 83%, 87% and 90% of the total drag for $d/c = 0.232$, 0.348 and 0.435, respectively.

Table 4.1. Total drag coefficients and its breakdown contributions of bumps with step.

Cases		$C_{d,viscous}$	$C_{d,form}$	$C_{d,total}$
d/c	λ/s			
0.232	0.5	0.0084	0.0388	0.0472
	0.7	0.0081	0.0402	0.0483
	1.0	0.0081	0.0418	0.0499
0.348	0.5	0.0086	0.0415	0.0501
	0.7	0.0083	0.0444	0.0527
	1.0	0.0073	0.0492	0.0565
0.435	0.5	0.0089	0.0458	0.0547
	0.7	0.0084	0.0502	0.0586
	1.0	0.0067	0.058	0.0647
smooth		0.0089	0.0352	0.0441

To better explain the drag force changes due to the step, the pressure and velocity distributions on the surfaces are investigated by comparing a selected case (a uniform step ($\lambda/s = 1$) placed at $d/c = 0.348$) with the baseline smooth case. Referring to Fig. 4.8(a), in terms of the pressure distribution, for the smooth case the pressure coefficient (C_p) on the windward side (blue dash line) is greater than that on the leeward side (green dash line) for the most of bump height ($0 < y/\delta < 0.59$, note in Fig. 4.8(a) the region $y/\delta < 0.3$ is not shown). The opposite circumstance occurs near the top of the bump (sub-region I, $0.59 < y/\delta < 0.67$), where the pressure on the leeward side is larger. This is due to the increased velocity and the consequent decrease of pressure. Considering now the stepped geometry, a recirculation zone in front of the step is induced along with flow separation behind its upper edge, which reattaches to the bump surface after a short distance (Fig. 4.8(b)). Between those two separated regions, a stagnation point is observed on the vertical wall of the step. Correspondingly, the pressure increases (blue solid line) and achieves a local maximum in sub-region II ($0.49 < y < 0.59$, Fig. 4.8(a)).

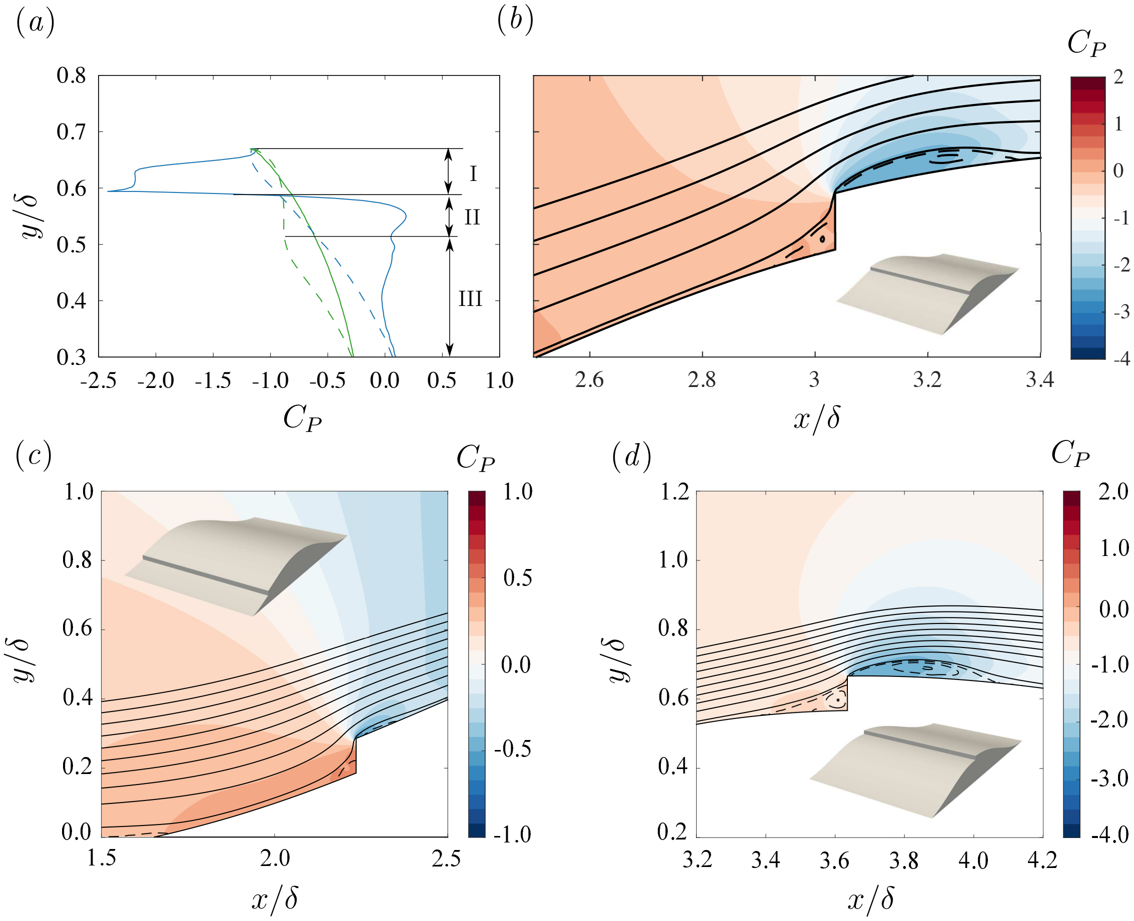

Figure 4.8. (a) Pressure coefficient along the surface of smooth bump (dashed lines) and bump with a uniform step ($\lambda/s = 1$) at $d/c = 0.348$ (solid lines). Blue: windward side, green: leeward side. (b, c, d) Streamlines (ψ, —— positive, ---- negative) superposed on the color contours of pressure coefficient. Uniform step at three chordwise positions: (b) $d/c = 0.348$, (c) $d/c = 0.232$, (d) $d/c = 0.435$. The flow field is averaged in time and spanwise direction. Note (b, c, d) are from different cases with different magnification levels for better visualization.

The area between the pressure distributions of the windward side and the leeward side is proportional to the form drag. When the pressure coefficient is greater on the windward side, the area in between provides a positive contribution to the form drag. On the contrary, where the pressure is higher on the leeward side, the pressure difference behaves as a suction force in front of the bump, and hence contributes negatively to the form drag. Overall, the form drag of the step case is about 20% higher than that of the smooth case. A portion of the increment comes from the step (sub-region II, $0.49 < y < 0.59$). Another part of it is contributed by the region more upstream of the step (sub-region III, $0.26 < y < 0.49$). This is due to the formation of a small APG region with the presence of the step; the flow decelerates locally inside this region before reaching the step. Qualitatively similar flow structures are found when the step is positioned at other chordwise locations (Fig. 4.8(*c, d*)). When the step is closer to the mid chord, however, the recirculation regions in front of and behind it are larger.

Regarding the velocity field around the bump, in both the smooth and uniform step cases, on the windward side the flow is subjected to a FPG which leads to an increase in velocity and friction coefficient (C_f) as a consequence (Fig. 4.9(*a*)). Downstream of the peak of the bump, the velocity gradually decreases, as does the friction coefficient, consistent with the APG. A separation is observed at $x/\delta \approx 5$ ($C_f < 0$) in the smooth case, and negative friction is found around $x/\delta = 3$ in the step case due to the two separated regions discussed previously. One separated region coincides with the recirculation at the bottom corner of the step, where near stagnant fluid acts as an equivalent friction-reduced 'slope' [88, 15]. Another is the separation behind the step; however, the friction achieves a peak value immediately downstream of the separation, and is even greater than that of the smooth case at the same location. This is because the separation on the crests tilts the streamlines further upward and the velocity has to increase due to the Venturi effect.

A strong shear layer is developed between the low-velocity reverse flow behind the step and the mean free stream flow. Local mixing and turbulence intensity is increased within the boundary layer, energizing it such that the boundary layer does not separate as it does

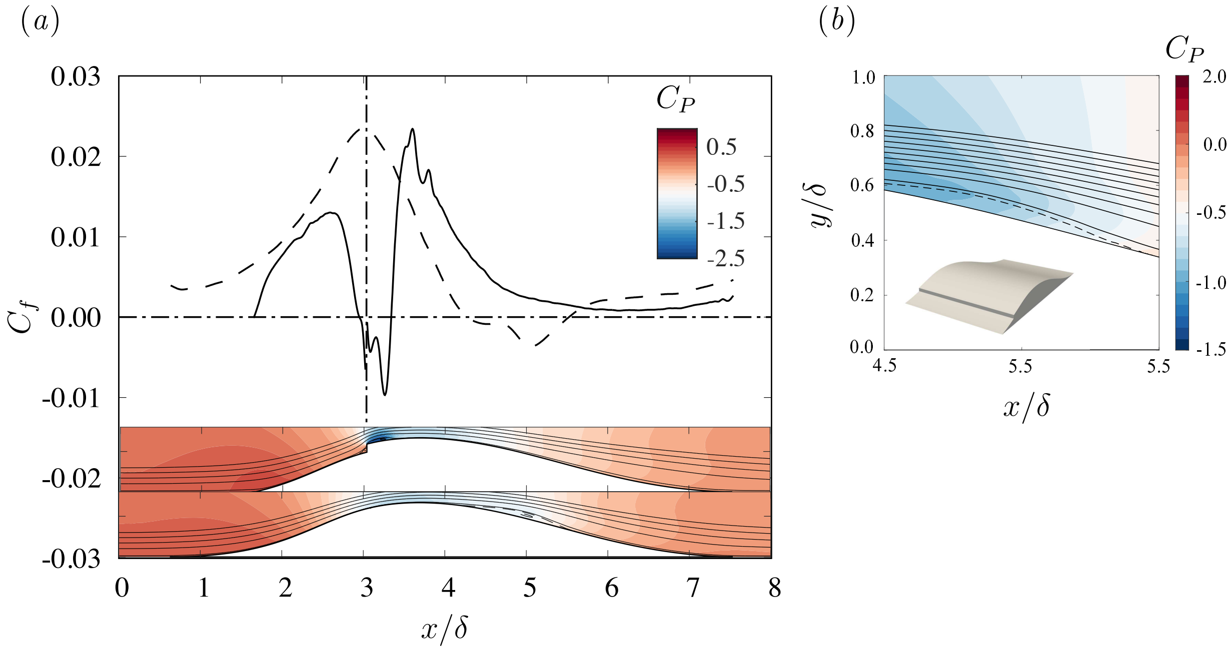

Figure 4.9. (a) Friction coefficient along the bump profile: smooth bump (– – – –), bump with step (——). Streamlines are superposed on color contours of pressure coefficient and shown in the inset to help the reader correlate the friction coefficient with the separated regions. The vertical line indicates the step location (—·—). (b) Streamlines superposed to color contours of pressure coefficient for $d/c = 0.232$.

over the smooth bump (see $x/\delta \approx 5$ in Fig. 4.9(a)); a qualitatively similar phenomenon was observed in [61]. This is not the case when the step is very close to the LE of the bump since the increase of mixing due to the upwash caused by the step is weak and not sufficient to prevent separation at the TE (see examples in Fig. 4.8(c) and Fig. 4.9(b)). Because of the reverse flow in the separated regions and the consequent negative friction, the overall viscous drag of this step case is found to be 30% less than for the smooth case. In addition, the viscous drag is observed to decrease more as the step is located closer to the mid chord, due to the growing size of the two recirculation regions.

Ultimately, the positive proportional relation between the form drag coefficient and the step location (d/c) is due to the increased velocity impinging on the step (see Fig. 4.10(a)). On the pressure side of the body, the FPG leads to an increase in velocity in the streamwise direction. When the step is placed at a farther downstream location (but in front of the apex), the flow impinges on the step with higher momentum, thus resulting in greater drag on the bump. As seen in Fig. 4.10(b), a strong linear relationship is exhibited between the increment of form drag and the tangential velocity, which is probed at one step height ($y_n/\delta = 0.1$) in front of the step. This supports the consideration underlying Eq. (4.3), proposed while developing the basic form of the ROM in Section 4.2.

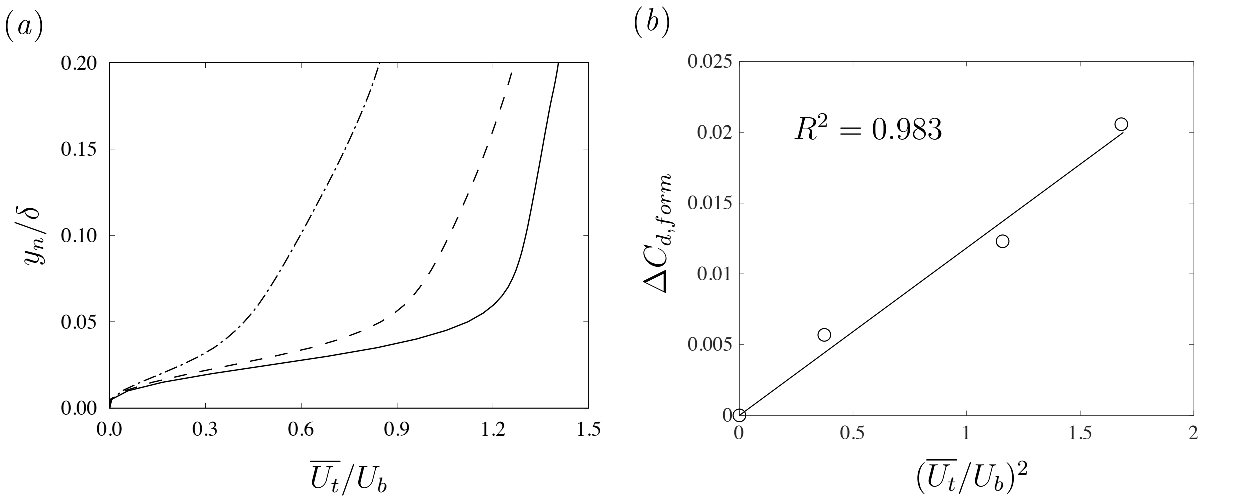

Figure 4.10. (a) Mean tangential streamwise velocity profiles in front of the step. $d/c = 0.232$: (—·—), $d/c = 0.348$: (– – – –) and $d/c = 0.435$: (——). (b) Linear relation found between $(\overline{U_t}/U_b)^2$ and $\Delta C_{d,form}$. Linear fit: (——), DNS data: (○).

For a finite step in the spanwise direction (instead of infinite/uniform step described by a single parameter d/c), numerical simulations are performed to consider the effects of step length (λ/s). As expected, drag increases with λ/s (see Table 4.1). Since the average of the pressure field cannot be assessed in spanwise direction due to the heterogeneity of the surface, a pressure force per unit length (f_{Pr}) is defined in Eq. (4.9) (Γ represents bump profile, $\vec{n}$ is the local normal direction of the profile and $\hat{x}$ is a unit vector in x direction) and used for examining the spanwise distribution of form drag for the half step case. Results are compared with the smooth case and a case with uniform step ($\lambda/s = 1$) at $d/c = 0.435$ (Fig. 4.11(a)).

$$f_{Pr} = -\int P\vec{n} \cdot \hat{x} d\Gamma \tag{4.9}$$

In both the smooth case and the case with a uniform step ($\lambda/s = 1$), due to the homogeneity of geometries a relatively constant pressure force is observed over the entire span (note that the small oscillations relate to statistical convergence). When the step covers only part of the span, however, the discontinuity in the geometry is also reflected in the pressure force distribution, which can be generally divided into two regions (smooth and step) by the change of profile at $z/\delta = 0$. The majority of the span is covered by a pressure force higher than what is found in the completely smooth case but also lower than that for the full ($\lambda/s = 1$) step case. At $z/\delta = 0$ and $z/\delta = 1.57$ (recall periodic boundary conditions are applied in the spanwise direction), corresponding to the transition between smooth and step regions, the pressure force is similar to that of the smooth bump. This is where the geometry induces streamwise vortices. In fact, as the flow approaches the bump, the step region presents less resistance due to a smaller cross section profile (lower height and reduced chord length). More flow leaning toward the step region leads to acceleration of the flow. Higher streamwise velocity is observed in front of the step region ($0 < z/\delta < 1.57$, Fig. 4.11(b)). When streams of fluid reach the step, they are tilted upward and towards the smooth region of the body because of the high pressure in proximity of the stagnation point on the step. As a consequence, two counter rotating streamwise vortices are generated at the side walls between the step and smooth regions (Fig. 4.11(c, d)).

The integral of the pressure force per unit length in Fig. 4.11(a) corresponds to the form drag discussed previously. The form drag increment of the half step case (area between dash-dot line and red line) is found to be half the increment in form drag from the smooth case to the full step case (area between dashed line and dash-dot line), indicating that the form drag change is indeed directly proportional to the spanwise step length, as proposed in Eq. (4.4). Due to the upward motion induced by the step, the wake is seen much farther behind the step region ($0 < z < 1.57$, Fig. 4.11(b)), and thus a much higher portion of the total form drag might be expected from the step region. Perhaps surprisingly, the form drag

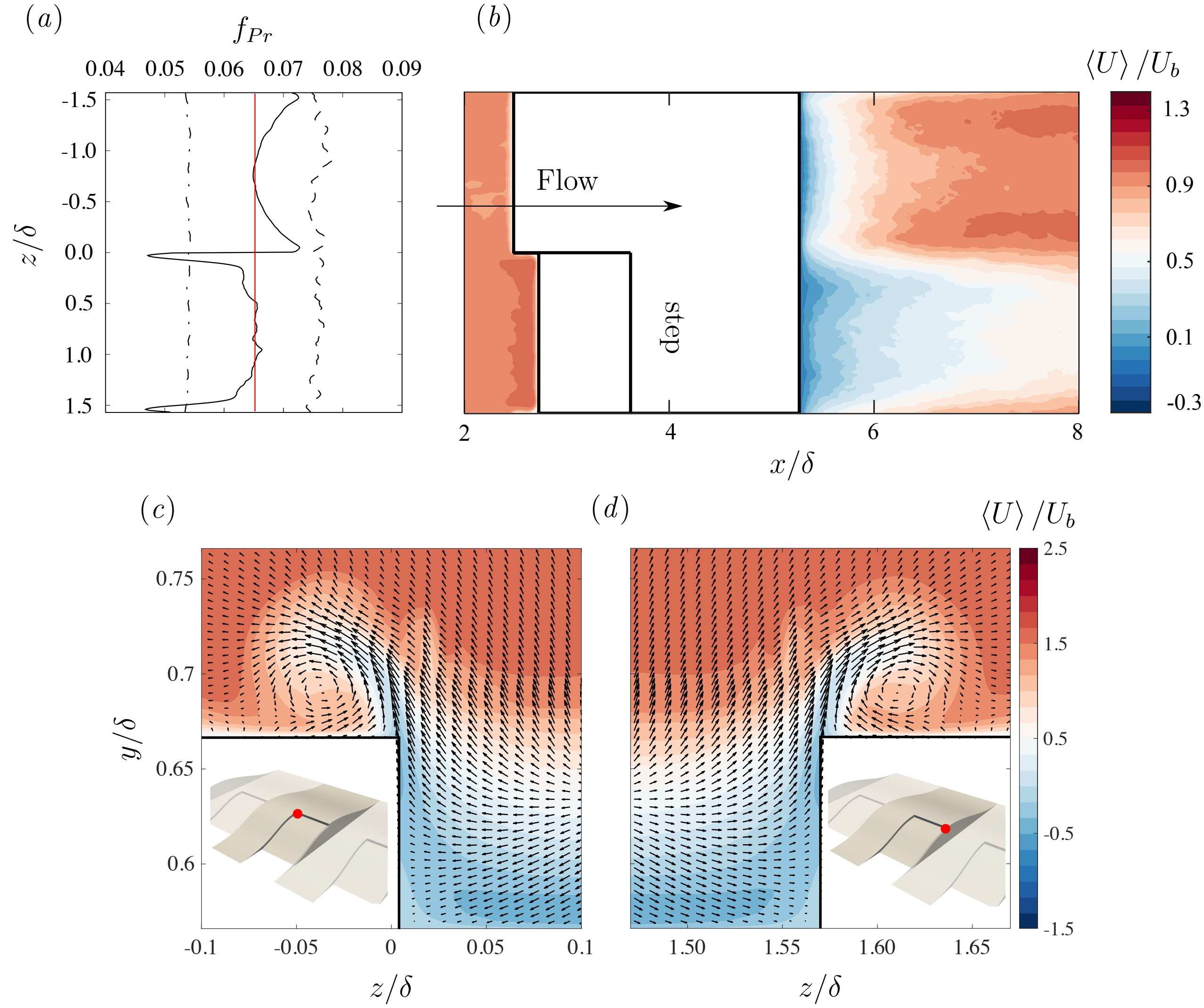

Figure 4.11. (a) Pressure force per unit span (f_{Pr}). Smooth bump: (—·—); Uniform step ($d/c = 0.435$, $\lambda/s = 1$): (- - - -) ; Half step case ($d/c = 0.435$, $\lambda/s = 0.5$): (——); Span averaged half step case: (——). (b) Color contours of time averaged streamwise velocity on a horizontal section at $y/\delta = 0.4$. (c,d) Velocity vectors superposed to color contours of time averaged velocity on a cross section in proximity of the step at $x/\delta = 3.6$. Note the horizontal axis of (d) is extended based on the periodic boundary condition along spanwise.

contribution from the step region is actually slightly less than that which is created by the smooth region—because the streamwise vortices redistribute momentum and balance the drag of each segment (smooth and step regions) of bump. This can be explained by applying the integral form of the conservation of momentum, per Eq. (4.10), to the control volume in Fig. 4.12.

$$-D = \underbrace{\int_a \rho U \cdot (-U) ds}_{\text{inflow}} + \underbrace{\int_b \rho U \cdot (W) ds}_{\text{side wall flux}} + \underbrace{\int_c \rho U \cdot (U) ds}_{\text{wake}} + \underbrace{\int_d \rho U \cdot (-W) ds}_{\text{side wall flux}} \tag{4.10}$$

where D is the force of the flow over the portion of the bump in the control volume, U and W are the streamwise and spanwise scalar components of the velocity, respectively. For a uniform step, the two integrals accounting for side wall fluxes are zero, and the drag is simply the difference between the momentum at the inlet and outlet of the control volume. However, a less than full spanwise step induces counter rotating streamwise vortices, or in simpler terms, streams of fluid move from the step region to the smooth region. In such circumstance, the two side wall flux terms are no longer zero. Since the vortices are counter rotating, W has opposite signs on faces (b) and (c), but it is always the same as the normal direction (outward the control volume is positive with the notation in Eq. (4.10)). These fluxes tend to reduce the drag of the step region. On the other hand, considering an equivalent control volume for the smooth region, all terms remain the same as Eq. (4.10) but the normal to the side walls changes sign. Therefore, both integrals become negative and tend to increase the drag of the smooth portion of the bump. This explains the similar value of the pressure force per unit length on the step and smooth region of the bump and the larger wake behind the step region observed in Fig. 4.11.

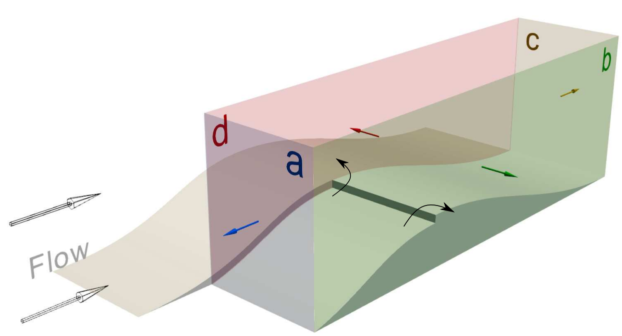

Figure 4.12. Control volume schematic for the half step case.

The remaining aspect of the ROM hypothesis to be tested is the linear relationship found between the local tangential velocity and step's chordwise location, as suggested in Eq. (4.7). Although this relation is indicated by the potential flow approach using conformal mapping, a higher-fidelity numerical simulation is still needed to confirm the relation due to the inherent simplifying assumptions of potential flow theory. By applying the described DNS to the smooth bump geometry, support for the hypothesis is indeed attained as follows. By 'probing' the tangential velocity in the region ahead of the apex of the bump at a constant height $y_n/\delta = 0.2$ (where Fig. 4.13(a) shows the tangential velocity gradients in the normal direction to be relatively small), the square of the DNS tangential velocity is found to exhibit a linear relation with chordwise location, consistently with potential flow theory as shown in Fig. 4.13(b). The existence of minor differences between the DNS and potential flow results is due to the fundamentally different flow characteristics of the two approaches (i.e., inlet conditions, domain dimension in y, boundary layers, etc.). At this point, absent one remaining hypothesis, which accounts for multiple steps, the basic mathematical form of the proposed ROM has been justified by observations from the foregoing DNS studies. Moreover, fitting of the coefficients in Eq. (4.8) using data from Table 4.1 leads to satisfactory ROM performance for single steps, as shown in Fig. 4.13(c), where $a' = 0.0722$ and $b' = -0.01154$. Note that Fig. 4.13(c) clearly illustrates the bilinear dependence of the total drag on chordwise location and spanwise length with a single step. The next section addresses the remaining hypothesis related to proposing a 'useful' ROM; that superposition of several, geometrically distinct constituent steps is appropriate to idealize more complex LE damage on a streamlined body.

4.4 Application of reduced order model to more complex geometries

In this section, the proposed ROM in Eq. (4.8) is extended to more geometrically complex cases to explore its capabilities and limitations when more closely emulating LE damage.

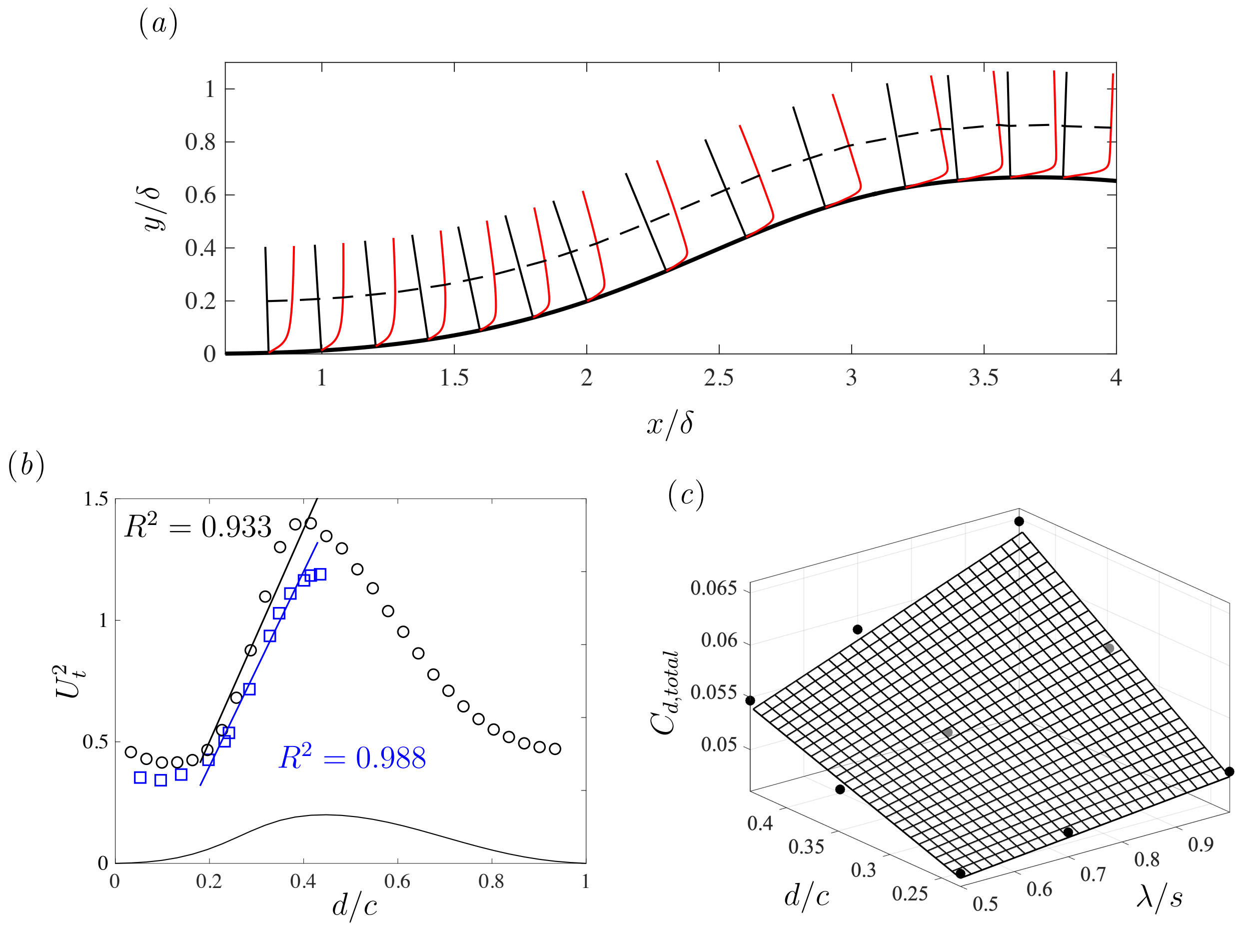

Figure 4.13. (a) DNS tangential velocity profiles at different chord locations (only the front half part of the bump). Tangential velocity profiles: (——), 'Probing' locations: (- - - -) (b) Squared tangential velocity distribution along the bump. Potential flow with conformal mapping: (○), present DNS: (□), Linear fit: (——), (——). (c) Total drag coefficient versus the step's chordwise location and spanwise length. DNS data points: (●). The meshed surface represents the proposed ROM.

Four new geometries are introduced and DNS are performed as reference to assess the performances of the ROM, as shown in Table 4.2. The first three cases (1-3) have more than one step, each of which is evenly distributed along the span (and each step has the same spanwise length). Case 3 includes two steps at two different chordwise locations. The entire span of Case 4 is covered by a 'single' step having random zig-zag face pattern rather than a flat-faced step. Total drag coefficients are computed as described below using the ROM (based on the coefficients obtained earlier) and compared with the DNS results. Note that Cases 1 and 2 are designed with the intent to understand the influence on drag due to the spanwise length of each of the individual steps. In both cases, half of the total span is covered by steps (i.e., $\lambda/s = 0.5$), hence, $\bar{c}$ is the same for Cases 1 and 2. In addition, all steps in these cases share the same chordwise location ($d/c = 0.435$). Therefore, from the viewpoint of the proposed ROM, these two cases have identical geometrical input parameters (d/c and λ/s), which also happen to be the same as the half step case seen earlier in Section 4.3.2. Referring to the results in Table 4.2, relative to DNS, the ROM under predicts the drag coefficient for Case 1 (-2.17% error), but overpredicts it for Case 2 (+3.63% error). Through comparison of the drag components of Cases 1 and 2 with the earlier half step case, the increased error stems from the decreased form drag but increased friction, since the single half step is now divided into multiple narrower steps (for the earlier half step case: $C_{d,total} = 0.0547$, $C_{d,form} = 0.0458$, $C_{d,viscous} = 0.0089$, +1.30% error).

Table 4.2. Drag component analysis for more complex geometries using DNS, and corresponding total drag estimation with reduced order model (ROM)

Case No.	1	2	3	4
Geometry	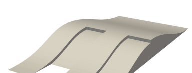	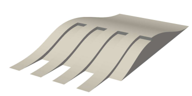	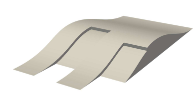	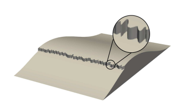
Description	2 steps $\lambda/s = 0.5$ $d/c = 0.435$	4 steps $\lambda/s = 0.5$ $d/c = 0.435$	2 steps $\lambda/s = 0.25,\ 0.25$ $d/c = 0.435,\ 0.348$	zigzag $\lambda/s = 1$ $d/c = 0.348$
$C_{d,total}$	0.0553	0.0522	0.0530	0.0613
$C_{d,form}$	0.0413	0.0378	0.0375	0.0492
$C_{d,viscous}$	0.0140	0.0144	0.0155	0.0121
ROM $C_{d,total}$	0.0541	0.0541	0.0526	0.0578
ROM Error	-2.17%	+3.63%	-0.75%	-5.71%

It is worth recalling that the proposed ROM is formed on the observation that friction only contributes a small portion of the total drag, and as a consequence, that variations in friction across different cases are negligible. The respective contributions of friction are found to be 16% for the half step case, 25% for Case 1, and a relatively greater 28% for Case 2. These results arise because larger number of steps implies increased number of vertical side walls oriented along the streamwise direction, which lead to increased viscous forces that are not accounted for in the ROM.

Regarding the decreased form drag for Cases 1 and 2 (relative to the half step), this is caused by the narrower steps. On the one hand, stronger recirculation is observed in front of the step when the single step's spanwise length is shorter, see Fig. 4.14 together with Fig. 4.8(d). The resultant lower pressure on the step reduces the form drag. Note also that a longer separation distance behind a single step is seen for relatively longer (spanwise) steps (e.g., Fig. 4.14(a)). This indicates that a narrow step benefits the turbulence mixing, which brings high velocity free stream flow to overcome the momentum deficit created by the separation behind the step and promotes reattachment. On the other hand, as the flow collides with the step and tries to escape, it not only does so along the streamwise direction but also in the spanwise direction by ascending the side walls. Indeed, as shown in Fig. 4.15, vortices are formed on the edge of the smooth region in each case. However, circulations are also found inside the channels of Case 2, as shown in Fig. 4.15(d), which actually shorten the 'effective' spanwise lengths of its steps, and hence reduce the form drag. A three dimensional pathline visualization is also provided for a more straightforward view in Fig. 4.16.

As net outcome for Case 1, the increased friction is mostly canceled by the decreased form drag, so the ROM estimation of the total drag coefficient still achieves reasonably good agreement with the DNS data. Since the reduction in form drag is even larger for Case 2, the increased friction is still insufficient to compensate; thus the ROM estimation for Case 2 gives a larger error relative to DNS.

Case 3 in Table 4.2 demonstrates the ability of the proposed ROM in providing reasonable drag estimations even when multiple steps are present at different chordwise locations. Based

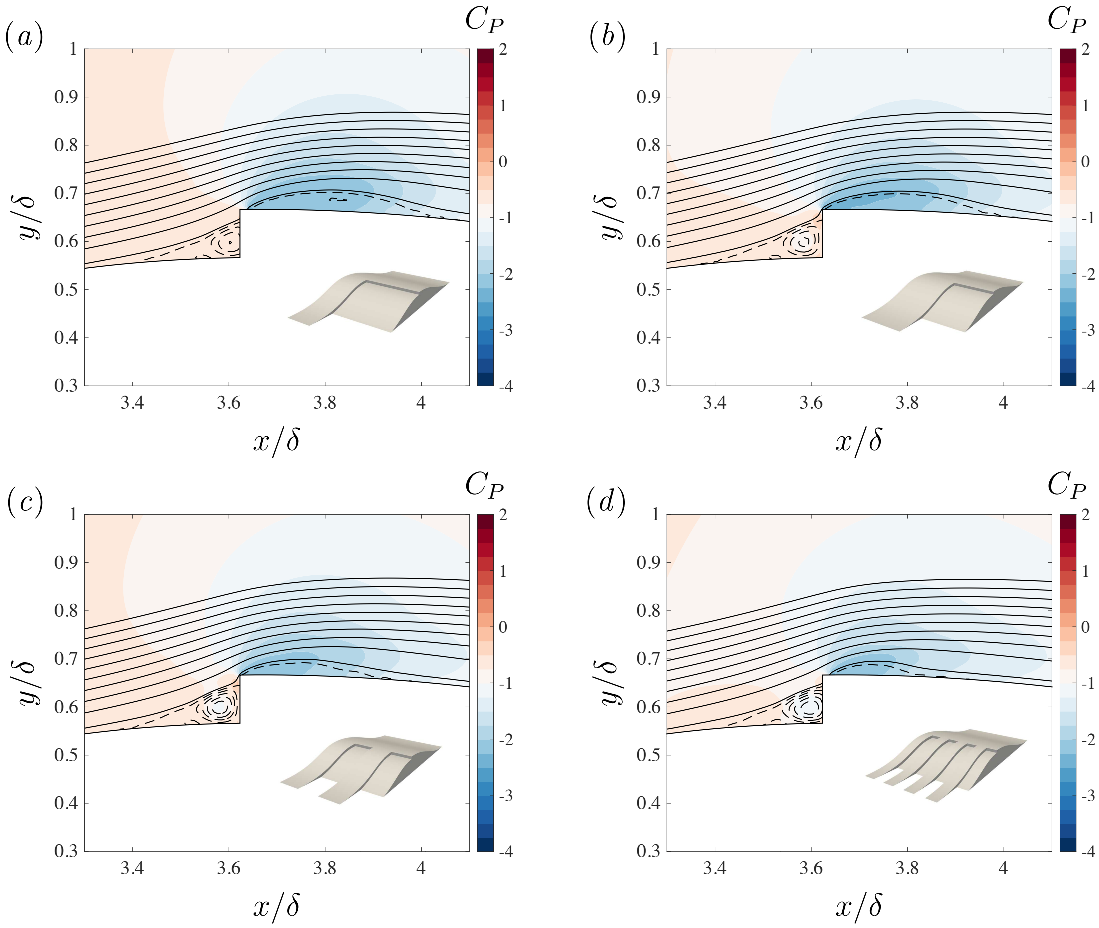

Figure 4.14. Streamlines visualization superposed on the pressure coefficient contour. Positive ψ (——), negative ψ (- - - -). The flow field is averaged within the step region in spanwise and time. (a) Case with $d/c = 0.435$ and $\lambda/s = 0.7$. (b) The half step case. (c) Case 1. (d) Case 2.

on the previous understanding, the three dimensionality can modify the spanwise pressure force distribution (see Fig. 4.11(a) for the half step case) but does not change the overall amount, which is only proportional to the step's chordwise location and spanwise length. In addition, the spanwise length of each individual step in Case 3 is similar those in Case 1 (and not as narrow as Case 2), so relative to a half step, the extra friction from the side walls is similarly expected to be compensated by decreased form drag. Due to the different chordwise step locations in Case 3, in accordance with the superposition hypothesis, the ROM is extended as Eq. (4.11), where d_1/c and d_2/c define the corresponding chordwise

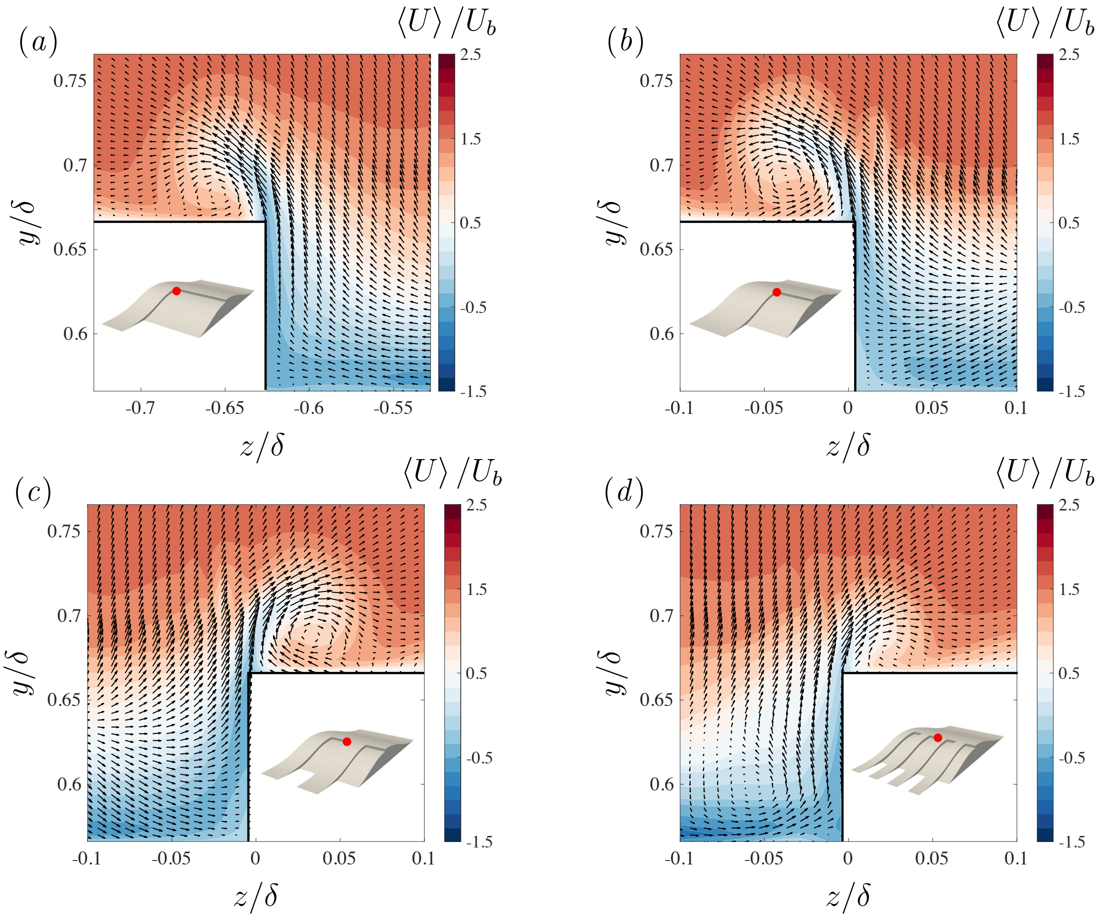

Figure 4.15. Time averaged secondary flow visualization superposed on the streamwise velocity contour at $x/\delta = 3.6$. (a) Case with $d/c = 0.435$ and $\lambda/s = 0.7$. (b) The half step case. (c) Case 1. (d) Case 2.

locations of the two steps. Or, in the more general expression of Eq. (4.12), the total drag increment is obtained as the sum contribution of n steps, where each step's chordwise location is defined by d_i/c, and where the spanwise length is specified as λ_i/s.

$$C_{d,total} = C_{d,0} + \left[a'(\frac{d_1}{c}) + b'\right](\lambda/s) + \left[a'(\frac{d_2}{c}) + b'\right](\lambda/s) \tag{4.11}$$

$$C_{d,total} = C_{d,0} + \sum_{i=1}^{n} \left[a'(d_i/c) + b'\right](\lambda_i/s) \tag{4.12}$$

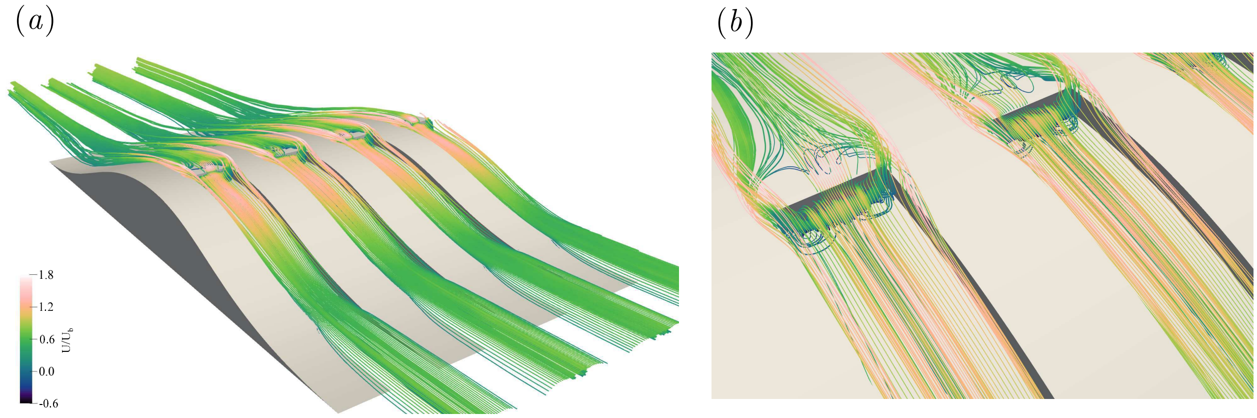

Figure 4.16. Pathline visualization for case 2. (*a*) Perspective view of the entire bump. (*b*) Zoomed in view near the step. Pathline is colored by streamwise velocity.

Ultimately, since the inspiration of the present work comes from erosion on the LE of wind turbine blades, Case 4 in Table 4.2 is specifically designed to mimic the realistic shape of such damage, while allowing an investigation of its drag behavior compared to the flat step case seen in Table 4.1. As seen in Table 4.2, the ROM unsurprisingly reveals greatest error against DNS among all the cases examined. Nonetheless, the 5.71% underprediction is commendable given the model's simplicity and its rapid prediction based on only the geometric characteristics. Interestingly, by looking into the DNS drag components, it is seen that the form drag of Case 4 is actually about the same as the DNS form drag of the flat step case (0.0492). Therefore, the resulting poorer estimation of the ROM total drag coefficient stems solely from the friction contribution. Again, compared to the flat step case (with $C_{d,viscous} = 0.0073$), extra friction is generated on Case 4's zig-zag 'step' surface, which leads to lower performance by the proposed ROM. Notably, this result also reveals that the detailed shape of the step has negligible effect on the form drag while considerably impacting friction. From the aspect of ROM development, therefore, the result also substantiates the assumption form drag dominates over the friction drag, and that more importantly, the decision to emulate LE damage as flat, forward-facing steps is justified. Even though a few DNS are required to determine $C_{d,0}$ and coefficients a' and b' in Eq. (4.12) for a given streamlined body, once these are known the ROM can be applied to provide important insights into total drag changes on the body due to widely varying configurations of leading-edge damage.

4.5 Chapter Conclusion

A reduced order model is proposed and developed to provide rapid estimation of the change in total drag coefficient for a streamlined body when leading-edge surface defects exist. While applicability of the reduced order model is general, its motivation stems from damage experienced by wind turbine blades due to leading edge erosion, which frequently manifests as surface fracture and loss of the laminated sections of the airfoils. To ensure the reduced model is useful, it is developed to be a function of only the geometric characteristics of leading edge damage, including chordwise locations and spanwise lengths of individual forward-facing 'steps' that emulate localized damage patterns. Hypotheses associated with the reduced order model development, for which support is demonstrated and explained through detailed direct numerical simulation studies, are that: 1) the reduced model of total drag can superpose the effects of the individual steps that collectively idealize the leading-edge damage, and that 2) the reduced model has bilinear dependency on the chordwise locations and spanwise lengths of the stepped damage features. Despite these assumptions of superposition and bi-linearity that form the basis of the reduced model, it still performs reasonably well relative to direct numerical simulation, even for the more complex geometries investigated. DNS results confirm that the pressure drag is the dominant component of total drag in all cases evaluated. When step lengths are restricted to less than full span, it is found that the resulting three-dimensionality of the frontal profile has a rather limited impact on total drag, even though it alters the force distribution significantly across the span. Moreover, when steps are very narrow in spanwise direction, the form drag is found to decrease substantially due to the strong recirculation formed in front of the steps, which reduces the 'effective' chordwise lengths of the narrow steps, lowering the drag impact. Analogous to using riblets (turbulators) with specifically designed dimensions and patterns to reduce drag on surfaces, such behavior possibly reveals a preferable damage mode from an engineering design aspect; if wind turbine blades, for example, are partially and intermittently reinforced along the span during manufacture, then as damage due to erosion occurs, relatively wide areas of connected erosion can be 'engineered' to only manifest as intermittent sections of narrow delamination (narrow longitudinal grooves) on the airfoil leading edges, thereby benefitting from reduced increments in total drag effects, as is demonstrated by the findings in this work.

CHAPTER 5

CONCLUSION AND FUTURE WORK

Presented has been understanding and improving the aerodynamic performance of airfoils in UAV and wind energy applications using numerical approaches of varying efficiency and fidelity.

In the UAV flexible wing study, a novel topology optimization using genetic algorithm with an efficient FSI model is presented, which produces a wing frame configuration with optimal flexibility distribution associated with high aerodynamic performance. Higher fidelity simulation - LES is applied and verified the improvement achieved. The hypothesis proposed remains supported. The decoupled effects of the induced camber and span-wise bending deformation are analyzed to understand their contributions to performance improvements.

As for the research about wind turbine blades with LE erosion, a bilinear ROM is developed for efficient drag prediction with satisfactory accuracy. The rationality of the ROM is verified by DNS. The hypotheses proposed have been tested and remain supported. Insights into the flow physics influencing both form and friction contributions to total drag are presented, a preferable damage mode from an engineering design aspect is revealed.

Future work will focus on extending the proposed ROM to real airfoil shapes at higher Reynolds number where the friction contribution is expected to be even less, thus potentially aiding accuracy and usefulness of the ROM further. Besides, the impact on the model development due to the consideration of laminar-turbulent transition should be studied. An additional erosion-related geometric parameter, step height, can also be incorporated to extend the ROM applicability and realize potentially even greater engineering benefit.

APPENDIX

NUMERICAL APPROACHES

Multiple numerical models have been applied for the present research above, though various improvements are made for those models by the author, the model development is not considered as the main contribution of this dissertation. However, to make the dissertation more self-contained, each model is documented with reasonable details in this appendix.

A.1 Fluid-structure interaction methodology

A.1.1 Finite element structural model

Finite element approach is used to simulate the deformation of complex wing structure of flexible micro air vehicle under aerodynamic load. Shear-deformable frame elements and shell elements are used, the shared six degrees of freedom per node allow for automated assembly during creation of a wing surface and simplified solid structural simulation of using only planar elements oriented in three-dimensional space. It is a reasonable simplification considering the micro air vehicle wings are often thin structures. Besides, this formulation significantly reduces computational complexity and cost compared with conventional isoparametric solid elements, which require a very resolute discretization for thin sections in order to reach the same level of accuracy (due to aspect ratio effects).

The standard finite element method consists of the terms K_g corresponding to the global stiffness matrix, U_g corresponding to the global nodal deformation vector, and F_g corresponding to the global nodal force vector as shown in Eq. (A.1) below:

$$[K_g]\{U_g\} = \{F_g\} \tag{A.1}$$

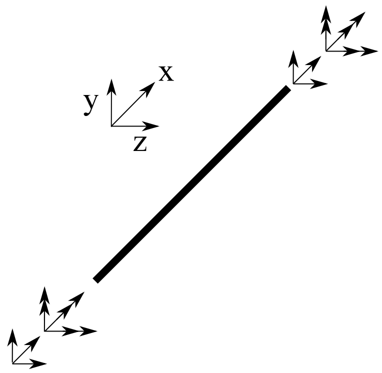

Figure A.1. Frame element degrees of freedom (single arrows depict the translational DOFs; double arrows depict the rotational DOFs).

Frame element

A shear deformable three-dimensional frame element [30] is used to model the wing frame. This element has combined formulations of beam and truss element with shear deformation considerations. For frame element, i, in a global system of n frame elements, the element stiffness matrix $[k_{e,f}]$ is first formulated in local coordinate system (subscript "e", "f" indicates "frame") and then transformed to the global coordinate system using the frame element transformation matrix $[T_f]_i$, where it will then be summed together with stiffness contributions from other frame and shell elements to create the global stiffness matrix given below:

$$[k_{g,f}]_i = [T_f]_i^{\mathrm{T}} \, [k_{e,f}]_i \, [T_f]_i \tag{A.2}$$

This 12 degree of freedom (DOF) element shown in Fig. A.1 contains six degrees of freedom at each of the two nodes, corresponding to three translations and three rotations. The element stiffness matrix depends on the following structural properties: cross sectional area A, elastic modulus E, element length L, moments of inertia of the cross section I_y and I_z, shear modulus G, torsional factor K (equal to the cross sectional polar moment of inertia for circular cross sections), and shear deformation factors k_y and k_z.

The frame element DOF is denoted below:

$$\{U_{e,f}\} = \{u_1, v_1, w_1, \theta_{x1}, \theta_{y1}, \theta_{z1}, u_2, v_2, w_2, \theta_{x2}, \theta_{y2}, \theta_{z2}\}^{\mathrm{T}} \tag{A.3}$$

where u, v, and w signify translations in the x, y, and z axes respectively and θ denotes a rotational degree of freedom around a specified axis.

The frame element stiffness matrix in local coordinates is a symmetric 12 by 12 matrix given below:

$$[k_{e,f}] = \begin{bmatrix} \mathrm{X} & 0 & 0 & 0 & 0 & 0 & -\mathrm{X} & 0 & 0 & 0 & 0 & 0 \\ \vdots & \mathrm{Y}_1 & 0 & 0 & 0 & \mathrm{Y}_2 & 0 & -\mathrm{Y}_1 & 0 & 0 & 0 & \mathrm{Y}_2 \\ \vdots & \vdots & \mathrm{Z}_1 & 0 & -\mathrm{Z}_2 & 0 & 0 & 0 & -\mathrm{Z}_1 & 0 & -\mathrm{Z}_2 & 0 \\ \vdots & \vdots & \vdots & \mathrm{S} & 0 & 0 & 0 & 0 & 0 & -\mathrm{S} & 0 & 0 \\ \vdots & \vdots & \vdots & \vdots & \mathrm{Z}_3 & 0 & 0 & 0 & \mathrm{Z}_2 & 0 & \mathrm{Z}_4 & 0 \\ \vdots & \vdots & \vdots & \vdots & \vdots & \mathrm{Y}_3 & 0 & -\mathrm{Y}_2 & 0 & 0 & 0 & \mathrm{Y}_4 \\ \vdots & \vdots & \vdots & \vdots & \vdots & \vdots & \mathrm{X} & 0 & 0 & 0 & 0 & 0 \\ \vdots & \vdots & \vdots & \vdots & \vdots & \vdots & \vdots & \mathrm{Y}_1 & 0 & 0 & 0 & -\mathrm{Y}_2 \\ \vdots & \vdots & \vdots & \text{symm.} & \vdots & \vdots & \vdots & \vdots & \mathrm{Z}_1 & 0 & \mathrm{Z}_2 & 0 \\ \vdots & \vdots & \vdots & \vdots & \vdots & \vdots & \vdots & \vdots & \vdots & \mathrm{S} & 0 & 0 \\ \vdots & \vdots & \vdots & \vdots & \vdots & \vdots & \vdots & \vdots & \vdots & \vdots & \mathrm{Z}_3 & 0 \\ \vdots & \vdots & \vdots & \vdots & \vdots & \vdots & \vdots & \vdots & \vdots & \vdots & \vdots & \mathrm{Y}_3 \end{bmatrix} \tag{A.4}$$

where the terms in the above matrix are defined:

$$\mathrm{X} = \frac{AE}{L} \tag{A.5}$$

$$\mathrm{Y}_1 = \frac{12EI_z}{(1+\phi_y)\,L^3} \tag{A.6}$$

$$\mathrm{Y_2} = \frac{6\mathrm{EI_z}}{(1+\phi_\mathrm{y})\,\mathrm{L}^2} \tag{A.7}$$

$$\mathrm{Y_3} = \frac{(4+\phi_y)\,EI_z}{(1+\phi_y)\,L} \tag{A.8}$$

$$\mathrm{Y_4} = \frac{(2-\phi_y)\,EI_z}{(1+\phi_y)\,L} \tag{A.9}$$

$$\mathrm{Z_1} = \frac{12EI_y}{(1+\phi_z)\,L^3} \tag{A.10}$$

$$\mathrm{Z_2} = \frac{6EI_y}{(1+\phi_z)\,L^2} \tag{A.11}$$

$$\mathrm{Z_3} = \frac{(4+\phi_z)\,EI_y}{(1+\phi_z)\,L} \tag{A.12}$$

$$\mathrm{Z_4} = \frac{(2-\phi_z)\,EI_y}{(1+\phi_z)\,L} \tag{A.13}$$

$$\mathrm{S} = \frac{GK}{L} \tag{A.14}$$

$$\phi_y = \frac{12EI_zk_y}{AGL^2} \tag{A.15}$$

$$\phi_\mathrm{z} = \frac{12EI_yk_z}{AGL^2} \tag{A.16}$$

This stiffness matrix is then transformed to the global system by means of a 12 by 12 transformation matrix given below:

$$T_{f(12\times 12)} = \begin{bmatrix} [\lambda] & [0] & [0] & [0] \\ [0] & [\lambda] & [0] & [0] \\ [0] & [0] & [\lambda] & [0] \\ [0] & [0] & [0] & [\lambda] \end{bmatrix} \tag{A.17}$$

where

$$[\lambda] = \begin{bmatrix} \cos\theta_{e1,g1} & \cos\theta_{e1,g2} & \cos\theta_{e1,g3} \\ \cos\theta_{e2,g1} & \cos\theta_{e2,g2} & \cos\theta_{e2,g3} \\ \cos\theta_{e3,g1} & \cos\theta_{e3,g2} & \cos\theta_{e3,g3} \end{bmatrix} \tag{A.18}$$

and

$$[0] = \begin{bmatrix} 0 & 0 & 0 \\ 0 & 0 & 0 \\ 0 & 0 & 0 \end{bmatrix} \tag{A.19}$$

The cosine terms correspond to direction cosines between the axes of the element "e" coordinate system and those of the global "g" coordinate system.

Shell element

The triangular shell element formulation used in this analysis is based on the combination of a membrane element formulation by Felippa [36] and a plate bending element formulation by Batoz [9]. The membrane element has three DOFs at each node, two in-plane translational degrees of freedom and one rotational degree of freedom with an axis of rotation normal to the element surface. The plate bending element has, at each node, one out-of-plane translational degree of freedom and two rotational degrees of freedom with axes parallel to the triangle surface. The formulation of this element assumes a decoupling of the bending and membrane actions much like the combination of the truss and beam elements for the frame element formulation. The standard local coordinate system for the shell element is

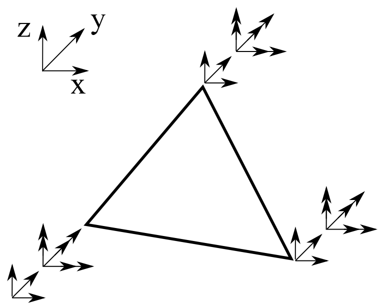

Figure A.2. Shell Element Degrees of Freedom (18 total; 6 at each node) and local coordinate system definition; (single arrows depict the translational DOFs; double arrows depict the rotational DOFs).

shown in Fig. A.2 with the local x axis along the edge of the triangle between the first and second nodes, the local y axis perpendicular to the x axis and parallel to the plane of the triangle surface, and the local z axis oriented normal to the plane defined by the triangle using the "right hand rule" convention according to node numbering.

The formulation of the OPT triangular membrane element can be found in [57, 36]. The stiffness formulation involves the triangle coordinates, the thickness, h, the material Poisson ratio, ν, and the elastic modulus, E_0. The nine degrees of freedom are denoted according to their corresponding coordinate axis of application as shown in Eq. (A.20) below where u and v signify translations in the element x and y axes respectively and θ denotes the rotational degree of freedom around the out-of-plane axis.

$$\{U_{e,m}\} = \{u_1, v_1, \theta_{z1}, u_2, v_2, \theta_{z2}, u_3, v_3, \theta_{z3}\}^{\mathrm{T}} \tag{A.20}$$

The membrane contribution to stiffness involves an assembly of a number of intermediate terms into a 9 by 9 stiffness matrix, K_m :

$$K_m = \frac{1}{V} L E L^{\mathrm{T}} + \frac{3}{4}\beta_0 \widetilde{T}_{\theta u}^{\mathrm{T}} \mathrm{K}_\theta \widetilde{T}_{\theta u} \tag{A.21}$$

where V is the triangle volume (product of area and thickness), and the remaining terms are:

$$E=\frac{E_0}{1-v^2}\begin{bmatrix}1 & v & 0\\ v & 1 & 0\\ 0 & 0 & \frac{1-v}{2}\end{bmatrix} \tag{A.22}$$

$$L=\frac{h}{2}\begin{bmatrix}\mathrm{y}_{23} & 0 & \mathrm{x}_{32}\\ 0 & \mathrm{x}_{32} & \mathrm{y}_{23}\\ \frac{1}{6}\alpha_{\mathrm{b}}\mathrm{y}_{23}\left(\mathrm{y}_{13}-\mathrm{y}_{21}\right) & \frac{1}{6}\alpha_{\mathrm{b}}\mathrm{x}_{32}\left(\mathrm{x}_{31}-\mathrm{x}_{12}\right) & \frac{1}{3}\alpha_{\mathrm{b}}\left(\mathrm{x}_{31}\mathrm{y}_{13}-\mathrm{x}_{12}\mathrm{y}_{21}\right)\\ \mathrm{y}_{31} & 0 & \mathrm{x}_{13}\\ 0 & \mathrm{x}_{13} & \mathrm{y}_{31}\\ \frac{1}{6}\alpha_{\mathrm{b}}\mathrm{y}_{31}\left(\mathrm{y}_{21}-\mathrm{y}_{32}\right) & \frac{1}{6}\alpha_{\mathrm{b}}\mathrm{x}_{13}\left(\mathrm{x}_{12}-\mathrm{x}_{23}\right) & \frac{1}{3}\alpha_{\mathrm{b}}\left(\mathrm{x}_{12}\mathrm{y}_{21}-\mathrm{x}_{23}\mathrm{y}_{32}\right)\\ \mathrm{y}_{12} & 0 & \mathrm{x}_{21}\\ 0 & \mathrm{x}_{21} & \mathrm{y}_{12}\\ \frac{1}{6}\alpha_{\mathrm{b}}\mathrm{y}_{12}\left(\mathrm{y}_{32}-\mathrm{y}_{13}\right) & \frac{1}{6}\alpha_{\mathrm{b}}\mathrm{x}_{21}\left(\mathrm{x}_{23}-\mathrm{x}_{31}\right) & \frac{1}{3}\alpha_{\mathrm{b}}\left(\mathrm{x}_{23}\mathrm{y}_{32}-\mathrm{x}_{31}\mathrm{y}_{13}\right)\end{bmatrix} \tag{A.23}$$

$$\widetilde{T}_{\theta u}=\frac{1}{4\ \mathrm{A}}\begin{bmatrix}\mathrm{x}_{32} & \mathrm{y}_{32} & 4\mathrm{A} & \mathrm{x}_{13} & \mathrm{y}_{13} & 0 & \mathrm{x}_{21} & \mathrm{y}_{21} & 0\\ \mathrm{x}_{32} & \mathrm{y}_{32} & 0 & \mathrm{x}_{13} & \mathrm{y}_{13} & 4\mathrm{A} & \mathrm{x}_{21} & \mathrm{y}_{21} & 0\\ \mathrm{x}_{32} & \mathrm{y}_{32} & 0 & \mathrm{x}_{13} & \mathrm{y}_{13} & 0 & \mathrm{x}_{21} & \mathrm{y}_{21} & 4\mathrm{A}\end{bmatrix} \tag{A.24}$$

where the triangle area:

$$\mathrm{A}=\frac{1}{2}\left(\mathrm{y}_{21}\mathrm{x}_{13}-\mathrm{x}_{21}\mathrm{y}_{13}\right) \tag{A.25}$$

and

$$\mathrm{K}_{\theta}=\mathrm{A}h\left(\mathrm{Q}_4^{\mathrm{T}}\mathrm{E}_{\mathrm{nat}}\mathrm{Q}_4+\mathrm{Q}_5^{\mathrm{T}}\mathrm{E}_{\mathrm{nat}}\mathrm{Q}_5+\mathrm{Q}_6^{\mathrm{T}}\mathrm{E}_{\mathrm{nat}}\mathrm{Q}_6\right) \tag{A.26}$$

where

$$E_{nat}=T_e^TET_e \tag{A.27}$$

$$\mathrm{Q}_4 = \frac{1}{2}\left(\mathrm{Q}_1 + \mathrm{Q}_2\right) \tag{A.28}$$

$$\mathrm{Q}_5 = \frac{1}{2}\left(\mathrm{Q}_2 + \mathrm{Q}_3\right) \tag{A.29}$$

$$\mathrm{Q}_6 = \frac{1}{2}\left(\mathrm{Q}_3 + \mathrm{Q}_1\right) \tag{A.30}$$

$$\mathrm{Q}_1 = \frac{2\ \mathrm{A}}{3}\begin{bmatrix} \frac{\beta_1}{\mathrm{l}_{21}^2} & \frac{\beta_2}{\mathrm{l}_{21}^2} & \frac{\beta_3}{\mathrm{l}_{21}^2} \\ \frac{\beta_4}{\mathrm{l}_{32}^2} & \frac{\beta_5}{\mathrm{l}_{32}^2} & \frac{\beta_6}{\mathrm{l}_{32}^2} \\ \frac{\beta_7}{\mathrm{l}_{13}^2} & \frac{\beta_8}{\mathrm{l}_{13}^2} & \frac{\beta_9}{\mathrm{l}_{13}^2} \end{bmatrix} \tag{A.31}$$

$$Q_2 = \frac{2\ \mathrm{A}}{3}\begin{bmatrix} \frac{\beta_9}{\mathrm{l}_{21}^2} & \frac{\beta_7}{\mathrm{l}_{21}^2} & \frac{\beta_8}{\mathrm{l}_{21}^2} \\ \frac{\beta_3}{\mathrm{l}_{32}^2} & \frac{\beta_1}{\mathrm{l}_{32}^2} & \frac{\beta_2}{\mathrm{l}_{32}^2} \\ \frac{\beta_6}{\mathrm{l}_{13}^2} & \frac{\beta_4}{\mathrm{l}_{13}^2} & \frac{\beta_5}{\mathrm{l}_{13}^2} \end{bmatrix} \tag{A.32}$$

$$Q_3 = \frac{2\ \mathrm{A}}{3}\begin{bmatrix} \frac{\beta_5}{\mathrm{l}_{21}^2} & \frac{\beta_6}{\mathrm{l}_{21}^2} & \frac{\beta_4}{\mathrm{l}_{21}^2} \\ \frac{\beta_8}{\mathrm{l}_{32}^2} & \frac{\beta_9}{\mathrm{l}_{32}^2} & \frac{\beta_7}{\mathrm{l}_{32}^2} \\ \frac{\beta_2}{\mathrm{l}_{13}^2} & \frac{\beta_3}{\mathrm{l}_{13}^2} & \frac{\beta_1}{\mathrm{l}_{13}^2} \end{bmatrix} \tag{A.33}$$

$$\mathrm{T_e} = \frac{1}{4\ \mathrm{A}^2}\begin{bmatrix} \mathrm{y}_{23}\mathrm{y}_{13}\mathrm{l}_{21}^2 & \mathrm{y}_{31}\mathrm{y}_{21}\mathrm{l}_{32}^2 & \mathrm{y}_{12}\mathrm{y}_{23}\mathrm{l}_{13}^2 \\ \mathrm{x}_{23}\mathrm{x}_{13}\mathrm{l}_{21}^2 & \mathrm{x}_{31}\mathrm{x}_{21}\mathrm{l}_{32}^2 & \mathrm{x}_{12}\mathrm{x}_{32}\mathrm{l}_{13}^2 \\ \left(\mathrm{y}_{23}\mathrm{x}_{31} + \mathrm{x}_{32}\mathrm{y}_{13}\right)\mathrm{l}_{21}^2 & \left(\mathrm{y}_{31}\mathrm{x}_{12} + \mathrm{x}_{13}\mathrm{y}_{21}\right)\mathrm{l}_{32}^2 & \left(\mathrm{y}_{12}\mathrm{x}_{23} + \mathrm{x}_{21}\mathrm{y}_{32}\right)\mathrm{l}_{13}^2 \end{bmatrix} \tag{A.34}$$

$$\alpha_{\mathrm{b}} = \frac{4}{3}; \beta_0 = \frac{1}{2}\left(1 - 4v^2\right); \beta_{1,3,5} = 1; \beta_2 = 2; \beta_4 = 0; \beta_{6,7,8} = -1; \beta_9 = -2 \tag{A.35}$$

In all of the above equations, the convention for the coordinate differences is given in Eq. (A.36):

$$\mathrm{x}_{ij} = \mathrm{x}_i - \mathrm{x}_j; \quad \mathrm{y}_{ij} = \mathrm{y}_i - \mathrm{y}_j \tag{A.36}$$

while the length of the triangle side between node i and node j is:

$$\mathrm{l_{ij}} = \sqrt{\mathrm{x_{ij}^2} + \mathrm{y_{ij}^2}} \tag{A.37}$$

The triangular plate bending element formulated by Batoz [9] consists of two rotational degrees of freedom and one out-of-plane translational degree of freedom per node. Whereas triangular membrane elements can be considered a complement to two node axial finite elements, the triangular plate bending element can be considered a surface element extension of the common two node beam element. Since the two stiffness matrix formulations are decoupled (not sharing any degrees of freedom), the summation of the two stiffness contributions can take place. The stiffness formulation in the publication by Batoz is given below and involves the triangle coordinates, the thickness, h, the material Poisson ratio, ν, and the elastic modulus, E_0 . The nine degrees of freedom are denoted according to their corresponding coordinate axis of application as shown below where signifies the translation in the element z axis and θ_x and θ_y denote the rotational degree of freedom around the in-plane x and y axes respectively.

$$\{U_{e,p}\} = \{w_1, \theta_{x1}, \theta_{y1}, w_2, \theta_{x2}, \theta_{y2}, w_3, \theta_{x3}, \theta_{y3}, \}^{\mathrm{T}} \tag{A.38}$$

The plate bending contribution to stiffness involves an assembly of a number of intermediate terms into a 9 by 9 stiffness matrix, $\mathrm{K_b}$:

$$\mathrm{K_b} = \frac{1}{2\ \mathrm{A}}[\mathrm{Q}][\alpha] \tag{A.39}$$

where A is the triangle area, [Q] is the matrix given by:

$$[Q] = \frac{1}{24}\begin{bmatrix} \left(E_1[\alpha_{11}]^T + E_2[\alpha_{21}]^T\right)[R] & \left(E_2[\alpha_{11}]^T + E_3[\alpha_{21}]^T\right)[R] & \left(E_4[\alpha_{31}]^T\right)[R] \\ \left(E_1[\alpha_{12}]^T + E_2[\alpha_{22}]^T\right)[R] & \left(E_2[\alpha_{12}]^T + E_3[\alpha_{22}]^T\right)[R] & \left(E_4[\alpha_{32}]^T\right)[R] \\ \left(E_1[\alpha_{13}]^T + E_2[\alpha_{23}]^T\right)[R] & \left(E_2[\alpha_{13}]^T + E_3[\alpha_{23}]^T\right)[R] & \left(E_4[\alpha_{33}]^T\right)[R] \end{bmatrix} \tag{A.40}$$

and $[\alpha]$ is the matrix given by:

$$[\alpha] = \begin{bmatrix} [\alpha_{11}] & [\alpha_{12}] & [\alpha_{13}] \\ [\alpha_{21}] & [\alpha_{22}] & [\alpha_{23}] \\ [\alpha_{31}] & [\alpha_{32}] & [\alpha_{33}] \end{bmatrix} \tag{A.41}$$

where

$$\mathrm{E}_1 = \mathrm{E}_3 = \frac{\mathrm{E}_0\ \mathrm{h}^3}{12\left(1 - v^2\right)}; \mathrm{E}_2 = v\mathrm{E}_1; \mathrm{E}_4 = \frac{\mathrm{E}_1(1 - v)}{2}; [\mathrm{R}] = \begin{bmatrix} 2 & 1 & 1 \\ 1 & 2 & 1 \\ 1 & 1 & 2 \end{bmatrix} \tag{A.42}$$

$$\alpha_{11} = \begin{bmatrix} \mathrm{y_3p_6} & 0 & -4\mathrm{y_3} \\ -\mathrm{y_3p_6} & 0 & 2\mathrm{y_3} \\ \mathrm{y_3p_5} & -\mathrm{y_3q_5} & \mathrm{y_3}\left(\mathrm{r_4} - 2\right) \end{bmatrix}; \alpha_{12} = \begin{bmatrix} -\mathrm{y_3p_6} & 0 & -2\mathrm{y_3} \\ \mathrm{y_3p_6} & 0 & 4\mathrm{y_3} \\ \mathrm{y_3p_4} & \mathrm{y_3q_4} & \mathrm{y_3}\left(\mathrm{r_4} - 2\right) \end{bmatrix} \tag{A.43}$$

$$\alpha_{13} = \begin{bmatrix} 0 & 0 & 0 \\ 0 & 0 & 0 \\ -y_3\left(p_4 + p_5\right) & y_3\left(q_4 - q_5\right) & y_3\left(r_4 - r_5\right) \end{bmatrix}; \alpha_{21} = \begin{bmatrix} -x_2 t_5 & x_{23} + x_2 r_5 & -x_2 q_5 \\ 0 & x_{23} & 0 \\ x_{23} t_5 & x_{23}\left(1 - r_5\right) & x_{23} q_5 \end{bmatrix} \tag{A.44}$$

$$\alpha_{22} = \begin{bmatrix} 0 & x_3 & 0 \\ x_2 t_4 & x_3 + x_2 r_4 & -x_2 q_4 \\ -x_3 t_4 & x_3\left(1 - r_4\right) & x_3 q_4 \end{bmatrix} \tag{A.45}$$

$$\alpha_{23} = \begin{bmatrix} x_2 t_5 & x_2 (r_5 - 1) & -x_2 q_5 \\ -x_2 t_4 & x_2 (r_4 - 1) & -x_2 q_4 \\ -x_{23} t_5 + x_3 t_4 & -x_{23} r_5 - x_3 r_4 - x_2 & x_3 q_4 + x_{23} q_5 \end{bmatrix} \tag{A.46}$$

$$\alpha_{31} = \begin{bmatrix} -\mathrm{x}_3\mathrm{p}_6 - \mathrm{x}_2\mathrm{p}_5 & \mathrm{x}_2\mathrm{q}_5 + \mathrm{y}_3 & -4\mathrm{x}_{23} + \mathrm{x}_2\mathrm{r}_5 \\ -\mathrm{x}_{23}\mathrm{p}_6 & \mathrm{y}_3 & 2\mathrm{x}_{23} \\ \mathrm{x}_{23}\mathrm{p}_5 + \mathrm{y}_3\mathrm{t}_5 & -\mathrm{x}_{23}\mathrm{q}_5 + \mathrm{y}_3 (1 - \mathrm{r}_5) & (2 - \mathrm{r}_5)\,\mathrm{x}_{23} + \mathrm{y}_3\mathrm{q}_5 \end{bmatrix} \tag{A.47}$$

$$\alpha_{32} = \begin{bmatrix} \mathrm{x}_3\mathrm{p}_6 & -\mathrm{y}_3 & 2\mathrm{x}_3 \\ \mathrm{x}_{23}\mathrm{p}_6 + \mathrm{x}_2\mathrm{p}_4 & -\mathrm{y}_3 + \mathrm{x}_2\mathrm{q}_4 & -4\mathrm{x}_3 + \mathrm{x}_2\mathrm{r}_4 \\ -\mathrm{x}_3\mathrm{p}_4 + \mathrm{y}_3\mathrm{t}_4 & \mathrm{y}_3 (\mathrm{r}_4 - 1) - \mathrm{x}_3\mathrm{q}_4 & (2 - \mathrm{r}_4)\,\mathrm{x}_3 - \mathrm{y}_3\mathrm{q}_4 \end{bmatrix} \tag{A.48}$$

$$\alpha_{33} = \begin{bmatrix} \mathrm{x}_2\mathrm{p}_5 & \mathrm{x}_2\mathrm{q}_5 & (\mathrm{r}_5 - 2)\,\mathrm{x}_2 \\ -\mathrm{x}_2\mathrm{p}_4 & \mathrm{x}_2\mathrm{q}_4 & (\mathrm{r}_4 - 2)\,\mathrm{x}_2 \\ t_{31} & t_{32} & t_{33} \end{bmatrix} \tag{A.49}$$

where

$$t_{31} = -\mathrm{x}_{23}\mathrm{p}_5 + \mathrm{x}_3\mathrm{p}_4 - (\mathrm{t}_4 + \mathrm{t}_5)\,\mathrm{y}_3 \tag{A.50}$$

$$t_{32} = -\mathrm{x}_{23}\mathrm{q}_5 - \mathrm{x}_3\mathrm{q}_4 + (\mathrm{r}_4 - \mathrm{r}_5)\,\mathrm{y}_3 \tag{A.51}$$

$$t_{33} = -\mathrm{x}_{23}\mathrm{r}_5 - \mathrm{x}_3\mathrm{r}_4 + 4\mathrm{x}_2 + (\mathrm{q}_5 - \mathrm{q}_4)\,\mathrm{y}_3 \tag{A.52}$$

$$\mathrm{p}_4 = -\frac{6\mathrm{x}_{23}}{\mathrm{l}_{23}}; \mathrm{p}_5 = -\frac{6\mathrm{x}_3}{\mathrm{l}_{31}}; \mathrm{p}_6 = -\frac{6\mathrm{x}_{12}}{\mathrm{l}_{12}}; \mathrm{t}_4 = -\frac{6\mathrm{y}_{23}}{\mathrm{l}_{23}}; \mathrm{t}_5 = -\frac{6\mathrm{y}_3}{\mathrm{l}_{31}} \tag{A.53}$$

$$\mathrm{q}_4 = \frac{3\mathrm{x}_{23}\mathrm{y}_{23}}{\mathrm{l}_{23}}; \mathrm{q}_5 = \frac{3\mathrm{x}_3\mathrm{y}_3}{\mathrm{l}_{31}{}^2}; \mathrm{r}_4 = \frac{3\mathrm{y}_{23}{}^2}{\mathrm{l}_{23}{}^2}; \mathrm{r}_5 = \frac{3\mathrm{y}_{31}{}^2}{\mathrm{l}_{31}{}^2} \tag{A.54}$$

The membrane and plate bending stiffness contributions can be combined into a single 18 by 18 degree of freedom stiffness matrix with the degrees of freedom given below:

$$\{U_{e,s}\} = \{u_1, v_1, w_1, \theta_{x1}, \theta_{y1}, \theta_{z1}, u_2, v_2, w_2, \theta_{x2}, \theta_{y2}, \theta_{z2}, u_3, v_3, w_3, \theta_{x3}, \theta_{y3}, \theta_{z3}\}^{\mathrm{T}} \tag{A.55}$$

The combination creates a symmetric stiffness matrix in the element coordinate system:

$$[k_{e,S}] = \begin{bmatrix} K_m & 0 \\ 0 & K_b \end{bmatrix} \tag{A.56}$$

This stiffness matrix is constructed in the local coordinate system, and to transform the matrix to the global system, an 18 by 18 transformation matrix similar to the 12 by 12 transformation matrix defined in Eq. (A.17) is used.

$$\mathrm{T}_{\mathrm{s}(18\times18)} = \begin{bmatrix} [\lambda] & [0] & [0] & [0] & [0] & [0] \\ [0] & [\lambda] & [0] & [0] & [0] & [0] \\ [0] & [0] & [\lambda] & [0] & [0] & [0] \\ [0] & [0] & [0] & [\lambda] & [0] & [0] \\ [0] & [0] & [0] & [0] & [\lambda] & [0] \\ [0] & [0] & [0] & [0] & [0] & [\lambda] \end{bmatrix} \tag{A.57}$$

where

$$[\lambda] = \begin{bmatrix} \cos\theta_{\mathrm{e1,\ g1}} & \cos\theta_{\mathrm{e1,\ g2}} & \cos\theta_{\mathrm{e1,\ g3}} \\ \cos\theta_{\mathrm{e2,\ g1}} & \cos\theta_{\mathrm{e2,\ g2}} & \cos\theta_{\mathrm{e2,\ g3}} \\ \cos\theta_{\mathrm{e3,\ g1}} & \cos\theta_{\mathrm{e3,\ g2}} & \cos\theta_{\mathrm{e3,\ g3}} \end{bmatrix} \tag{A.58}$$

and

$$[0] = \begin{bmatrix} 0 & 0 & 0 \\ 0 & 0 & 0 \\ 0 & 0 & 0 \end{bmatrix} \tag{A.59}$$

where $[\lambda]$ is the same as defined in Eq. (A.17) for the frame element transformation. Once the shell element stiffness matrix has been formulated and transformed to the global system, the global system stiffness can be formulated by summing all of the contributions from both the frame and shell elements at nodal degrees of freedom.

$$[\mathrm{K}] = \sum_{\mathrm{i}=1}^{\mathrm{NF}} [\mathrm{T_f}]_{\mathrm{i}}^{\mathrm{T}} [\mathrm{k_{e,f}}]_{\mathrm{i}} [\mathrm{T_f}]_{\mathrm{i}} + \sum_{\mathrm{j}=1}^{\mathrm{NS}} [\mathrm{T_s}]_{\mathrm{j}}^{\mathrm{T}} [\mathrm{k_{e,s}}]_{\mathrm{j}} [\mathrm{T_s}]_{\mathrm{j}} \tag{A.60}$$

where NF and NS are the total number of frame and shell elements respectively, and the subscripts i and j are the index of the current frame and shell element respectively. Once this stiffness matrix has been defined, it is the task of the aerodynamic model to generate pressure loading on the wing surface which is converted to equivalent nodal loading for the structural model.

A.1.2 Potential flow aerodynamic model

A potential flow model developed by Bramesfeld et al. [18] is incorporated into the present fluid-structure interaction process, which is used to simulate the pressure load on the wing structure. This method only requires the geometry definition of the wing structure and corresponding flow conditions. Good agreements for predicting lift and drag forces with experimental studies have been demonstrated [17, 18, 16]

This adapted potential flow method models the wing and wake with elements of distributed vorticity (DVEs) instead of the standard method of discrete vortex filaments of constant strength. This approach provides a more accurate modeling of the wing bound circulation distribution by using second order splines in the spanwise direction. The DVE

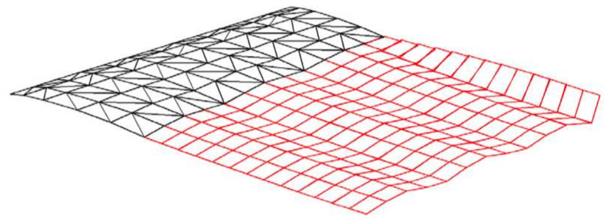

Figure A.3. Wing and wake elements generated by the potential flow model. Note the formation of the vortex sheet rollup behind the wingtip. This figure is reproduced from [28]

formulation results in a wake shear layer represented by a continuous vortex sheet with linearly-varying strength in the spanwise direction instead of the conventional representation which uses discrete vortex filaments with singularities at their centers. A demonstration of the wing elements and the wake elements it produces can be seen in Fig. A.3. A continuous vortex sheet allows for the simulation of multiple lifting surfaces and also dynamic cases such as flapping flight where conventional vortex-lattice or panel models would numerically break down due to unfavorable interaction of the wake singularities. Another advantage of this model over conventional models is the direct computation of lift forces along the bound circulation. This direct computation facilitates the transfer between the aerodynamic loads and the structural nodal loads by providing easily accessible load information at locations on the wing surface. Drag forces are computed along the trailing edge, and like many potential flow models, is a prediction of induced drag only. However, because most micro air vehicle wings are relatively thin compared to conventional aircraft wings, induced effects generally influence the drag coefficient more substantially than viscous skin friction and pressure drag effects at pre-stall angles of attack.

A.1.3 Fluid-Structure coupling framework

The structural and aerodynamic solvers are weakly coupled in the present fluid structure interaction model, a partitioned method is adapted to communicate the deformation and loading information between two solvers. The aerodynamic forces and the corresponding structural deformation are computed one after the other, instead of being solved simultaneously (as is needed with strong coupling). A detailed review of the assumptions and limitations of the partitioned fluid-structure interaction method is present by Potvin et al. [80].

As a guide to the explanation of the solution method in this research, a flowchart of the static fluid-structure interaction process is shown in Fig. A.4. Before the fluid structure interaction process begins, the initial aerodynamic and structural wing geometries are generated from a structural design program. The fluid-structure interaction simulation is initiated by calculating the aerodynamic loads on the undeformed structure. The aerodynamic pressure distribution is then transferred to the structural model, where the loading causes a deformation and formation of internal loads.

The structural surface deformation is then communicated back to the aerodynamic model by translating the deformations to the aerodynamic panel attachment nodes introduced earlier. The newly deformed aerodynamic surface geometry is then run to obtain the next iteration of aerodynamic loads. From the first deformed state iteration onward, the internal loading from the previous iteration is added to the equivalent nodal loads translated from the new pressure distribution. Convergence occurs when the accumulated internal loads equilibrate the externally applied pressure loads.

A.2 Direct numerical simulation

The present in-house DNS code solves the incompressible Navier Stokes and continuity equation, see in Eqs. (A.61) and (A.62).

$$\frac{\partial U_i}{\partial t} + \frac{\partial U_i U_j}{\partial x_j} = -\frac{\partial P}{\partial x_i} + \frac{1}{Re}\frac{\partial^2 U_i}{\partial x_j^2} \tag{A.61}$$

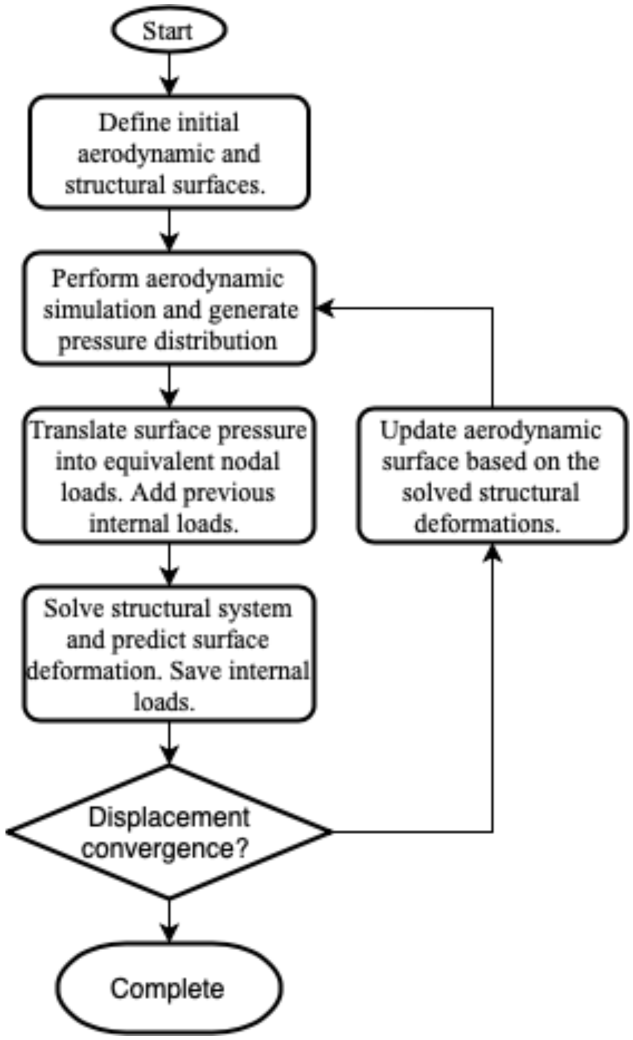

Figure A.4. Static Fluid-Structure Interaction Method

$$\frac{\partial U_i}{\partial x_i} = 0 \tag{A.62}$$

Where U_i is the component of the velocity vector in the i direction, $i = 1$ is for the component U in the streamwise direction (x), $i = 2$ is for the component V in the wall-normal (channel upper wall) direction (y) and $i = 3$ is for the component W in the spanwise direction (z). P is the pressure and Reynolds number is defined as $Re = U_b\delta/\nu$. In the present study, U_b is the bulk velocity and δ is the half channel height.

The code employs the second-order centered finite-difference scheme for the spatial derivatives on an orthogonal staggered grid. The equations are advanced in time with a hybrid third-order, low-storage Runge-Kutta scheme, with viscous terms treated implicitly and convective terms explicitly. The large sparse matrix resulting from the linear terms is inverted with an approximate factorization technique. Equations are advanced with the pressure at the previous step, which results in a non-solenoidal velocity field. A scalar quantity is used to project the velocity onto a solenoidal velocity field and update the pressure in time. The numerical discretization is discussed in more details by Orlandi [73].

The presence of a body (e.g. the bump on the lower floor seen later) is treated with the efficient immersed boundary method described in Orlandi and Leonardi [74]. The geometry boundary is found by performing ray-triangle intersection test [64]. Immersed boundary method allows the solution of flows over complex geometries without the need for computationally intensive body-fitted grids. It consists of imposing a velocity equal to zero on the body surface, which does not necessarily coincide with the grid. To avoid describing the geometry in a stepwise way, the viscous terms are discretized to take into account the real distance between the grid point and the boundary of the body, rather than the grid spacing. The method has been extensively applied for geometries in different applications [74, 19, 103, 24, 104, 102].

A.3 Large-eddy simulation approach

To achieve accurate numerical simulation, the discretized domain needs to be fine enough to include the computation of all the dynamically important structures of the flow. However, it can become challenging when the range of scales characterises is large. In that case, an alternative numerical approach is adapted in the present dissertation - large-eddy simulations (LES). In LES, only the the large scales of flow are solved, which contain the most of energy and plays a significant role in the flow under investigation. On the contrary, small scales contain less energy and expected to be universal, since they are modeled based on the resolved large scales. This approach reduces the grid resolution requirement and lowers the computational cost.

The universality of the small scale is implied in the local isotropy hypothesis with the Kolmogorov theory. This scales, being small, are independent of the flow, and thus isotropic and statistically homogeneous. This assumption holds better as far as the Reynolds number is larger, since the scale separation increases. Then, the energy cascade process is long and it is reasonable to assume that the vortical structures, as their scale decreases and the energy is transferred, lose memory of the large anisotropic flow-dependent eddies and thus becomes locally isotropic.

The filtered Navier-Stokes equations are obtained after application of the filter:

$$\frac{\partial \bar{U}_i}{\partial x_i} = 0 \tag{A.63}$$

$$\frac{\partial \bar{U}_i}{\partial t} + \frac{\partial}{\partial x_j}\left(\bar{U}_i \bar{U}_j\right) = -\frac{\partial \bar{p}}{\partial x_i} + \frac{1}{\mathrm{Re}}\frac{\partial^2 \bar{U}_i}{\partial x_j \partial x_j} + \frac{\partial \tau_{ij}}{\partial x_j} \tag{A.64}$$

where τ_{ij} is the so-called subgrid-scale (SGS) tensor which represents the interaction between the resolved scales and the unresolved ones which otherwise would not be present in the simulation.

To close the system of equations Eqs. (A.63) and (A.64) the subgrid tensor has to be modeled as function of the filtered velocity field $\bar{U}$ (closure problem). A widely used type of models are the eddy-viscosity models. These models describe the effects of the SGS terms analogously to the viscous mechanisms which take place at a molecular level in the fluids such as momentum or thermal exchanges.

The Smagorinsky model is used [91] in this present work. The subgrid viscosity is modelled as:

$$
\begin{aligned}
v_{\mathrm{sgs}} &= \left(C_s\bar{\Delta}\right)^2\sqrt{2\bar{S}_{ij}\bar{S}_{ij}} \\
&= \left(C_s\bar{\Delta}\right)^2|\bar{S}|
\end{aligned}
\tag{A.65}
$$

where S_{ij} is the rate of strain tensor and C_s is Smagorinsky constant, which in general depends upon the type of flow and usually ranges between $C_s = 0.1 - 0.2$. In this work, $C_s = 0.09$ is used based on previous works [26, 104].

REFERENCES

[1] Abudaram, Y., B. Stanford, and P. Ifju (2009). Wind tunnel testing of load-alleviating membrane wings at low reynolds numbers. In *47th AIAA Aerospace Sciences Meeting including The New Horizons Forum and Aerospace Exposition*, pp. 1468.

[2] Albertani, R., B. Stanford, J. Hubner, and P. Ifju (2007). Aerodynamic coefficients and deformation measurements on flexible micro air vehicle wings. *Experimental Mechanics 47*(5), 625–635.

[3] Ananda, G. K. (2012). Aerodynamic performance of low-to-moderate aspect ratio wings at low reynolds numbers. Master's thesis, University of Illinois at Urbana-Champaign.

[4] Ananda, G. K., P. P. Sukumar, and M. S. Selig (2015). Measured aerodynamic characteristics of wings at low reynolds numbers. *Aerospace Science and Technology 42*, 392–406.

[5] Anderson, J. (2015). *Introduction to flight*. McGraw-Hill Higher Education.

[6] Arenas, I., E. García, M. K. Fu, P. Orlandi, M. Hultmark, and S. Leonardi (2019). Comparison between super-hydrophobic, liquid infused and rough surfaces: a direct numerical simulation study. *Journal of Fluid Mechanics 869*, 500–525.

[7] Armour Edge (n.d.). `https://www.armouredge.com/`. [Online; accessed 30-January-2020].

[8] Bartolomé, L. and J. Teuwen (2019). Prospective challenges in the experimentation of the rain erosion on the leading edge of wind turbine blades. *Wind Energy 22*(1), 140–151.

[9] Batoz, J.-L. (1982). An explicit formulation for an efficient triangular plate-bending element. *International Journal for Numerical Methods in Engineering 18*(7), 1077–1089.

[10] Bechert, D. and M. Bartenwerfer (1989). The viscous flow on surfaces with longitudinal ribs. *Journal of Fluid Mechanics 206*, 105–129.

[11] Bhaganagar, K., J. Kim, and G. Coleman (2004). Effect of roughness on wall-bounded turbulence. *Flow, turbulence and combustion 72*(2-4), 463–492.

[12] Blade Partners (n.d.). `http://bladepartners.com/services-wear-tear/`. [Online; accessed 30-January-2020].

[13] Bleischwitz, R., R. de Kat, and B. Ganapathisubramani (2015). Aspect-ratio effects on aeromechanics of membrane wings at moderate reynolds numbers. *AIAA Journal 53*(3), 780–788.

[14] Bleischwitz, R., R. De Kat, and B. Ganapathisubramani (2016). Aeromechanics of membrane and rigid wings in and out of ground-effect at moderate reynolds numbers. *Journal of Fluids and Structures 62*, 318–331.

[15] Bowen, A. and D. Lindley (1977). A wind-tunnel investigation of the wind speed and turbulence characteristics close to the ground over various escarpment shapes. *Boundary-Layer Meteorology 12*(3), 259–271.

[16] Bramesfeld, G. (2010). Small and micro aerial vehicles: How much span is too much span? *Journal of Aircraft 47*(6), 1982–1990.

[17] Bramesfeld, G. and M. D. Maughmer (2008a). Effects of wake rollup on formation-flight aerodynamics. *Journal of Aircraft 45*(4), 1167–1173.

[18] Bramesfeld, G. and M. D. Maughmer (2008b). Relaxed-wake vortex-lattice method using distributed vorticity elements. *Journal of Aircraft 45*(2), 560–568.

[19] Burattini, P., S. Leonardi, P. Orlandi, and R. A. Antonia (2008). Comparison between experiments and direct numerical simulations in a channel flow with roughness on one wall. *Journal of Fluid Mechanics 600*, 403–426.

[20] Celik, I. (2005). Rans/les/des/dns: the future prospects of turbulence modeling. *Journal of fluids engineering 127*(5), 829–830.

[21] Chan, L., M. MacDonald, D. Chung, N. Hutchins, and A. Ooi (2015). A systematic investigation of roughness height and wavelength in turbulent pipe flow in the transitionally rough regime. *Journal of Fluid Mechanics 771*, 743–777.

[22] Chavarin, A. and M. Luhar (2020). Resolvent analysis for turbulent channel flow with riblets. *AIAA Journal 58*(2), 589–599.

[23] Cheney, J., N. Konow, K. Middleton, K. Breuer, T. Roberts, E. Giblin, and S. Swartz (2014). Membrane muscle function in the compliant wings of bats. *Bioinspiration & biomimetics 9*(2), 025007.

[24] Ciri, U. and S. Leonardi (2021). Heat transfer in a turbulent channel flow with superhydrophobic or liquid-infused walls. *Journal of Fluid Mechanics 908*.

[25] Ciri, U., G. Petrolo, M. V. Salvetti, and S. Leonardi (2017). Large-eddy simulations of two in-line turbines in a wind tunnel with different inflow conditions. *Energies 10*(6), 821.

[26] Ciri, U., M. Salvetti, K. Carrasquillo, C. Santoni, G. Iungo, and S. Leonardi (2018). Effects of the subgrid-scale modeling in the large-eddy simulations of wind turbines. In *Direct and large-eddy simulation x*, pp. 109–115. Springer.

[27] Coceal, O., T. Thomas, I. Castro, and S. Belcher (2006). Mean flow and turbulence statistics over groups of urban-like cubical obstacles. *Boundary-Layer Meteorology 121*(3), 491–519.

[28] Combes, T. P. (2012). An efficient fluid-structure interaction method for conceptual design of flexible micro air vehicle wings: Development, comparison, and application. Master's thesis, Saint Louis University.

[29] Combes, T. P., A. S. Malik, G. Bramesfeld, and M. W. McQuilling (2015). Efficient fluid-structure interaction method for conceptual design of flexible, fixed-wing microair-vehicle wings. *AIAA Journal 53*(6), 1442–1454.

[30] Cook, R. D., D. S. Malkus, M. E. Plesha, and R. J. Witt (1974). *Concepts and applications of finite element analysis*, Volume 4. Wiley New York.

[31] de Jesus, A., L. Schiavo, J. Azevedo, and J.-P. Laval (2016). Adverse pressure gradients and curvature effects in turbulent channel flows. In *Progress in Wall Turbulence 2*, pp. 295–306. Springer.

[32] Dean, B. and B. Bhushan (2010). Shark-skin surfaces for fluid-drag reduction in turbulent flow: a review. *Philosophical Transactions of the Royal Society A: Mathematical, Physical and Engineering Sciences 368*(1929), 4775–4806.

[33] Dong, H., A. T. Bode-Oke, and C. Li (2018). *Learning from Nature: Unsteady Flow Physics in Bioinspired Flapping Flight*. InTech.

[34] Driest, E. V. (1956). On turbulent flow near a wall. *Journal of the aeronautical sciences 23*(11), 1007–1011.

[35] Fang, X. and M. F. Tachie (2019). On the unsteady characteristics of turbulent separations over a forward–backward-facing step. *Journal of Fluid Mechanics 863*, 994–1030.

[36] Felippa, C. A. (2003). A study of optimal membrane triangles with drilling freedoms. *Computer Methods in Applied Mechanics and Engineering 192*(16-18), 2125–2168.

[37] Flack, K. A. and M. P. Schultz (2010). Review of hydraulic roughness scales in the fully rough regime. *Journal of Fluids Engineering 132*(4).

[38] Flack, K. A., M. P. Schultz, and R. J. Volino (2020). The effect of a systematic change in surface roughness skewness on turbulence and drag. *International Journal of Heat and Fluid Flow 85*, 108669.

[39] Forouzi Feshalami, B., M. H. Djavareshkian, A. H. Zaree, M. Yousefi, and A. Mehraban (2018). The role of wing bending deflection in the aerodynamics of flapping micro aerial vehicles in hovering flight. *Proceedings of the Institution of Mechanical Engineers, Part G: Journal of Aerospace Engineering*, 0954410018806081.

[40] Fröhlich, J. and W. Rodi (2002). Introduction to large eddy simulation of turbulent flows. *Closure strategies for turbulent and transitional flows 1*(8), 197–224.

[41] Fujita, K., K. Uechi, K. Takahashi, and H. Nagai (2019). Effects of rib number and rigid trailing edge on flexible-skinned thick wing at low reynolds number. In *AIAA Scitech 2019 Forum*, pp. 1893.

[42] Galvao, R., E. Israeli, A. Song, X. Tian, K. Bishop, S. Swartz, and K. Breuer (2006). The aerodynamics of compliant membrane wings modeled on mammalian flight mechanics. In *36th AIAA Fluid Dynamics Conference and Exhibit*, pp. 2866.

[43] García-Mayoral, R. and J. Jiménez (2011). Drag reduction by riblets. *Philosophical transactions of the Royal society A: Mathematical, physical and engineering Sciences 369*(1940), 1412–1427.

[44] Gatto, A., P. Bourdin, and M. Friswell (2012). Experimental investigation into the control and load alleviation capabilities of articulated winglets. *International Journal of Aerospace Engineering 2012*.

[45] Gaudern, N. (2014). A practical study of the aerodynamic impact of wind turbine blade leading edge erosion. In *Journal of Physics: Conference Series*, Volume 524, pp. 012031. IOP Publishing.

[46] Ge, M., H. Zhang, Y. Wu, and Y. Li (2019). Effects of leading edge defects on aerodynamic performance of the s809 airfoil. *Energy conversion and management 195*, 466–479.

[47] Goldberg, D. E. (1989). *Genetic Algorithms in Search, Optimization and Machine Learning*. Addison-Wesley.

[48] Gordnier, R. E. and P. J. Attar (2014). Impact of flexibility on the aerodynamics of an aspect ratio two membrane wing. *Journal of Fluids and Structures 45*, 138–152.

[49] Gursul, I., D. Cleaver, and Z. Wang (2014). Control of low reynolds number flows by means of fluid–structure interactions. *Progress in Aerospace Sciences 64*, 17–55.

[50] Han, W., J. Kim, and B. Kim (2018). Effects of contamination and erosion at the leading edge of blade tip airfoils on the annual energy production of wind turbines. *Renewable Energy 115*, 817–823.

[51] Hattori, H. and Y. Nagano (2010). Investigation of turbulent boundary layer over forward-facing step via direct numerical simulation. *International Journal of Heat and Fluid Flow 31*(3), 284–294.

[52] Hu, H., M. Tamai, and J. T. Murphy (2008). Flexible-membrane airfoils at low reynolds numbers. *Journal of Aircraft 45*(5), 1767–1778.

[53] Hunt, J. C., A. A. Wray, and P. Moin (1988). Eddies, streams, and convergence zones in turbulent flows. *NASA Center for Turbulence Research, Proceedings of the Summer Program*.

[54] J.-P. Laval (2011). DNS: 2D converging-diverging channel, $R_e = 12600$. `https://turbmodels.larc.nasa.gov/Other_DNS_Data/conv-div-channel12600.html`. [Online; accessed 30-January-2020].

[55] Jeong, J. and F. Hussain (1995). On the identification of a vortex. *Journal of fluid mechanics 285*, 69–94.

[56] Keidel, D., G. Molinari, and P. Ermanni (2019). Aero-structural optimization and analysis of a camber-morphing flying wing: Structural and wind tunnel testing. *Journal of Intelligent Material Systems and Structures 30*(6), 908–923.

[57] Khosravi, P., R. Ganesan, and R. Sedaghati (2007). Corotational non-linear analysis of thin plates and shells using a new shell element. *International Journal for Numerical Methods in Engineering 69*(4), 859–885.

[58] Kyle, R., F. Wang, and B. Forbes (2019). The effect of a leading edge erosion shield on the aerodynamic performance of a wind turbine blade. *Wind Energy*.

[59] Leonardi, S. and I. P. Castro (2010). Channel flow over large cube roughness: a direct numerical simulation study. *Journal of Fluid Mechanics 651*, 519–539.

[60] Leonardi, S., P. Orlandi, R. Smalley, L. Djenidi, and R. Antonia (2003). Direct numerical simulations of turbulent channel flow with transverse square bars on one wall. *Journal of Fluid Mechanics 491*, 229.

[61] Mariotti, A., G. Buresti, G. Gaggini, and M. Salvetti (2017). Separation control and drag reduction for boat-tailed axisymmetric bodies through contoured transverse grooves. *Journal of Fluid Mechanics 832*, 514–549.

[62] Marquillie, M., U. Ehrenstein, and J.-P. Laval (2011). Instability of streaks in wall turbulence with adverse pressure gradient. *Journal of Fluid Mechanics 681*, 205–240.

[63] Marquillie, M., J.-P. Laval, and R. Dolganov (2008). Direct numerical simulation of a separated channel flow with a smooth profile. *Journal of Turbulence* (9), N1.

[64] Möller, T. and B. Trumbore (1997). Fast, minimum storage ray-triangle intersection. *Journal of graphics tools 2*(1), 21–28.

[65] Möller, T. and B. Trumbore (2005). Fast, minimum storage ray/triangle intersection. In *ACM SIGGRAPH 2005 Courses*, pp. 7. ACM.

[66] Mollicone, J.-P., F. Battista, P. Gualtieri, and C. M. Casciola (2017). Effect of geometry and reynolds number on the turbulent separated flow behind a bulge in a channel. *Journal of Fluid Mechanics 823*, 100–133.

[67] Moser, R. D., J. Kim, and N. N. Mansour (1999). Direct numerical simulation of turbulent channel flow up to $Re_\tau = 590$. *Physics of Fluids 11*(4), 943–945.

[68] Mottaghian, P., J. Yuan, and U. Piomelli (2018). Boundary layer separation under strong adverse pressure gradient over smooth and rough walls. In *Direct and Large-Eddy Simulation X*, pp. 173–179. Springer.

[69] Mueller, T. J. and G. E. Torres (2001). Aerodynamics of low aspect ratio wings at low reynolds numbers with applications to micro air vehicle design and optimization. Technical report, NOTRE DAME UNIV IN OFFICE OF RESEARCH.

[70] Nasser, M. M. (2015). Fast computation of the circular map. *Computational Methods and Function Theory 15*(2), 187–223.

[71] Nasser, M. M. (2020). Plgcirmap: A matlab toolbox for computing conformal mappings from polygonal multiply connected domains onto circular domains. *SoftwareX 11*, 100464.

[72] Oduyela, A. and N. Slegers (2014). Gust mitigation of micro air vehicles using passive articulated wings. *The Scientific World Journal 2014*.

[73] Orlandi, P. (2000). *Fluid flow phenomena. A numerical toolkit.* Kluwer Academic.

[74] Orlandi, P. and S. Leonardi (2006). Dns of turbulent channel flows with two-and three-dimensional roughness. *Journal of Turbulence* (7), N73.

[75] Orlandi, P., S. Leonardi, and R. A. Antonia (2006). Turbulent channel flow with either transverse or longitudinal roughness elements on one wall. *Journal of Fluid Mechanics 561*, 279–305.

[76] Orlanski, I. (1976). A simple boundary condition for unbounded hyperbolic flows. *Journal of computational physics 21*(3), 251–269.

[77] Paranjape, A. A., S.-J. Chung, and M. S. Selig (2011). Flight mechanics of a tailless articulated wing aircraft. *Bioinspiration & biomimetics 6*(2), 026005.

[78] Pelletier, A. and T. J. Mueller (2000). Low reynolds number aerodynamics of low-aspect-ratio, thin/flat/cambered-plate wings. *Journal of Aircraft 37*(5), 825–832.

[79] Perry, A. E., W. H. Schofield, and P. N. Joubert (1969). Rough wall turbulent boundary layers. *Journal of Fluid Mechanics 37*(2), 383–413.

[80] Potvin, J., K. Bergeron, G. Brown, R. Charles, K. Desabrais, H. Johari, V. Kumar, M. McQuilling, A. Morris, G. Noetscher, et al. (2011). The road ahead: A white paper on the development, testing and use of advanced numerical modeling for aerodynamic decelerator systems design and analysis. In *21st AIAA Aerodynamic Decelerator Systems Technology Conference and Seminar*, pp. 2501.

[81] Rankin, C. and F. Brogan (1986). An element independent corotational procedure for the treatment of large rotations. *Journal of pressure vessel technology 108*(2), 165–174.

[82] Rankin, C. and B. Nour-Omid (1988). The use of projectors to improve finite element performance. In *Computational Structural Mechanics & Fluid Dynamics*, pp. 257–267. Elsevier.

[83] Rojratsirikul, P., M. Genc, Z. Wang, and I. Gursul (2011). Flow-induced vibrations of low aspect ratio rectangular membrane wings. *Journal of Fluids and Structures 27*(8), 1296–1309.

[84] Sachs, G. and F. Holzapfel (2007). Flight mechanic and aerodynamic aspects of extremely large dihedral in birds. In *45th AIAA Aerospace Sciences Meeting and Exhibit*, pp. 46.

[85] Santhanakrishnan, A., N. Pern, K. Ramakumar, and J. Jacob (2005). Enabling flow control technology for low speed uavs. In *Infotech@ Aerospace*, pp. 6960.

[86] Santoni, C., K. Carrasquillo, I. Arenas-Navarro, and S. Leonardi (2017). Effect of tower and nacelle on the flow past a wind turbine. *Wind Energy 20*(12), 1927–1939.

[87] Sareen, A., C. A. Sapre, and M. S. Selig (2014). Effects of leading edge erosion on wind turbine blade performance. *Wind Energy 17*(10), 1531–1542.

[88] Sherry, M., D. L. Jacono, and J. Sheridan (2010). An experimental investigation of the recirculation zone formed downstream of a forward facing step. *Journal of Wind Engineering and Industrial Aerodynamics 98*(12), 888–894.

[89] Shields, M. and K. Mohseni (2012). Effects of sideslip on the aerodynamics of low-aspect-ratio low-reynolds-number wings. *AIAA journal 50*(1), 85–99.

[90] Smagorinsky, J. (1963a). General circulation experiments with the primitive equations. i. the basic experiment. *Monthly Weather Review 91*(3), 99–164.

[91] Smagorinsky, J. (1963b). General circulation experiments with the primitive equations: I. the basic experiment. *Monthly weather review 91*(3), 99–164.

[92] Song, S. and J. Eaton (2002). The effects of wall roughness on the separated flow over a smoothly contoured ramp. *Experiments in fluids 33*(1), 38–46.

[93] Sun, X. and J. Zhang (2017). Effect of the reinforced leading or trailing edge on the aerodynamic performance of a perimeter-reinforced membrane wing. *Journal of Fluids and Structures 68*, 90–112.

[94] Wang, J. and Y. Liu (2008). Experimental study on lift characteristics for flow over flexible cropped delta wings. *Journal of Aircraft 45*(6), 2158–2161.

[95] Wang, Y., R. Hu, and X. Zheng (2017). Aerodynamic analysis of an airfoil with leading edge pitting erosion. *Journal of Solar Energy Engineering 139*(6).

[96] Webster, D., D. DeGraaff, and J. Eaton (1996). Turbulence characteristics of a boundary layer over a two-dimensional bump. *Journal of Fluid Mechanics 320*, 53–69.

[97] Wehmann, H.-N., L. Heepe, S. N. Gorb, T. Engels, and F.-O. Lehmann (2019). Local deformation and stiffness distribution in fly wings. *Biology open 8*(1), bio038299.

[98] Wrist, A. H. and J. P. Hubner (2018). Aerodynamic comparisons of flexible membrane micro air vehicle wings with cambered and flat frames. *International Journal of Micro Air Vehicles 10*(1), 12–30.

[99] Xu, M. and M. Wei (2016). Using adjoint-based optimization to study kinematics and deformation of flapping wings. *Journal of Fluid Mechanics 799*, 56–99.

[100] Yang, H., J. Dudley, and R. Harris (2018). Aeroelasticity validation study for a three-dimensional membrane wing. *AIAA Journal 56*(6), 2361–2371.

[101] Yang, T., M. Wei, K. Jia, and J. Chen (2019). A monolithic algorithm for the flow simulation of flexible flapping wings. *International Journal of Micro Air Vehicles 11*, 1756829319846127.

[102] Yu, H., U. Ciri, S. Leonardi, and A. Malik (2020). A simplified model for drag evaluation of a streamlined body with surface roughness. *Bulletin of the American Physical Society*.

[103] Yu, H., U. Ciri, A. Malik, and S. Leonardi (2019). Direct numerical simulation for irregular roughness on a curved surface. *Bulletin of the American Physical Society 64*.

[104] Yu, H., U. Ciri, A. Malik, and S. Leonardi (In press, 2020). Decoupled effects of localized camber and spanwise bending for flexible thin wing. *AIAA Journal*.

[105] Yu, H., M. Seger, and A. Malik (2018). Wing frame design and strain tuning for optimum endurance of flexible fixed-wing micro air vehicles. In *2018 AIAA/AHS Adaptive Structures Conference*, pp. 1287.

[106] Yu, H., W. Yang, H. Duan, and A. Malik (2019). Flexibility distribution tuning by wing frame inner structure morphing for fixed-wing unmanned aerial vehicle. In *AIAA Aviation 2019 Forum*, pp. 3348.

[107] Zhang, Z., N. Martin, A. Wrist, and J. P. Hubner (2015). Geometry and prestrain effects on the aerodynamic characteristics of battenreinforced membrane wings. *Journal of Aircraft 53*(2), 530–544.

[108] Zhu, X. and W. Anderson (2018). Turbulent flow over urban-like fractals: prognostic roughness model for unresolved generations. *Journal of Turbulence 19*(11-12), 995–1016.

BIOGRAPHICAL SKETCH

Haoliang Yu was born in Xinjiang, China. He obtained his Bachelor of Science in Mechanical Engineering in 2015 at Fuzhou University. Then he enrolled in the graduate school at The University of Texas at Dallas and started to pursue his PhD degree in Mechanical Engineering in 2016.

CURRICULUM VITAE

Haoliang Yu

February 14, 2021

Contact Information:

Department of Mechanical Engineering
The University of Texas at Dallas
800 W. Campbell Rd.
Richardson, TX 75080-3021, U.S.A.
Email: haoliang.yu@utdallas.edu

Educational History:

BS, Mechanical Engineering, Fuzhou University, 2015
MS, Mechanical Engineering,The University of Texas at Dallas, 2017
PhD, Mechanical Engineering,The University of Texas at Dallas, 2021

Employment History:

Research Assistant, The University of Texas at Dallas, August 2016 – present
Teaching Assistant, The University of Texas at Dallas, August 2017 – present
Additive Manufacturing Simulation Intern, Ansys, Inc. May 2020 – Dec 2020

Publications:

Journal papers:

- **Yu, H.**, Ciri, U., Malik, A., & Leonardi, S. (2021) A simplified model for drag evaluation of a streamlined body with leading edge damage. *Journal of Turbulence*, (Submitted)
- Sunny, S., Mathews, R., **Yu, H.**, & Malik, A. (2021) Effects of microstructure, inherent stress and temperature when predicting residual stress induced during hybrid powder bed fusion with interlayer burnishing. *Additive Manufacturing*, (Submitted)
- Sunny, S., **Yu, H.**, Mathews, R., & Malik, A. (2021). A predictive model for in situ distortion correction in laser powder bed fusion using laser shock peen forming. *The International Journal of Advanced Manufacturing Technology*, 1-19.
- **Yu, H.**, Sunny, S., Mathews, R., Malik, A., & Li, W. (2020). Improved grain structure prediction in metal additive manufacturing using a dynamic kinetic Monte Carlo framework. *Additive Manufacturing*, 37, 101649.

- **Yu, H.**, Ciri, U., Malik, A. S., & Leonardi, S. (2020). Decoupled effects of localized camber and spanwise bending for flexible thin wing. *AIAA Journal*, 1-14.
- Sadeh, S., Gleason, G., Hatamleh, M., Sunny, S., **Yu, H.**, Malik, A., & Qian, D. (2019). Simulation and Experimental Comparison of Laser Impact Welding with a Plasma Pressure Model. *Metals*.

Conference papers and abstracts:

- **Yu, H.**, Ciri, U., Leonardi, S., & Malik, A. (2020). A simplified model for drag evaluation of a streamlined body with surface roughness. In *APS Division of Fluid Dynamics Meeting Abstracts*.
- Gleason, G., Sunny, S., Sadeh, S., **Yu, H.**, & Malik, A. (2020). Eulerian Modeling of Plasma-Pressure Driven Laser Impact Weld Processes. *Procedia Manufacturing*, 48, 204-214.
- **Yu, H.**, Ciri, U., Malik, A., & Leonardi, S. (2019). Direct numerical simulation for irregular roughness on a curved surface. In *APS Division of Fluid Dynamics Meeting Abstracts*.
- **Yu, H.**, Yang, W., Duan, H., & Malik, A. (2019). Flexibility Distribution Tuning by Wing Frame Inner Structure Morphing for Fixed-Wing Unmanned Aerial Vehicle. In *AIAA Aviation 2019 Forum* (p. 3348).
- **Yu, H.**, Seger, M., & Malik, A. (2018). Wing frame design and strain tuning for optimum endurance of flexible fixed-wing micro air vehicles. In *2018 AIAA/AHS Adaptive Structures Conference* (p. 1287).
- Zhang, F., Malik, A. S., & **Yu, H.** (2018). High-Fidelity Roll Profile Contact Modeling by Simplified Mixed Finite Element Method. In *ASME 2018 13th International Manufacturing Science and Engineering Conference*. American Society of Mechanical Engineers Digital Collection.